ETD Archive

2018

Modeling Liver Diseases Using Hepatic Cell Microarrays

Alexander David Roth

MODELING LIVER DISEASES USING HEPATIC CELL MICROARRAYS

ALEXANDER D. ROTH

Bachelor of Science in Biological Engineering

Cornell University

January 2009

Master of Engineering in Biological Engineering

Cornell University

August 2009

Master of Science in Chemical Engineering

The Ohio State University

May 2013

Submitted in partial fulfillment of requirements for the degree

DOCTOR OF ENGINEERING IN CHEMICAL ENGINEERING

at

CLEVELAND STATE UNIVERSITY

December 2018

We hereby approve this dissertation

for

Alexander D. Roth

Candidate for the Doctor of Engineering in Chemical Engineering degree

For the Department of Chemical and Biomedical Engineering
and

CLEVELAND STATE UNIVERSITY's
College of Graduate Studies by

_____

Moo-Yeal Lee, Ph.D., Dissertation Committee Chairperson, Chemical and Biomedical Engineering, date

_____

Joanne Belovich. Ph.D., Dissertation Committee Member, Chemical and Biomedical Engineering, date

_____

Nolan B. Holland, Ph.D., Dissertation Committee Member, Chemical and Biomedical Engineering, date

_____

Chandra Kothapalli, Ph.D., Dissertation Committee Member, Chemical and Biomedical Engineering, date

_____

Xue-Long Sun, Ph.D., Dissertation Committee Member, Chemistry, date

Date of Defense: Wednesday, June 13th, 2018

This student has fulfilled all requirements for the Doctor of Engineering degree.

_____

Chandra Kothapalli, Ph.D., Doctoral Program Director

DEDICATION

This thesis is dedicated to my brother, Gary Roth, and to three of my favorite teachers, Emily Weinstein, Donna Midgol, and Lester Milch.

staff throughout the department and college who helped along the way, including Rebecca Laird, Darlene Montgomery, Jim Barker, Ali Kaddah, David Epperly, and Karen Johnson.

I would also like to thank everyone who lent me their emotional support and help during the duration of my graduate studies. Patricia Otcasek, Erica Henkin, Zachary Pichler, Rita Kizys, Anne Koelewijn, and everyone else from the Graduate and Professional Student Association who helped give me balance. The CSU Counseling Center and CASC who gave me tools to succeed and be happy. My pets, Jon and Arya, who kept me laughing and smiling as I would read and write. My parents, Ronnie and Jeffrey Roth, my brother, Gary Roth, my sister, Lisa Roth, my grandparents, Marilyn and Harvey Roth, and everyone else from my family and close friends who make me feel present and cared for no matter how many miles separated us. And last but definitely not least, my partner, Shannon Harwood, who talks to me every day about everything, and who has fed and watered me during those days when I do not get enough sun.

MODELING LIVER DISEASES USING HEPATIC CELL MICROARRAYS

ALEXANDER D. ROTH

ABSTRACT

Hepatocellular carcinoma (HCC) is an invasive and aggressive cancer of the liver that arises due to chronic cirrhosis. Research into understanding HCC has focused on two-dimensional (2D) and three-dimensional (3D) technologies to simulate the liver microenvironment and use animal models to model how HCC affects the rest of the body. 3D hydrogel models are desired because they can mimic the transport behavior observed *in vivo* by structurally mimicking the extracellular matrix (ECM) without the ethical concerns of animal models. However, hydrogels can be toxic to cells and require optimal procedures for appropriate handling. In this study, we created 3D models of liver diseases on high-throughput platforms. First, we optimized hydrogel attachment on micropillar chips by coating them with 0.01 w/v % PMA-OD in ethanol. Next, we optimized the protocol for encapsulation of viable Hep3B cells PuraMatrix peptide hydrogel, using a higher seeding density ($6 * 10^6$ cells/mL) and two post-print media washes. Then, we established the ability to transduce adenoviruses *in situ* in encapsulated cells and successfully demonstrated their dose-response behavior towards six compounds. In the second part, we scaled up to using the microwell chip platform and optimized the polymerization of oxidized methacrylated alginate (OMA) for Hep3B encapsulation. First, we plasma-treated microwell chips for 15 minutes at high RF to minimize bubbles. Then, we optimized micro-scale photopolymerization conditions at 45 % methacrylated OMA (OMA-45) and 2 w/v % OMA with 0.05 w/v % PI and reflective background under either low intensity, long duration (2.5 mW/cm² for 2 minutes) or high intensity, short duration (4.0 mW/cm², 30 seconds) light by testing cell viability at these conditions. Third, we used

these OMA conditions to develop a high-throughput, real-time 3D cell migration assay on a newly engineered 384-pillar plate with sidewalls. We first developed a set of a protocols where out-of-focus cells are removed mean position of cells on a pillar are quantified. Next, we established a delay in growth factor release rate by co-encapsulating growth factors with OMA and methacrylated heparin sulfate sulfate (MH). Finally, we demonstrated collective cell migration occurred toward angiogenic growth factors at 6-10 μm/day over two weeks. These results provide optimized chemistry between hydrogels and polystyrene, show effective hydrogel polymerization techniques for microscale tissue engineering, and yield several methods where scientists can model liver diseases in high-throughput.

TABLE OF CONTENTS

LIST OF TABLES

LIST OF FIGURES

CHAPTER I

BACKGROUND AND MOTIVATION

1.1. Introduction

Liver disease affects about 30 million (or 1 in 10) Americans alone annually [1]. Included in this statistic are non-alcoholic fatty liver disease (NAFLD), hepatitis, drug-induced liver injury (DILI), cirrhosis, and liver cancer [1]. In addition, as sanitary conditions in parts of the country and world are still poor, some of the incidents for these diseases are on the rise. Unlike other cancers, liver cancer rates are increasing in the US [1,2]. Because of the presence of liver disease throughout the US and world, it becomes necessary to develop adequate models to understand these illnesses and develop compounds to combat them.

In the case of liver cancer, the most prevalent cancer of the liver is hepatocellular carcinoma (HCC). HCC is generally triggered by chronic cirrhosis, which itself is caused by previous injuries to the liver, including hepatitis and the presence of various toxins [3]. About 65% of national liver cancer cases and 75% of global liver cancer cases are attributed to this illness [4]. The increases seen in HCC seem to be increasing in regions where

individuals do not have access to good hygiene or clean food [1,5]. This illness is the most common cause of death of individuals affected with cirrhosis, with estimates varying between 10-30% of individuals with cirrhosis eventually developing HCC [5]. HCC generally is associated with poor prognosis in the late stage of diagnosis, as tumors are highly invasive and have a great potential to metastasize locally and globally [3]. While there are certain therapeutics that are available to treat the illness, the therapies for HCC are often tied to the mechanisms that trigger the illness itself and are again generally only effective during early staging of the disease [3,6].

Many of the current technologies for understanding HCC and creating compounds to combat the illness relies on screens for *in vitro* hepatocyte cultures as a method to weed out drug candidates before clinical trials [7]. Subsequent follow-up with animal models are used to reduce the possible drug failure [8–10]. For developing treatments and modeling the illness, emphasis is put on the evolution of the tumor, looking at angiogenesis and metastasis in particular [4,11]. Unfortunately, these screens often have poor predictive value in assessing hepatotoxicity potential [12]. HCC is an illness that often takes on characteristics based on the individual diagnosed, so the cells and technologies used in the models should account for this individual variation. Thus, the goal of scientists and doctors is to better understand the mechanisms for liver diseases and focus on individualized treatment methods.

For understanding liver disease (and HCC in particular), there is a shift of researchers to investigate three-dimensional (3D) *in vitro* cell cultures. Two-dimensional (2D) cultures often simplify the models significantly, and lack any extracellular matrix (ECM) components, which play a major role in understanding diseases [13]. Meanwhile,

2

in vivo models can give some insight into HCC, but ultimately animals are physiologically different enough from humans where they may not fully reflect all aspects of the disease [14]. Additionally, use of animals always contains some ethical issues and is expensive. 3D *in vitro* models reconcile 2D *in vitro* models with *in vivo* models by replicating the transport and mechanical properties seen *in vivo* while eliminating the need use of animal models [13]. Hydrogels are generally used in these 3D models, as they are ideal for replicating the tissue ECM properties [15].

In this introductory chapter, I will discuss the various mechanisms that contribute towards the development HCC. Next, I will highlight various models and techniques used in assessing HCC, focusing on distinguishing 2D *in vitro* cultures, 3D *in vitro* cultures, and *in vivo* models, and looking at particular techniques used in *in vitro* cultures. Finally, I will look at materials used to in 3D *in vitro* studies, with particular emphasis on using various hydrogel materials to mimic the liver ECM.

1.2. Mechanisms of HCC Development

HCC is often caused by the development of a previous disease within the liver where the damaged tissue can eventually turn into cancer. Generally, these triggers can be manifested through exposure to liver toxins, such as alcohol/drugs, or viral insults, such as hepatitis. These diseases often trigger cirrhosis, which can eventually lead to HCC. However, other disease states, particularly ones that affect metabolism, may also trigger the development of HCC. The triggers and molecular mechanisms behind the development of HCC can be seen in Table 1. Additionally, because of the mutagenic nature associated with the main causes of HCC, affected individuals can contain multiple tumors, each with

3

distinct markers. In this section, we intend to discuss the various mechanisms that can lead to HCC, focusing on the pathways that lead to HCC over other forms of liver cancer.

Table 1. Mechanisms Associated with HCC

Cause for HCC	Affected Pathways
Hepatitis B Virus (HBV)	P53, Wnt/β-catenin, pRB, miR-122
Hepatitis C Virus (HCV)	P53, Wnt/β-catenin
Aflatoxins	P53, miR-122
Alcohol-Induced Liver Injury	Wnt/β-catenin
Diabetes	P53

1.2.1. Hepatitis B and C Viruses (HBV and HCV)

Hepatitis is the most common cause of HCC, with about 80 percent of HCC individuals had hepatitis preceding the onset of HCC [16,17]. Of these cases, hepatitis B virus (HBV) is the most common form of the illness that gives way to HCC, though cases of hepatitis C virus (HCV) cases have also been reported [17–19]. Chronic viral hepatitis is said to trigger HCC both directly and indirectly. Most of the indirect contribution to HCC is from the development of cirrhosis. While both forms of hepatitis can be manifested acutely and initially cured, both viruses can eventually lead to the chronic version of the disease [20]. and it is in this state where individuals become significantly more susceptible to both cirrhosis and HCC. In HBV, this is particularly troublesome as young children are more susceptible to developing chronic hepatitis than older individuals, and chronic HBV is not easily treated [16,17]. While both forms of the virus play roles in the development of HCC, the mechanisms associated with each are different. HBV is a double-stranded DNA virus that can integrate into the host genome and induce hepatocarcinogenesis via promoting cell proliferation, affecting DNA repair, and inducing inflammatory damage

[17,21]. HCV is a single stranded RNA virus that triggers host immune responses to cause inflammation but does not integrate with host DNA [22].

Both diseases can trigger HCC through multiple molecular mechanisms. Of all the causes for HCC, HBV has the potential to trigger more mechanisms than the others. These mechanisms include the Wnt/β-catenin regulatory pathway [23], mutations on the p53 [24] or the tumor suppressor retinoblastoma (pRB) genes [5,23], complicating the mitogen-activated protein (MAP) kinase pathway [25], or affecting cytokine signaling [25,26]. Additionally, all of these pathways can act synergistically with expression of key cancer markers. The role of HBV in affecting these pathways involves the increased propensity for DNA methylation, histone modifications, and affecting the RNA interference mechanisms that prevent the spread of cancer.

In the case of Wnt/β-catenin, this pathway is important in regulating cell proliferation, cell differentiation, and cell migration [27,28]. This pathway can be compromised via numerous mutations within the pathway, though most mutations that can progress to HCC directly affect β-catenin [23,27]. One thing to note about this pathway is that Wnt/β-catenin dysregulation is not strictly linked to HCC, as other cancers have this pathway compromised, and individuals with type 2 diabetes may show an upregulation in some isoforms of Wnt [3,28]. Both HBV and HCV have been linked with mutations to Wnt/β-catenin [17,23]. For β-catenin, mutations result in the increase of Wnt, linking to increased proliferation [28]. Mutations due to HBV and HCV in frizzled-7, a G protein coupled receptor (GPCR) involved in the Wnt pathways have also been found to be linked to increased susceptibility to HCC [29].

In the case of the P53 pathway, often a single point mutation is enough to cause cancer, as inactivation of the tumor suppressor 53 (TP53) gene causing a decrease in apoptosis in the normal cell cycle, and general over-proliferation of cancer cells [24]. For HBV, this is due to a point mutation at the 249 codon [5,24]. However, mutations at codon 250 have been found to be in some cases of HCC as well [5].

In the pRB pathway, these set of genes act to suppress tumor formation by regulating the E2F family in cell cycle division and the activity of cyclin-dependent kinases (CDKs) [30]. pRB is reported to be tied to p53 as loss of pRB function results in loss of p53 function as well [23,30]. Mutations in the pRB pathway are specifically a mechanism of HBV only, with the pathways being most effected are inhibition of p16 and overexpression of cyclin D1, which again promotes excessive cell growth [23].

MAP kinases play a significant role in cell proliferation, differentiation, adhesion, and survival, as they receive signals from many of the tyrosine kinase receptors, including endothelial growth factor receptor (EGFR) and platelet-derived growth factor receptor (PDGFR) [25]. In the case of the MAP kinase pathway, both forms of hepatitis serve to upregulate this pathway, promoting cell proliferation and angiogenesis [3,25]. Unlike many of the other mechanisms for HCC discussed here, dysregulation of the MAP kinase pathway seems to be strictly a phenomenon related to hepatitis-induced HCC, though other cancers are also known to have levels of dysregulation associated with MAP kinase [23].

Mechanistically, issues related to the mutations in p53, pRB, and β-catenin are tied to the effect of DNA methylation by HBV or HCV, causing mutations in the various pathways leading to cancer [16,31]. The methylation sites result in the mutations described earlier, all of which result in uncontrolled cell growth [16]. Thus, the largest role of

6

hepatitis in development of HCC stems from mutations in proteins that control the cell cycle.

This is not to say that the only mechanisms governing hepatitis-induced HCC rely to DNA methylation. Histones can be modified, which can also increase the likelihood of individuals developing HCC [31]. For example, HCV is known to increase the expression of protein phosphatase 2A (PP2A), which binds to protein arginine methyltransferase 1 (PRMT1) [17]. The result is a decrease in DNA desphosphorylation and histone methylation at sites which control hepatocellular carcinogenesis and DNA damage repair, though the latter is also important for viral replication [16]. For HBV, the generated viral protein HBx interacts with histone acetyltransferases in a way to promote their activity, which results in increased cellular replication [16].

Besides DNA methylation, HBV and HCV both have roles in affecting RNA interference and circulating miRNA, which deregulates the cell cycles. For HCV, miR-122, an antiproliferative microRNA can act to increase the odds of developing HCC as miR-122 serves to replication HCV [23,32]. On the other hand, this same microRNA acts against replication for HBV [32]. While generally suppressed levels of miR-122 have been shown to be indicative of HCC, that does not apply to individuals affected by HCV-induced hepatitis [32]. Other microRNAs that are associated with hepatitis include miR-141 which also serves to repression HBV replication, while miR-1 seems to increase HBV replication [23,32].

1.2.2. Aflatoxins

Aflatoxins are a class of compounds characterized as secondary metabolites of the *Aspergillus flavus* and *Aspergillus paracitus* molds [33]. Aflatoxins are generally found in

contaminated harvest foods such as corn, rice, nuts and sorghum[33]. Aflatoxin metabolites are generally considered to be both poisonous and carcinogenic, with several versions of Aflatoxin considered to be strongly linked to the development of HCC [33].

One striking thing to note is how aflatoxins can also work synergistically with hepatitis B to manifest HCC. The incidence of HCC seems to be drastically increased when exposed to both aflatoxins and HBV [16,31]. Aflatoxins both stimulate the Wnt/β-catenin as well as the p53 mechanisms of developing cancer [28,34]. For the p53 protein, it has been found that aflatoxin mutates the 249 codon, which limits the tumor suppressor gene [35]. While this mutation is not absent in other cancers, aflatoxin's metabolism in the liver is cause for HCC to develop over other cancers [4,5].

Of all the potentially generated aflatoxins, the B1 variant (AFB1) is the most potent, as nearly all animal tests have developed liver cancer once exposed to this toxin [24,35]. However, other variants of aflatoxin may also generate HCC. AFB1 may actually lead to HCC *in utero* and it has been shown that the most susceptible individuals to HCC are those exposed to HBV and aflatoxins at young ages [3,16]. The odds of an individual developing HCC in response to the presence of AFB1 can vary between 3:1 and 10:1 depending on the health of the individual and other factors that can contribute to HCC [16,23].

The mechanisms for control of these various pathways involve DNA methylation and RNA interference. In the case of DNA methylation, the CYP450 generated metabolite, AFB1-8,9, exo-epoxide adducts onto the guanine residues of DNA at the 249 codon in P53 [35]. Aflatoxins may also inhibit the production of miR-122, which controls the replication of liver cells [32]. This makes miR-122 an interesting microRNA to exam for HCC, as

promoting miR-122 levels could inhibit HCC due to aflatoxins, whereas it has the opposite effect of HCC induced by HCV [32].

1.2.3. Alcohol- and Drug-Induced Toxicity

Alcohol- and drug-induced toxicity can both contribute to the development of cirrhosis in the liver, and subsequently HCC. The major mechanism associated with toxicity developing into cancer involves the effects alcohol has on the Wnt/β-catenin pathway [29,34]. Generally, β-catenin is the protein most likely to be mutated from alcohol- or drug-induced toxicity [16,36]. Additionally, it is believed that CYP2E1 function is compromised via histone modifications in drug-induced toxicity [16]. This compromise in CYP2E1 function further inhibits drug metabolism and may affect oxidative stress within the cell as well [37,38].

1.2.4. Other Concurrent Disease States

HCC has been shown to be caused by several other illnesses or conditions. An example of this is type II diabetes. As a metabolic disorder, diabetes mellitus has been shown to have some effects that may cause HCC, specifically inducing cirrhosis via affecting hormonal changes in the liver [39]. Obesity and hypertension has the effect to increase susceptibility to diabetes, but it may also cause HCC through separate mechanisms [11,39,40]. Additionally, hemochromatosis is another causative agent for HCC. The effect of iron-overload (hemochromatosis) has been shown to be associated with the p53 mutations seen in aflatoxin-induced toxicity and HBV, targeting the methylation at the 249 and 250 codons in p53 [31]. Hemochromatosis has several causes, including genetic mechanisms and previous disease states, including diabetes [41].

1.2.5. Genetic and Environmental Factors

HCC does not need a pre-requisite of cirrhosis to occur, though most cases do follow that pattern. As HCC can occur with the presence of HBV in the system regardless of the concurrent conditions, any individuals that carry the virus are susceptible to developing cancer. African and Asian descent seem to be more at risk than other ethnic groups, though there is no gender predisposition to the disease [31]. Additionally, family history associated with HCC is shown to increase the susceptibility of an individual to develop the illness [16]. There are also several other carcinogens that may cause HCC. Generally, the carcinogens that promote cancer do so via mutations on the Ras family of proteins, which ultimately has the impact of increase MAP kinase protein signaling, specifically targeting MAP kinase kinase (MEK) 1 and 2 [25]. This has the impact of decreasing apoptosis and increasing proliferation [25].

1.2.6. Diagnostic Measures

There are several biomarkers present that are commonly used for the detection of HCC. Specific microRNAs are generally as an indicator for the presence of this illness in individuals. However, there are other prognostic indicators. Testing for the levels of alpha-fetoprotein (AFP) and des-gamma carboxyprothrombin (DCP) are generally recommended by physicians before further examination of the tumor [42]. AFP is normally found in elevated levels in pregnant women, playing a fetal analog or pre-cursor to serum albumin; but if it is detected at elevated levels, AFP can otherwise indicate the presence of benign or malignant germ cell tumors or other liver cancers in addition to HCC [19,43]. DCP is a variant of the coagulation protein prothrombin though it may also be detected in individuals with vitamin K deficiency [42]. Genetic profiling can also be used to diagnose HCC, as

quantifying the levels of affected microRNAs or specific gene panels can be indicative of a positive diagnosis. Genetic panels can predict the illness over 90% of the time [42,44]. The presence of interleukins 2 and 15 (IL-2 and IL-15 respectively), regulatory T cells (T_{reg}s), and tumor-associated macrophages (TAMs) are also positive diagnostic markers for HBV-induced HCC [45]. Additionally, CTs and MRIs are also used to observe the tumor and confirm diagnosis with the blood tests [36].

1.3 Models and Techniques for Understanding HCC

In order to better understand HCC, *in* vitro and *in vivo* models have been generated for examining the illness. Most important are the presence of appropriate cell types and the recapitulation of the tumor architecture. The tumor physiology is characterized by having a diverse set of cell types, including cancer-associated fibroblasts, cells promoting angiogenesis, and cancer immune cells [3]. In addition, tumor vasculature is more heterogeneous and less dense than healthy tissue, as blood flow and oxygen and nutrient transport is limited within the tumor [46]. Predictive tumor models are designed to mimic these features and understand the mechanisms behind cell proliferation and metastasis. In this section, we look to discuss the various models used to study HCC, and evaluate how they perform in terms of accurate representations of the illness.

1.3.1. 2D Cancer Migration Models

Because of the complexity of HCC, 2D cancer models focus on a limited number of variables when examining the illness. 2D models are best used when observing proliferation and some migration studies, as they can give insight into the effects of some potential chemoattractants. One such example uses wound healing assays, where artificial

wounds are introduced into cellular monolayers, and the cancer cells migration in response to close the gap [47–49]. Similar models, such as the cell exclusion zone assay [50] or the fence assay [51], also create barriers in a monolayer of cells through which the cells must migrate. The cell exclusion zone assay utilizes seeding on two different sides of a removal barrier and watch cells close the gap, while a fence assay utilizes cells seeded inside of a removal insert and spread after the insert is removed. All of these migration assays are mid-throughput and can be used for real-time monitoring of migration. While there is ease associated with quantifying this type of behavior and chemical gradients can be induced, the 2D environment is still limited regarding nutrient transport and the interactions that can occur between different cells [47,52].

Another method that can be used is the Boyden chamber model. Here, cells are seeded in a removable well with a porous membrane on the bottom surface while submerged in a second well containing media and any chemoattractants/repellants [47,48]. The pores are small enough to make sure cells simple do not fall through the membrane without a chemical gradient driving the movement, meaning cells will only pass through if the chemoattractant is strong enough [53,54]. If the pore is sufficiently small, cells will not pass through but instead adhere strongly to the bottom part of the top chamber. Both of the wound healing assay and the Boyden chamber have some moderate-throughput potential to test multiple factors affecting HCC metastasis. However, the design of the Boyden chamber makes it a better end-point assay for cancer cell migration, whereas other 2D migration assays are kinetic [47].

To overcome some of the limitations of 2D cell migration, scientists have introduced microfluidic devices. Here, capillary flow can assist with some movement of

the cell, while chemoattractants or repellents can be added near the periphery of the capillary, allowing scientists to measure how much cells may deflect in movement in response to these cues [55,56]. Microfluidic devices provide some shear effects seen *in vivo* and are suitable for real-time tracking of cell movement, but they are relatively expensive to develop and their throughput is lower than some of the other 2D migration models [55].

1.3.2. Spheroid Models

In generating spheroids, scientists, clinicians, and researchers can observe a round 3D structure that is similar in architecture to normal tumor models. Generally, spheroids strictly consist of cells, though they occasionally may include ECM components, or they may secrete some ECM components themselves [57]. While spheroids do not have to be homogenous in cell composition, spheroids do have uniform cell seeding density when initially developed, which is not always the case when tumors are observed [58]. Additionally, because most spheroids do lack the ECM components, a large part of the interaction between cancer cells and their microenvironment is missing, with cell-cell interactions dominating the signaling occurring in these models [47]. It is also difficult to generate spheroids based on size, and in the case of co-culture spheroids, it is sometimes hard to predict how various cell types are arranged within the spheroid [59,60]. However, much like actual tumors, spheroid cultures do maintain the aspects of the cell density arrangement; namely, cells in the center of the spheroid tend to be both hypoxic, nutrient deficient, and necrotic, whereas cells closer to the spheroid periphery are more proliferative and have better exposure to nutrients and oxygen [47,61].

There are several methods in which to create spheroid structures. Using hanging droplets within plates is one way to generate spheroids, as gravity forces cells to aggregate near the bottom of the droplet [62]. Depending on the size of the plate, several spheroids can be generated, with homogenous size distributions [63]. However, because these spheroids are generated in media or PBS, many of the architectural supports associated with 3D matrices and the ECM have been eliminated, unless cells are able to generate these components themselves [63,64]. Additionally, for more thorough assays, the spheroids need to be transferred to a different plate, which is very labor intensive and more susceptible to human error than other methods for generating spheroids [47]. Finally, the volumes associated with hanging droplets are quite low, making the droplet more susceptible to evaporation, which has a direct impact on the osmolarity of the solution, and hence, the viability of the cells in the spheroid [62].

Another common method for spheroid generation are using ultralow attachment plates. Seeding cells on non-adherent substrates such as agar can force cells to interact with each other and form spheroids [65]. Like the hanging droplet method, ultralow attachment plates can produce vast quantities of spheroids [66]. Spheroids generated this way are also easier for transfer than ones in hanging droplets, making them somewhat less labor intensive [65,66]. However, the spheroid suspensions generated this way tend to be heterogeneous in size, and they too suffer from issues where a lack of ECM components can make holding together the spheroid more difficult [65].

While hanging droplet and ultra-low attachment plates can generate large amounts of spheroids, addition of hydrogels or ECM components can strengthen the spheroid via promoting cell-cell and cell-ECM interactions typically seen *in vivo*. Here, cells are either

14

seeded on top of or within hydrogels, and over time, cells will naturally aggregate if incubated and maintained with cell culture media [49]. Generation of spheroids this way relies on the mechanisms of the cells to aggregate and bond to the surrounding structures than reactions to physical stimuli [47,67]. Spheroids generated this way tend to have characteristics more similar to *in vivo* studies and these spheroids can also be generated in high-throughput [67]. Like ultra-low attachment plates, spheroids generated this way are typically heterogenous in size and structure and using hydrogels or ECM components can occasionally cause problems when staining or imaging cells [47,65].

Generation of spheroids can be subsequently used in either 2D or 3D migration assays. Much like the fence assay, spread of cells away from the spheroid can be measured in real time to characterize the cells [68]. Additionally, spheroids can be embedded or seeded on top of hydrogel matrices and directed to migrate in response to certain cues [49]. The problem with using spheroids this way is that while behavior of the spheroid can be tracked easily, individual cell movement is harder to track as compared to many of the 2D models [68].

1.3.3. Sandwich Culture Assays

In sandwich culture, cells are seeded between two hydrogel layers, in which the hydrogel layers contain various chemoattractants or chemorepellants [69]. The cells respond to the chemoattractants or repellants either through increased growth or through migration in response to the signal [69,70]. Like spheroids, cells in sandwich culture exist in 3D, so the mechanical and chemical interactions are closer to *in vivo* cultures. Like spheroids, imaging can be difficult, although this is generally less of a problem as individual cells are easier to track once outside the spheroid [47,71]. Some of the cell-cell

interactions are not completely reflected on initial seeding, as it takes time for the cells to organize themselves into 3D structures [70]. However, spheroids can also be seeded in sandwiches, though individual cell tracking is still difficult with sandwich spheroids [72]. Another drawback is that because the cells are seeded within hydrogels, there are other potential barriers to delivery of nutrients and oxygen to the sandwiched cells, which can make sustained culture of sandwiched cells somewhat more difficult as compared to other HCC mimics [73]. Like the other cultures, there are relatively few limits to cells sourced for sandwich culture, which means explants and heterogenous tissues can be seeded [74].

1.3.4. Co-Culture Systems

Liver co-culture systems provide the advantage of giving a more complete profile of liver behavior in the presence of drugs. While the liver is primarily composed of hepatocytes, there are other cells present, including several different kinds of lymphocytes, sinusoidal endothelial cells, and stellate cells [75]. In the case of cancer, co-cultures can consist of any combination of the cancers cells with fibroblasts, immune cells, stem cells, and potentially other cell types present in the affected organ, including normal functioning cells (i.e., co-cultures of hepatocytes and HCC cells) [76,77]. In addition, the liver is organized based on proximity to blood vessels. Cells closer the portal vein are more involved in oxidative metabolism, β-oxidation of fatty acids, ureagenesis, and gluconeogensis, whereas cells further from major blood vessels are involved in biotransformation of drugs, glutamine synthesis, lipid synthesis, and glycolysis [78]. As a result, development of models for understanding liver disease is more complex While co-culture systems tend to be more complex than some of the other HCC systems discussed, they generally do incorporate 3D behavior and better recapitulation of the tumor

microenvironment than other systems [79]. Additionally, co-cultures can be incorporated into some of the previously mentioned technologies, including 2D migration assays [80] and spheroid cultures [61].

Most HCC co-cultures focus on the use of HCC along with fibroblasts and immune cells, as these cells are generally necessary to best model the *in vivo* responses. While utilizing HCC is obvious, fibroblasts are important for secretion of ECM proteins such as laminin and fibronectin [81]. Laminin is especially important, as this component is generally present in greater quantities in HCC than in healthy livers [6,46,82]. Generally, fibroblasts can be incorporated in 3D suspensions with HCC cells, regardless of the presence or absence of hydrogels [79]. Additionally, 2D co-cultures can also be achieved. By seeding fibroblasts first, several ECM components can be secreted, which allows for easy adherence of HCC cells onto various surfaces and can promote cell-ECM interactions that are normally absent in 2D culture [83].

Several kinds of immune cells have interactions with HCC and the ECM in ways that involve inflammation responses that can subsequently lead either the liver's tolerance or adaptive immunity to certain signals. While KCs are native to the liver, other cells, including CD8+ T cells and regulatory T cells (T_{reg}s) both play a role in the progression of HCC [45]. The relative presence of tumor-associated macrophages (TAMs) is also an indicator of the prognosis of potential outcomes for an individual affected with HCC [84]. HCC co-cultures with lymphocytes generally have the lymphocytes in suspension, responding to signals of static HCC cells, as the lymphocytes will act on the tumor [84].

Disadvantages of coculture platforms involve the complexity of the scaffolds to accurately mimic the *in vivo* liver environment, as well miniaturization being limited due

to the number of cells needed to create a full model of a tumor. The assay miniaturization is of particular importance, as this also impacts scalability and cost. Even integrating all cell types on a 96 well-plate platform is challenging because decreasing the number of cells limits interactions observed between different cell types. Thus, size of culture optimization should be considered when designing small scale liver tissues for toxicity testing.

1.3.5. In vivo Models

Animal models make up a large fraction of the studies used in scientific literature for HCC [85]. While *in vitro* models can use excised tumors or immortalized cell lines such as Hep3B, HepG2, or Huh7 cells, rat and mouse models make up most organisms used for *in vivo* studies [86]. Cells and the animals they are implanted into can vary significantly depending on the mechanism of HCC development studied. Many *in vivo* models use xenografts of HCC tumors by injecting HCC cells subcutaneously [84]. Generally, this procedure is less invasive and easier to monitor than orthotopic models, where HCC cells are surgically implanted within the liver. However, the orthotopic model is considered to be more accurate as the cells are residing at the site where the illness normally starts, so growth and metastasis of the tumor is more adequately reflected [85].

Scientists have successfully shown the treatment of various HCCs developed *in vivo* using the orthotopic model. The aforementioned Hep3B, HepG2, and Huh7 cell lines have all been implanted into mice, with cell growth demonstrated to have occurred in these various models, and treatment was found to be affected in some of them [85]. The drawback to using *in vivo* models is that even with humanized mice, several functions cannot be completely replicated in a different species, and the size of mice also limits how large tumors can grow within the organism [60], making it much easier to treat the illness

here than clinically. Additionally, because of the *in vivo* implementation of tumors, the imaging of the tumors is generally done with CT or MRI, which are more expensive and time consuming than the methods used to visualize *in vitro* models [4,11].

1.4. Materials to Mimic the 3D Liver Architecture

As discussed earlier, the best methods for understanding the behavior of the liver or other tissues *in vitro* rely on the development of materials that allow for cells to organize themselves into their native architecture. Most often, this relies on hydrogels or similar materials to recapitulation the 3D architecture seen in the tissues. Hydrogels are most commonly used as their high degree of water content allows the hydrogel to reflect some of the mechanical properties seen in tissues [87]. Here we discuss the various kinds of hydrogels as well as other 3D platforms that have been used to characterize HCC.

1.4.1. Alginate

Alginate is an anionic polysaccharide hydrogel derived from algae [88]. It forms a gel in the presence of strong divalent cations, which serve to crosslink the negatively charged hydroxyl groups [89]. Alginate was originally used medically to encapsulate pancreatic islet cells as a potential to treat patients with diabetes [89]. Since then, its use has expanded to other cell lines, including the study of hepatic cells [60]. The use of alginate hydrogels is popular as alginate is generally structurally stable and the polymerization mechanisms are relatively nontoxic [90]. However, because of it being derived from plant matter, alginate lacks many of the necessary functional groups for cell adherence [89]. Subsequently, this limits the amount of manipulation cells can have on their microenvironment and slows down any changes should they come.

In order to bypass these issues, alginate can be modified with functional groups. Integrin-binding sites at RGD residues can be added within the hydrogel structure, which allows for better cell adherence [91]. Other peptide binding sequences have also been conjugated onto alginate to promote cell adhesion [91]. Additionally, co-encapsulation with mammalian derived hydrogels such as Matrigel can also improve cell-ECM interactions [92]. Alginate is generally best employed when emphasizing structure stability of the hydrogel with some level of co-encapsulation with somewhat more biocompatible polymers, such as modified polyethylene glycol (PEG), polycaprolactone (PCL), or polylactic acid (PLA) [91].

1.4.2. Collagen

Collagen is a structural protein found in many organs in the body, including the liver. Most of the liver's structural protein mass consists of collagen I, though there is a noticeable amount of collagen IV in the liver as well [52]. Collagen can also be used as a biomimetic hydrogel *via* temperature-based polymerization [93]. The advantage to using collagen is that since it is a native protein, hepatocyte and hepatoma cells have favorable interactions with the protein, making it a suitable host for cell encapsulation and migration [72]. Collagen's natural compatibility with liver cells has made it so that liver models mimic many of the key liver functions, including drug and glucose metabolism [94]. The disadvantage to using collagen as a hydrogel is because it is a native liver protein, it is more susceptible to degradation and ECM remodeling, which may or may not be desired in a given experiment [13]. Additionally, because of the temperature-controlled polymerization mechanism, cells must be kept at lower temperatures to prevent premature gelation, and this temperature cycling can have a deleterious effect on cells [95].

1.4.3. Gelatin

Gelatin is another biologically derived hydrogel, composed of peptides and proteins following the hydrolysis of collagen in the connective tissue, skin, and bones of mammalian organisms [96]. Gelatin can be polymerized in a variety of different ways, including natural polymerization in sufficient concentrations in water [97]. However, addition of crosslinking agents or enzymatic polymerization using transaminases can improve hydrogel stability [98]. Because of the fact that gelatin is biologically derived and has multiple methods for polymerization, it is a popular hydrogel for cell encapsulation purposes. However, addition of a crosslinker always increases the chance for cytotoxicity and the use of enzymatic catalysis for polymerization often results in inconsistent crosslinking densities, which makes the hydrogel less tunable for desired properties [47].

Gelatin naturally contains many of the important functional groups necessary for cell adhesion to the ECM. While gelatin is a popular hydrogel for several different kinds of tissue engineering, methacroyl gelatin (GelMA) has seen increasing popularity for wound healing purposes [98]. Here, GelMA is modified with methacrylate groups, which allows for a photo-polymerization based mechanism of the hydrogel [99]. This serves to increase the stiffness of the hydrogel relative to gelatin and makes it somewhat more resistant to degradation while still allowing cells the ability to reshape the surrounding tissue [98]. However, the process for photopolymerization is also quite toxic, as radicals generated from the polymerization can generate ROS and cause oxidative damage [98,99].

1.4.4 Hyaluronic Acid

Hyaluronic acid (HA) is a glycosaminoglycan (GAG), a long polysaccharide chain containing a urea group in every other saccharide molecule [100]. It is found in connective

and epithelial tissue throughout the body and serves as a structural molecule to anchor cells while also having numerous regulatory processes [100]. HA is degraded relatively easily, which makes it a suitable material for both structural stability and ECM remodeling [15,101]. The mechanism by which hyaluronic acid forms gels can depend on the modifications associated with the material [100,101]. This can be enzymatic polymerization, photopolymerization, or polymerization using a cross-linking agent like glutaraldehyde. The drawbacks to using HA are, much like gelatin, related to the agents used for crosslinking more than compatibility issues with the hydrogel itself [100,102].

1.4.5. Fibrin

Fibrin is the natural product polymer formed during scar tissue formation when fibrinogen is polymerized by thrombin [96,103]. The same mechanism governs the formation of this hydrogel. Because it is a naturally occurring hydrogel, the toxicity associated with fibrin is quite low, and it is easily compatible with multiple cell types [96]. The drawback with using fibrin is that it is arguably the most susceptible to degradation, as cells have a natural mechanism to restructure the ECM around scar tissue [90]. Additionally, this hydrogel generally has weaker mechanical properties compared to other hydrogels, so it is best used in conjunction with other degradation-resistant hydrogels such as alginate or hyaluronic acid [104,105]. However, the ability for fibrin to be degraded and be biocompatible means cells have better abilities to reshape their microenvironment.

1.4.6. Peptide-Functionalized Materials

Cells can adhere to ECM proteins as a result of interactions between integrins and certain peptide motifs such as RGD sequences. While synthetic hydrogels have been used to serve as mimics of the *in vivo* ECM, biocompatibility issues pose a problem which

affects cell viability, function, and the ability of the cell to reshape its environment. Modification of hydrogels to include the integrin-binding peptides can promote cell-adhesion and improve biocompatibility of many synthetic hydrogels [106]. As cells are adherent, they are also more likely to move and manipulate the environment in reaction to various chemical cues.

Generally, the hydrogels that are peptide-functionalized include many of the polysaccharide-based hydrogels, including alginate, chitosan, and hyaluronic acid [107–109]. Fibrin, collagen, and derivatives of these hydrogels already have the functional sites necessary for cell adhesion. Additionally, several synthetic hydrogels are commercially available that contain peptide groups, including PuraMatrix, PGMatrix, and HydroMatrix [110]. Because of the use of peptide linkages, these matrices are more suited for soft-tissue models [110,111]. A disadvantage of using these hydrogels are the expenses associated with them [110]. While the other hydrogels can be obtained in bulk from natural sources, peptide hydrogels must be synthesized, and peptide functionalization of natural hydrogels incurs its own preparation costs that may be more expensive than other hydrogel modifications.

1.4.7. Nanofibers

An alternative to using hydrogels or derived liver matrices for *in vitro* 3D cell culture are nanofibers. Nanofibers are fibers with nanometer-sized diameter that may be synthesized from a variety of different functional materials, including polyvinyl alcohol (PVA), PCL, PLL, PEG, and others [112]. They are generally synthesized via electrospinning or phase separation process. In both cases, fiber alignment can be random, or controlled depending on the application [113,114]. After fibers are synthesized, cells are

23

seeded. While the fibers offer some of the structure advantages of hydrogels (namely, increased stiffness and homogeneity of structure), nanofibers are not necessarily degraded by the cells, which gives the cell little ability to shift the environment [115]. Fibers can be used in migration studies, particularly if they are aligned to promote directional movement [116].

1.5. Significance and Aims of the Research

The goal of this study is to have a better understanding of various liver disease states by utilizing a comprehensive high-throughput platform. Initially, we intended to use this platform for analyzing the potential for an individual to be susceptible to drug induced liver injury (DILI). DILI refers to injuries from ADRs because of individual, non-dose-dependent responses. The advantage of our system includes rapid generation of miniaturized liver tissue constructs in microarrays *via* bioprinting technology, which allows us to examine combinations of microenvironment conditions. Our system is capable of printing hydrogels onto small, microscope slide-sized micropillar/microwell chips containing 532 individual tests, or onto larger 384-pillar plates that are paired with standard 384-well plates. The microwell chip can be used as a vessel for a layer-by-layer printing approach for 3D cell culture. Alternatively, the microwell chip can contain media and be paired with the micropillar chip, which is used for culturing a small, but sizeable number of cells for individual assays. The 384-pillar plate with sidewalls offers a slightly larger scale test that pairs with a known, readily available platform, and the sidewalls on the platform can hold hydrogels in place as the plate changes between various media compositions in the 384 well plate. The basis of our work relies on the hypotheses that 1) three-dimensional (3D) hydrogel layers are a better mimic of the *in vivo* liver

24

microenvironment than two-dimensional (2D) platforms or other 3D platforms, 2) layer-by-layer printing of hydrogels can be used to create organized liver tissue organoids *in vitro*, and 3) liver cancer cells will migration through hydrogels *in vitro* towards potential metastatic cues and that this migration can be quantified in 3D.

The most significant outcome of this study is the creation of miniaturized liver tissue constructs and an ability to accurately measure and quantify cell migration *in situ*. These results can be used to better understand metastasis, or any kind of cell migration to various chemical cues. Another potential outcome is the ability to control for genetic expression of key enzymes affected during certain liver disease states. While not all contributing factors towards DILI or liver cancer will be examined in this study, our platform can be used for future studies to examine those other factors.

Specific Aims: The specific aims (and subsequent chapter themes) are:

Aim 1: Encapsulate hepatic cells in hydrogels that can be used for high-throughput drug screening and *in situ* adenoviral transduction. The goal of this work was to develop a platform where we could encapsulate Hep3B human hepatoma cell line in PuraMatrix that could provide the cells with a stable and non-toxic architecture while also being suitable for genetic modification using adenoviral transduction.

Aim 2: Optimize hepatic cell encapsulation conditions in a photopolymerizable hydrogel for creating layered cell structures. While PuraMatrix is a suitable platform for adenoviral gene transduction, the protocol for cell printing and the hydrogel itself was toxic due to the removal of salts from printing solutions and acidity of PuraMatrix. Additionally, the micropillar plate platform was unsuitable for long-term multicellular

tissue culture as the low volume of cells used during the print may not be enough for the encapsulated cells to develop an appropriate liver microenvironment seen in disease states. Thus, we decided to try new hydrogels for Hep3B cell encapsulation and find a more suitable platform for 3D cell culture. Here, we optimized the use of photopolymerizable oxymethacrylated alginate (OMA) for cell encapsulation for 3D cell culture in the microwell chip. OMA polymerizes in the presence of photoinitiator (PI) 2-Hydroxy-4′-(2-hydroxyethoxy)-2-methylpropiophenone (Irgacure 2959) while exposed to near-UV light. Our desire to use this material is for layer-by-layer printing; a photopolymerizable hydrogel gives us more control over when we decide to initiate polymerization *in situ*.

Aim 3: Simulate migration of liver cancer cells in 3D and quantify their migration *in situ* in high throughput. After optimizing photopolymerizable OMA for use, we simulate hepatocellular carcinoma (HCC) by printing Hep3B cells in OMA and quantify Hep3B cell migration in 3D in the presence of various chemoattractants. Our group designed a 384-pillar plate with sidewalls paired with a 384-well plate using the same assay protocol. This new modification allows for better nutrient transport to all cells while being usable for combinatorial studies. First, we tested the effects of leaching of various growth factors and ECM proteins known to exist in the microenvironment of HCC by encapsulating the compounds with OMA in the presence and absence of heparin sulfate. Next, we demonstrated the ability to image cells *in situ* by transducing Hep3B cells with lentiviruses containing fluorescent proteins. Finally, transduced cells migrated in 3D because of exposure to various growth factors and ECM proteins. This migration was quantified using a set of macros developed for ImageJ that filter out out-of-focus cells, quantify the intensity of the filtered cell images, then calculates the mean position of the cells on the pillar.

CHAPTER II

POLYMER COATING ON A MICROPILLAR CHIP FOR ROBUST ATTACHMENT OF PURAMATRIX PEPTIDE HYDROGEL FOR 3D HEPATIC CELL CULTURE

2.1. Introduction

Recent advances in three-dimensional (3D) cell culture technologies demonstrate clear advantages over traditional two-dimensional (2D) cell cultures, which include cells in biomimetic 3D microenvironments, promoting cell-cell and cell-extracellular matrix (ECM) interactions that are critical for many biological and physiological processes [78,117,118]. The transport of drugs and nutrients is vastly different between the two systems, resulting in some 2D cell culture systems that cannot accurately predict certain biological disease states [78,119,120]. Mimicking 3D microenvironments are crucial in both modeling disease states with cell models and understanding how to treat these diseases.

One way to mimic *in vivo* 3D cell structure is to use hydrogels as a scaffold for cell growth. Hydrogels can provide a mechanical and biochemical environment that is similar

to *in vivo* cell-ECM interactions, promoting the formation of tissue-like structures [90]. Hydrogels might be biologically derived, completely synthetic, or somewhere in between the synthetic and biological extremes [87,96,102,121–123]. Hydrogels can be polymerized in the presence of divalent ions (e.g., alginate), UV-light (methacrylated collagen), enzymes (fibrinogen), or changes in temperature and pH (Matrigel), all of which depend on the hydrogel being studied [124–127]. Many of the synthetic hydrogels use biological motifs found in the ECM to improve cell attachment, and thus, providing biocompatibility [96,121,123]. Nonetheless, large scale 3D-tissue culture in hydrogels is challenging for high-throughput screening (HTS) of potential drug candidates due to cumbersome steps necessary for dispensing viscous hydrogels and changing growth media over time, difficulty in imaging 3D-cultured cells, limited diffusion of nutrients within a 3D construct, and high costs of primary human cells.

To alleviate these issues, miniaturized 3D cell cultures in hydrogels have been investigated, including cellular microarrays [128–130]. While microarray technologies have existed for molecular detection, including nucleic acids [131–133] and proteins [134,135], cellular microarrays are relatively recent development [90,136]. Cells suspended in hydrogels may be micropatterned onto various surfaces using photolithography [137–140], or they may be printed in mini-arrays on functionalized glass slides and plastic chips using automatic liquid dispensation systems [129,130,136,141]. These bioprinted cells were cultured in 3D and subsequently exposed to various compounds and viruses for toxicity assessment [129,130,136]. For example, Kwon *et. al.* and Lee *et. al.* have developed a micropillar/microwell chip system that can support miniaturized 3D cultures with 50 - 400 cells seeded on each micropillar for recapitulating

28

certain *in vivo* behaviors and is small enough to provide sufficient nutrient transport to cells within hydrogels (Figure 1) [136,142,143]. Thus, the chip platform is great for assay miniaturization, as biological assays can be performed at one hundredth the volume of the same test performed on a 96-well plate. Additionally, when using the microwell chip as a vessel for containing media and other reagents, it is easier to change growth media and modify culture conditions without disturbing the cells as is the case for well plate experiments.
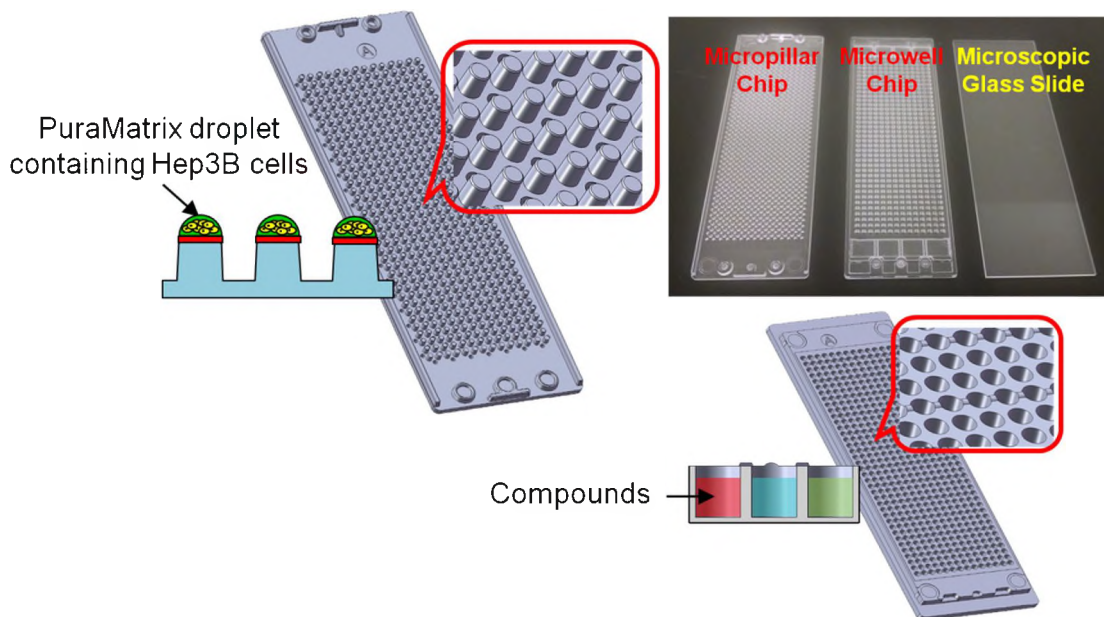
Figure 1. Schematic representation of the micropillar and microwell chip platform for use in Hep3B cell encapsulation in PuraMatrix and compound toxicity assessment.

In the present study, PuraMatrix was explored as a hydrogel matrix for cell encapsulation on the micropillar chip. PuraMatrix is a peptide hydrogel containing a repeating sequence of arginine-alanine-aspartic acid-alanine (RADA) residues. These residues are analogous to the arginine-glycine-aspartic acid (RGD) sequence found in the tissue ECM that cell-surface integrins bind to, which makes PuraMatrix an ideal synthetic

hydrogel for recapitulating *in vivo* cell-ECM interactions. While the study of PuraMatrix has been performed for use in neural cell lineages [111,144] and tissue vascularization [103], limited work has been performed with hepatic cell lineages for HTS of potential drug candidates. However, PuraMatrix has been used for tumor spheroid models in conjunction with other hydrogels [145], and it has been shown that PuraMatrix is positively associated with albumin synthesis compared to other hydrogels, a function specific to hepatocytes [115]. Additionally, PuraMatrix has been shown to improve the formation of bile canaliculi in 3D [146]. Another major motivation for using PuraMatrix is its peptide structure, which makes encapsulated cells amenable to viral transduction. This is in contrast with alginate, which has been used successfully in the culture of hepatic cell lines on the micropillar/microwell chip in the past, but has not been successfully used for adenoviral transduction [136,143].

The goal of the research was to establish the use of PuraMatrix as a viable hydrogel for hepatic cell culture in 3D on the micropillar chip and prove that control of protein expression *via* adenoviral transduction into hepatic cells is possible while cells are encapsulated in hydrogels. Surface chemistry was optimized with several amphiphilic polymers with maleic anhydride groups for robust spot attachment, and gelation mechanisms were compared by printing with various salts and ionic polymers. With optimized 3D cell culture conditions, Hep3B cells encapsulated in PuraMatrix and cultured in 3D were exposed to recombinant adenoviruses to demonstrate on-chip gene transduction. Finally, 3D-cultured Hep3B cells in PuraMatrix on the chip cells were tested with several model compounds at various concentrations, and IC_{50} values obtained were compared with literature *in vivo* and *in vitro* toxicity values.

2.2. Materials and Methods

2.2.1. Materials

Polyethylene oxide-maleic anhydride copolymers including ACM1510, ADM1510, AEM1510, AKM0530, and AKM1510 used for surface coating of the micropillar chip were kindly supplied from Nippon Oil and Fat Co., Japan. Poly(maleic anhydride-*alt*-1-octadecene) (PMA-OD) and poly(maleic anhydride-*alt*-1-tetradecene) (PMA-TD) were purchased from Sigma Aldrich. The chemical formulae of the compounds are given in Figure 2. PuraMatrix peptide hydrogel was obtained from BD Biosciences. Hep3B human hepatoma cell line and human embryonic kidney (HEK293) cells were obtained from ATCC (catalog nos. HB-8064 and CRL-1573 respectively), as were all cell culture ingredients, including growth media, sera, and antibiotics. The micropillar and microwell chips were manufactured by MBD Korea (Suwon, South Korea). Model compounds including acetaminophen, lovastatin, rotenone, tamoxifen, menadione, and sodium citrate were obtained from Sigma Aldrich. Sucrose, Dulbecco's phosphate-buffered saline (D-PBS), sodium alginate, $BaCl_2$, NaCl, and $CaCl_2$ were also obtained from Sigma Aldrich. Calcein AM and ethidium homodimer were obtained from ThermoFisher. 96-well plates and 0.01% (w/v) poly-L-lysine (PLL) solution were obtained from ThermoFisher.

2.2.2. Cell culture

Hep3B cells at the passage number between 15-50 were cultured in T75 flasks with Roswell Park Memorial Institute (RPMI) 1640 medium supplemented with 10% (v/v) fetal bovine serum (FBS). For chip experiments, Hep3B cells were cultured in complete RPMI

containing 10% (v/v) FBS, 1% (v/v) penicillin and streptomycin (P/S), and 0.1% (v/v)

gentamycin. HEK293 cells at the passage number between 2-10 were cultured in eagle's

minimum essential medium (EMEM) with 10% (v/v) FBS for the amplification of

recombinant adenoviruses and the measurement of viral titers.

A   B
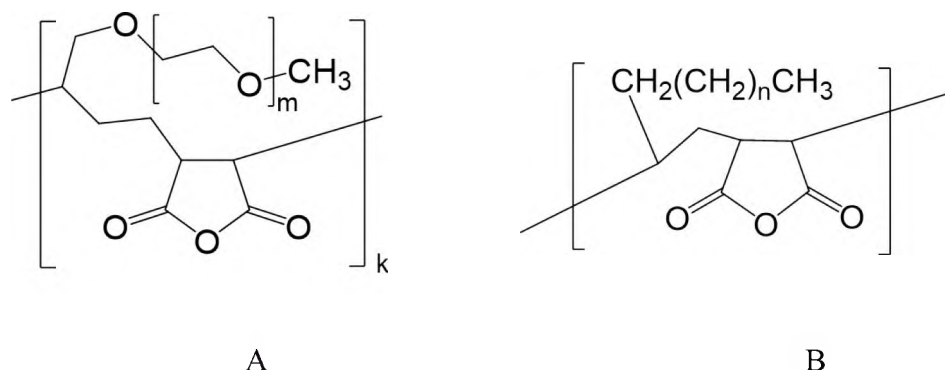
Figure 2. Chemical structures of amphiphilic polymers used to coat the micropillar chip:
(A) Polyethylene oxide-maleic anhydride copolymers including ACM1510, ADM1510,
AEM1510, AKM0530, and AKM1510 which are the names designated by the company
manufacturing the polymers. (B) Poly(maleic anhydride-*alt*-1-octadecene) (PMA-OD) and
poly(maleic anhydride-*alt*-1-tetradecene) (PMA-TD).

2.2.3. Microwell chip preparation

For all experiments, a 950 nL/microwell printing protocol was used to print growth

media into the microwell chips. The microwell chips were always warmed 30-60 min in

humidified, air-tight chambers to 37°C in a Heracell 150i CO_2 incubator from

ThermoFisher before stamping printed cell cultures. All printing protocols were performed

while keeping the chip deck at 7°C to avoid water evaporation.

2.2.4. Optimization of surface coating of the micropillar chip

Ethanol was used to dissolve all the polymers used for surface coating. All stock

solutions contained 1% (w/v) polymer. Hydrophobicity of the polymers was tested by

attempting to dissolve 1% (w/v) polymers in water under continuous stir for 24 h. In addition, 0.1% (w/v) polymer solutions in ethanol were prepared for surface coating of the micropillar chips. A shallow-well staining plate was filled with 2 mL of 0.1% (w/v) polymer solution in ethanol per chip, and then the micropillars briefly submerged in the plate. The micropillar chips were air dried for a minimum of 1 h before dispensing 40 nL of 0.25% PuraMatrix onto the chips using a S+ microarray spotter (Samsung ElectroMechanics, Co. or SEMCO). Samples were dried again for a minimum of 4 h. Samples that were not printed with cells within 24 h were stored in the refrigerator for future use. Hep3B cells were printed at a concentration of 4 million cells/mL in 0.25% PuraMatrix containing 10% (w/v) sucrose onto the micropillar chips using a 40 nL/micropillar printing protocol with the S+ microarrayer. Following printing, Hep3B cells were allowed to sit for 5 min before sandwiching (or "stamping") with pre-warmed microwell chips containing complete RPMI. The sandwiched chips were kept in humidified chambers at 37°C and 5% CO_2 for 30 min before stamping with a fresh, pre-warmed microwell chip containing complete RPMI. Hep3B cells in PuraMatrix were then incubated 48 h in the microwell chips containing complete RPMI before live-dead cell staining was performed. Hep3B cells were imaged with a multiband filter using an initial gain of 150. Both staining and imaging protocols are detailed near the end of the experimental section. In addition to cell viability, the formation of bubbles was characterized as a measure of air-liquid interfaces generated by the interaction of the polymer with the cell culture media. Spot detachment was also quantified by calculating the percentage of micropillars that did not maintain covalent attachment with the hydrogel.

2.2.5. Printing of PuraMatrix gelation agents

33

Our optimized surface coating chemistry is provided in Figure 3. Micropillar chips were coated with 0.01% (w/v) PMA-OD in ethanol and dried under ambient air for 4 h. To enhance affinity between PMA-OD coating and cell-PuraMatrix spots, 0.25% PuraMatrix in sterile deionized water was printed on the micropillar chips using the S+ microarrayer at 60 nL/micropillar and dried under ambient air for 4-24 h. 60 nL/micropillar of gelation agents were printed onto the micropillar chips and dried under ambient air for 4 h. Potential gelation agents tested were sterile deionized water (control), Dulbecco's phosphate-buffered saline (D-PBS), 0.01% alginate, 0.01% PLL, ¼ diluted saline solution (containing 37.5 mM NaCl and 5 mM $CaCl_2$), and 25 mM $BaCl_2$. Microwell chips were printed with 950 nL of complete RPMI per microwell using the S+ microarrayer, which were warmed to 37°C in a 5% CO_2 incubator 1 h before stamping with micropillar chips. To reduce the viscosity of PuraMatrix, 1% (w/v) stock of PuraMatrix was sonicated for 30-60 min before printing. Hep3B cells were trypsinized and centrifuged at 200 g for 4 min using Eppendorf centrifuge 5702. The supernatant was discarded, the cell pellet was resuspended in RPMI 1640 containing 10% FBS, and then the cell number was counted with an ORFLO Moxi Z Mini Automated Cell Counter (MXZ000). Hep3B cell suspension was centrifuged again at 200 g for 4 min. The supernatant was discarded, and the cell pellet was gently resuspended in 7 mL of warmed 10% sucrose. The cells were centrifuged again at 200 g for 5 min. The supernatant sucrose was discarded, and Hep3B cells were resuspended in 10% sucrose to a final concentration of either 8 million or 12 million cells/mL. The resuspended cells were combined with 20% sucrose and 1% PuraMatrix in a 2:1:1 ratio to create a final cell sample containing either 4 million or 6 million cells/mL in 0.25% PuraMatrix containing 10% sucrose. 60 nL of these cell samples were printed onto each micropillar of the chip.

34

Micropillar chips were stamped with microwell chips containing complete RPMI and incubated at 37°C in a 5% CO_2 incubator for 30 min. For the 6 million cells/mL micropillar chips and some of the 4 million cells/mL micropillar chips, there was a second stamping and 30 min incubation with microwell chips containing complete RPMI, as this stamping process serves to neutralize the highly acidic PuraMatrix. After the first/second rinsing, Hep3B cells were stamped again with a microwell chip containing complete RPMI and incubated at 37°C in a 5% CO_2 incubator for 72 h. Micropillar chips were subsequently stained with a dye solution containing 0.5 μM calcein and 0.5 μM ethidium homodimer in D-PBS. Cell images were acquired using a S+ scanner (SEMCO) under 4x magnification, multiband filter, and a gain of 150. Cell viability was quantified using the ColorSplit macro in ImageJ to quantify the green fluorescence intensity, and spot detachment was counted on the micropillar chip for each salt condition used.
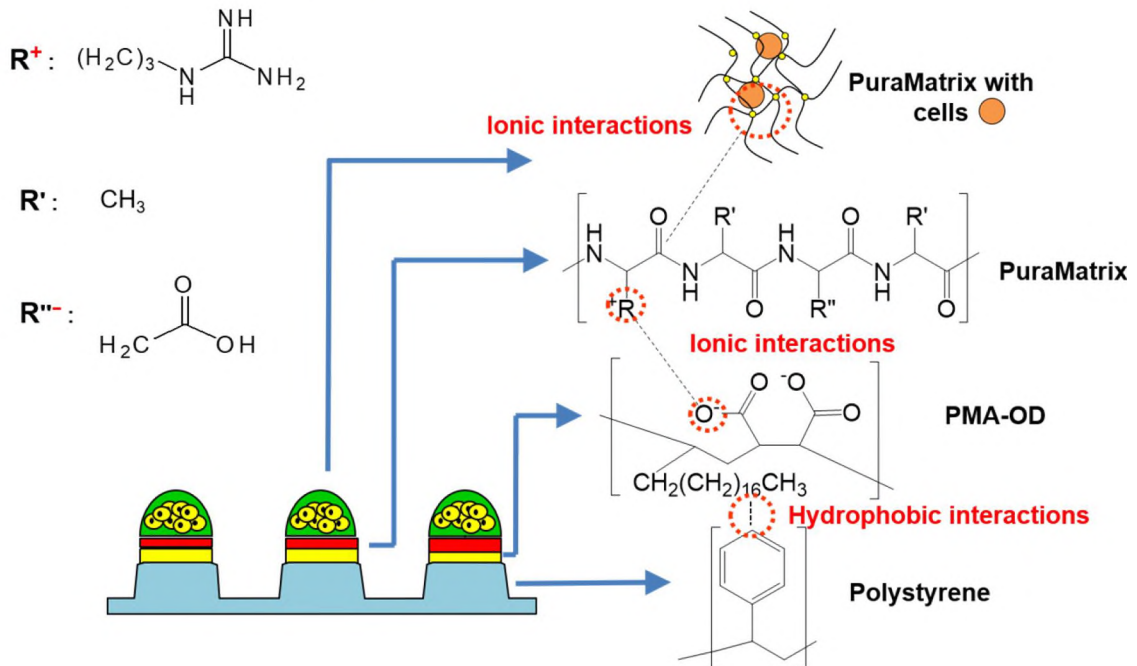
Figure 3. Optimized surface chemistry for printing Hep3B cells encapsulated in PuraMatrix onto the micropillar chip.

2.2.6. Adenoviral expansion and titering

35

Genes for green fluorescent protein (GFP) and red fluorescent protein (RFP) were coded into an adenoviral expression system using the protocols from Kwon *et. al.* to generate recombinant adenoviruses carrying genes for GFP (Ad-GFP) and RFP (Ad-RFP) [136]. HEK293 cells were used to expand the adenoviruses. T75 flasks were seeded at 50-70% confluency and grown for twenty-four hours in EMEM containing 10% FBS before exposure to the viruses. Cells were incubated with the viruses and serum-free EMEM using a multiplicity of infection (MOI) of fifty for 24 h. The growth medium was removed and replaced with serum-free EMEM. When significant cytopathic effect (CPE) was observed (usually 2-4 days after the viral particles were removed), the infected HEK293 cells and media were removed from the flask. To lyse the cells and release the viral particles into the media, cells underwent three rapid freeze-thaw cycles where cells were frozen at -80°C for 30 min, followed by thawing at 37°C for 10 min. The cells were centrifuged at 1500 g for 5 min at 4°C to remove the debris. The supernatant was placed in a centrifugal filter unit with a molecular weight cut-off (MWCO) of 100,000 kDa and centrifuged at 4,000 g at 4°C for 45 min. Viral particles were washed twice with 10 mL bronchial epithelial cell growth medium (BEGM) without additives using the centrifugal filter unit before being resuspended in 1 mL serum-free BEGM. To determine adenoviral titer, an end-point dilution assay was used, utilizing HEK293 cells to determine CPE [147]. Final Ad-GFP and Ad-RFP stock concentrations ranged between 10^8 and 10^{10} PFU/mL.

2.2.7. Adenoviral transduction in PuraMatrix

Hep3B cells were printed using the optimized gelation agent (water) as described earlier in the materials and methods section, using two media washes and a seeding density

of 6 million cells/mL. After 24 h of incubation in complete RPMI, 950 nL of the adenoviruses in complete RPMI were printed into microwell chips, and Hep3B cells were exposed to various MOI of the adenoviruses for 24 h. Following adenoviral exposure, the microwell chip was discarded and replaced with a microwell chip containing fresh complete RPMI. The micropillar chips were incubated for additional 48 h before being dried under ambient air in a dark environment for another 24 h. Fluorescent cell images were obtained with the S+ scanner using a multiband filter, and individual green and orange filters at 4x magnification. A gain of 100 was used to examine fluorescence.

2.2.8. Drug toxicity assessment

Hep3B cells were printed at the optimum condition described in the adenoviral transduction procedure. After 24 h of incubation, six model compounds were printed into microwell chips at six dosages per compound. Tested compounds include acetaminophen (2.10 - 2125 μM), lovastatin (0.03 - 29.5 μM), rotenone (0.03 - 29.5 μM), tamoxifen (0.03 - 29.5 μM), menadione (0.04 - 44.3 μM), and sodium citrate (1.38 - 1417 μM). Compounds were four-fold serially diluted in complete RPMI starting with the highest concentration of a tested compound to develop dose-response curves. Following 48 h of Hep3B cell exposure to the compounds, the cells were stained and imaged for viability as described in Section 2.9.

2.2.9. Live-dead cell staining and image acquisition

Micropillar chips were rinsed *via* submersion in 5.5 mL of D-PBS in a deep-well staining plate for 5 min twice. Any excess D-PBS solution from the chip was drained by tilting the chip at an angle of 45° and removing the remaining solution from the side of the

chip with a paper towel. A dye solution containing 0.5 μM calcein and 0.5 μM ethidium homodimer in D-PBS was used for live-dead cell staining. Hep3B cells were stained in a shallow-well staining plate in the dark using 2 mL of the dye solution per well for 1 h. The cells were then rinsed with 5.5 mL of D-PBS in the deep-well staining plate for 15 min twice. Following the last wash, the excess water was drained from the chip and the cells were left to dry overnight in the dark before imaging with the S+ scanner. Cell images were acquired using the S+ scanner under 4x magnification, multiband filter, and a gain of 150.

2.2.10. Analysis of cell images

All images were separated for analysis based on color using the ImageJ plugin in "ColorSplit", which splits the colors of individual images into distinct red, green, and blue emission spectra. Each image underwent a basic background subtraction, followed by thresholding using the moments method [148]. Finally, the total fluorescence in the image was quantified using an integrated density function.

2.2.11. Statistical analysis

Fluorescence intensities obtained from Hep3B cells exposed to media alone (control) and compounds were plotted as a function of dosages using S+ chip analysis software to generate dose response curves and calculate IC_{50} values [141]. In addition, average, standard deviation (SD), and standard error mean (SEM) of sample fluorescence were calculated for analysis of variance (ANOVA) using GraphPad Prism 4. Samples exposed to various compounds underwent dose-response curve plotting using the S+ chip analysis software.

2.3. Results

2.3.1. Optimization of polymer coating on the micropillar chip for PuraMatrix attachment

The amphiphilic polymers chosen for surface coating of the micropillar chip include maleic anhydride analogs. The carboxylic groups from hydrolyzed maleic anhydride may have ionic interactions with the positively charged arginine residues on PuraMatrix, while the main alkyl and ethylene/propylene oxide chains may have hydrophobic interactions with the micropillar chip made of polystyrene (Figure 2). This results in a situation where these polymers can anchor PuraMatrix onto the surface of the micropillar chip. Additionally, while PuraMatrix contains amine functional groups, these polymers can conjugate to any hydrogel containing amine functional groups, or cross-linking molecules containing amine functional groups such as poly-L-lysine.

The results of the polymer coating experiment on micropillar chips are summarized in Table 2. It was found that six out of the seven tested polymers were soluble in ethanol. The one that was insoluble in ethanol, AKM1510, was also insoluble in water; this polymer was subsequently excluded for further surface coating experiments. Of the six remaining polymers, three dissolved in water (ADM1510, AEM1510, and AKM0530), while three formed colloidal suspensions (ACM1510, PMA-OD, and PMA-TD) at a 0.1 % (weight per volume, or w/v) concentration. The initial polymer coating condition at 0.1% (w/v) proved to be too toxic to Hep3B cells presumably due to polymer leaching so that the concentration was diluted to 0.01% (w/v) to minimize basal toxicity.

Table 2. Polymers used for coating the micropillar chip made of polystyrene.

Polymers used for coating	Length of chains [a]	EO/AO [b] (%)	Solubility in ethanol	Solubility in water	Bubble formation	Spot detachment (%)
ACM1510	m = 26 k = 10	20	+ [c]	–	++	1 ± 0.5 [d]
ADM1510	m = 27 k = 10	30	+	+	+	13 ± 5
AEM1510	m = 28 k = 10	40	+	+	+	19 ± 12
AKM0530	m = 10 k = 30	100	+	+	–	12 ± 15
AKM1510	m = 33 k = 10	100	–	–	N/A	N/A
PMA-OD	n = 16	N/A	+	–	–	0
PMA-TD	n = 12	N/A	+	–	+	0
No coating	N/A	N/A	N/A	N/A	–	25 ± 16

[a] Chains refer to the number of repeating units in the structures described in Fig 2.

[b] Ethylene oxide (EO), alkylene oxide (AO), propylene oxide (PO). AO = EO + PO. For where these oxides are in the polymer, see Fig 2.

[c] "++" denotes the aspect was greatly observed above the normal, "+" denotes the aspect was somewhat observed, and "–" denotes that the aspect was not observed.

[d] "±" denotes standard deviation (SD)

For cell-based assays on the micropillar chip, bubble formation and spot detachment were tested. Air bubbles entrapped between the hydrogel spot on the micropillar chip and the growth media in the microwell chip imply that the surface of polymer coating may not be uniform, or a polymer may be unsuitable for coating. With excess air bubbles, cells encapsulated in hydrogels may experience nutrient deficiency and could potentially dry out. In addition, robust spot attachment on the micropillar chip is critical for 3D cell culture and imaging. Uniform surface coating of a polymer and the affinity of a bottom layer between the PuraMatrix spot and the polymer-coated surface of the micropillar chip play a significant role.

When examining the chips, bubble formation was only absent in the cases of AKM0530 and PMA-OD, while excess bubbles were observed with ACM1510 coating. This result indicates that there is no correlation between bubble formation and the hydrophobicity of the coating polymers or their alkyl/alkylene oxide chain lengths. We suspect bubble formation occurs due to the presence of dissolved O_2 in the media that could collect at the surface of the micropillar chips though we could not tie this to a particular property associated with any of the dissolved polymers.

When spot detachment was calculated, it was found that PuraMatrix detached more readily with hydrophilic polymer coating over hydrophobic polymer coating. We hypothesize that this detachment was due to relatively high solubility of the hydrophilic polymers in growth media, leading to weak interactions between PuraMatrix and the surface of the micropillar chip. In contrast with the hydrophilic polymers, the hydrophobic polymers will be remained intact on the surface of the micropillar chip for interactions with PuraMatrix. In the case of the no-surface treatment control, we found that spot attachment was reduced although bubble formation was not an issue. Overall, PMA-OD found to be the best coating with PuraMatrix due to robust spot attachment and no bubble formation. Therefore, all subsequent experiments were conducted on the micropillar chip coated with 0.01% (w/v) PMA-OD (Figure 3).

2.3.2. Salts and ionic polymers for gelation of PuraMatrix and enhanced spot attachment

Tests were performed to determine if there are additional salts or ionic polymers necessary to ensure robust spot attachment immediately after cell printing in PuraMatrix. The results of using the various salts and ionic polymers as gelation mechanisms are

summarized in Figure 4. In general, salts in growth media are used as a gelation agent for PuraMatrix as they facilitate the self-assembly of the hydrogel, resulting in a β-sheet type structure [149,150]. The bonds that hold the hydrogel together include ionic interactions between the aspartic acid and arginine residues, hydrophobic interactions between the alanine residues, and hydrogen bonding associated with the β-sheet type structure [151–154]. Significant spot detachment was only observed when D-PBS without Ca^{2+} and Mg^{2+} was printed on 0.01% (w/v) PMA-OD coating to assist PuraMatrix gelation (Figure 4B). It is hard to deduce why D-PBS was so unfavorable for PuraMatrix spot attachment given that the diluted saline and $BaCl_2$ solutions showed high spot attachment levels. Perhaps, excess salt crystals formed on the surface of the micropillar chip due to high concentration of NaCl (137 mM) in D-PBS prohibit robust attachment of PuraMatrix droplets on the surface. Interestingly, PuraMatrix droplets were robustly attached on the surface of the micropillar chip without any salts and ionic polymers added, which indicate that salts in growth media are sufficient to form PuraMatrix gelation, and PuraMatrix spots printed are adherent to PMA-OD coating.

Day 0   **Day 1**   **Day 2**   **Day 3**

A

B   C
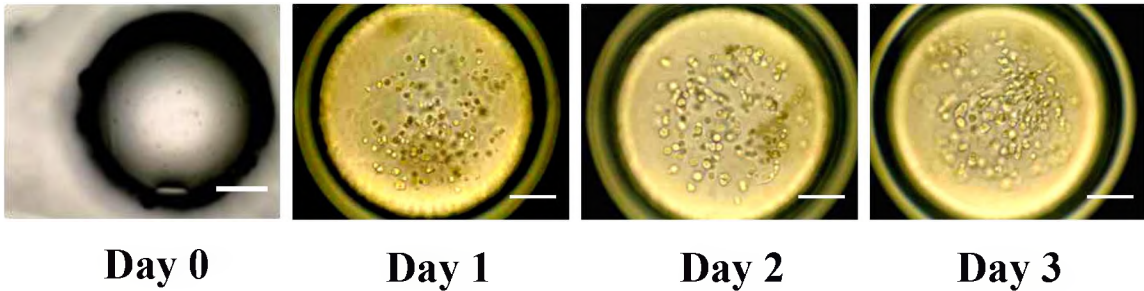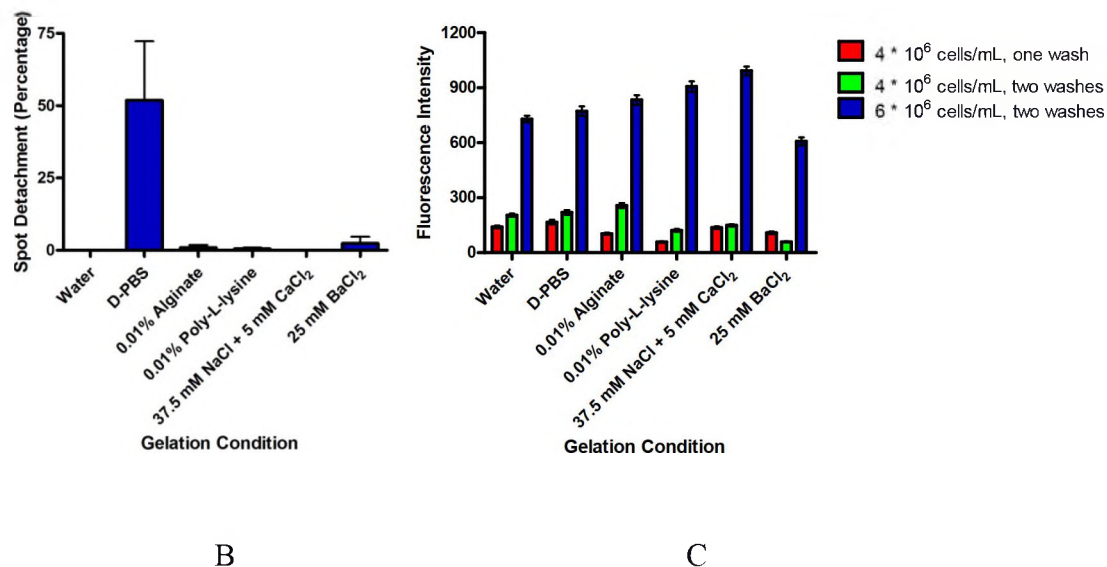
Figure 4. (A) Bright-field microscopic images of Hep3B cells in PuraMatrix printed on the micropillar chip and cultured over time in combination with the microwell chip. The scale bar is 200 μm. (B) Detachment of PuraMatrix droplets containing Hep3B cells (60 nL/spot at 6 million cells/mL) as a function of salts and ionic polymers used for PuraMatrix gelation after two media washes. (C) Hep3B cell viability as a function of salts and ionic polymers used at different cell seeding and wash conditions. Error bars represent SEMs, n = 72.

Hep3B cell viability was measured on the salt and ionic polymer layer at different cell seeding density and media wash conditions (Figure 4C). Overall, Hep3B cells were viable within PuraMatrix, and cell viability was somewhat reduced in the presence of 25 mM $BaCl_2$ and 0.01% (w/v) PLL, but not significantly in either. As PuraMatrix is acidic, we decided to test the effects of additional growth media rinsing in the microwell chip and high cell seeding density. Briefly, the mixture of PuraMatrix and Hep3B cells was prepared by rinsing the Hep3B cell pellet with sucrose, centrifuging the cell-sucrose mixture, and then resuspending the cell pellet in the mixture of PuraMatrix-sucrose at a seeding density of 4 or 6 million cells/mL. To further neutralize acids in PuraMatrix, freshly printed Hep3B cells on the micropillar chip were rinsed with an additional microwell chip containing fresh growth media 30 min after cell printing. Overall,

43

increasing from one to two media washes increased Hep3B cell viability as described in manufacturer's instruction for 96-well plate cultures. In addition, we noticed that additional sucrose rinsing to remove salts in growth media can disturb cell membrane integrity, leading to low cell viability. Therefore, sucrose rinsing was performed once very gently without vigorous pipetting. Finally, cell seeding density greatly affected the viability of Hep3B cells in PuraMatrix on the chip. Increasing cell seeding density from 4 to 6 million cells/mL resulted in higher cell viability and increased reproducibility. The biggest contributors towards improving cell viability involved increasing the number of media washes and the cell seeding density.

Since additional salts and ionic polymers did not significantly enhance spot attachment and cell viability, we decided to eliminate this step. Therefore, all subsequent experiments were conducted on the 0.01% (w/v) PMA-OD-coated micropillar chip with 60 nL of 6 million Hep3B cells/mL (360 cells seeded per micropillar) after two media washes. Hep3B cells in PuraMatrix formed 3D spheroid structure over time in this condition (Figure 4A).

2.3.3. Adenoviral transductions

With the optimized Hep3B cell culture condition in PuraMatrix on the chip, adenoviral transduction was performed in the presence of recombinant adenoviruses carrying genes for green fluorescent protein (Ad-GFP) and red fluorescent protein (Ad-RFP), and the results are shown in Figure 5. Adenoviral transduction is important as a method to efficiently deliver genes such as metabolizing enzyme genes and control protein expression *in vitro*, as to develop predictive cell models for testing the toxicity of

compounds [136]. However, adenoviral gene delivery is often difficult in 3D systems due to strong interactions of virus particles with a hydrogel matrix and diffusion issues into 3D constructs. Unlike alginate, PuraMatrix successfully facilitated adenoviral gene transduction on 3D-cultured Hep3B cells as demonstrated with individual Ad-GFP and Ad-RFP (Figure 5). Hep3B cells transduced with both Ad-GFP and Ad-RFP exhibited a yellow-orange color, indicating that both green and red fluorescent proteins were simultaneously expressed and detected by a multiband filter. Analysis of fluorescence intensity at different MOI showed that both GFP and RFP exhibited dose-dependent fluorescence intensity changes, with the exception that the 10 MOI Ad-RFP showed slightly reduced fluorescence compared to the 5 MOI Ad-RFP alone. This may be caused by red fluorescence generally being weaker than green fluorescence, particularly when cells have been infected with both viruses and are exhibiting yellow fluorescence.
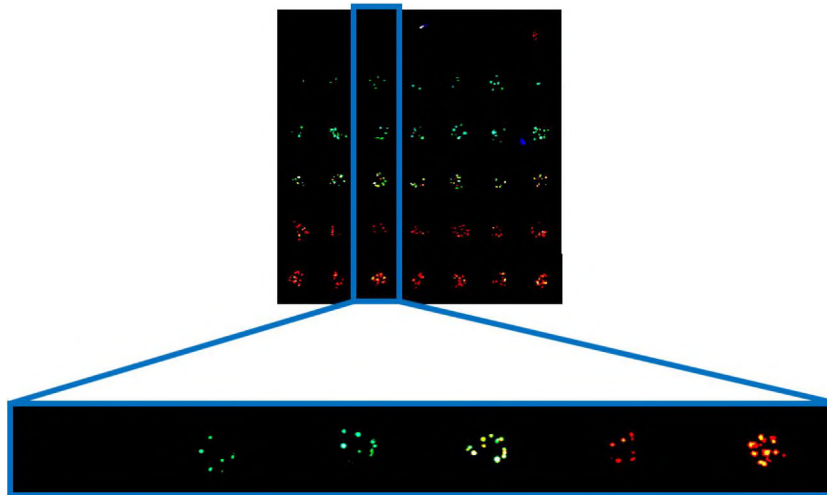
A
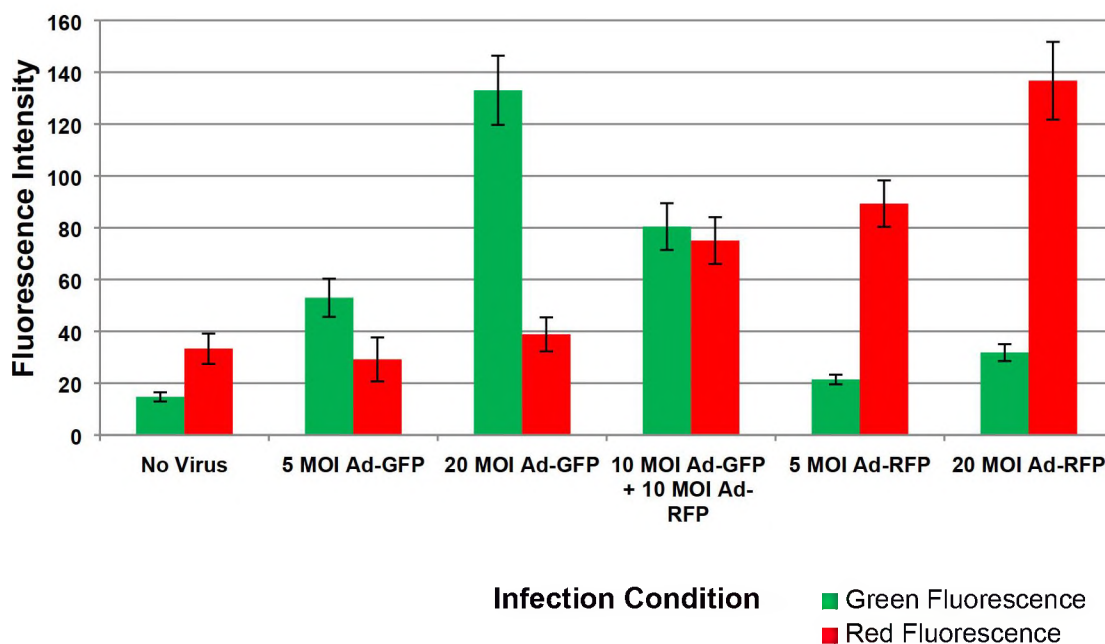
B

Figure 5. Adenoviruses transduced into Hep3B cells encapsulated in PuraMatrix on the micropillar chip. A) From left to right, images showing transduction in the presence of no virus, 5 MOI Ad-GFP, 20 MOI Ad-GFP, 10 MOI Ad-GFP + 10 MOI Ad-RFP, 5 MOI Ad-RFP, and 20 MOI Ad-RFP. B) Corresponding fluorescence intensity measurements observed on the micropillar chip. Error bars represent SEMs, n = 72.

2.3.4. Drug toxicity assays

Six model compounds were tested on 3D-cultured Hep3B cells in PuraMatrix to demonstrate the capability of the chip platform for rapid toxicity assessment (Figure 6). The IC_{50} data from 3D-cultured Hep3B cells on the chip were compared with the *in vitro* IC_{50} data from HepG2 cell monolayers in 2D, IC_{50} values from human hepatocytes, *in vivo* human C_{max} values, and *in vivo* LD_{50} data from mice exposed orally to these compounds (Table 3). The *in vivo* data were sourced from Sigma for acetaminophen, lovastatin, Cayman Chemicals for rotenone and tamoxifen, Applichem for menadione, and Sagent Pharmaceuticals for sodium citrate. Acetaminophen and sodium citrate were found to be

46

non-toxic for the range of compound concentrations tested, which is consistent with previous experiments in 2D using the micropillar chips [136], and with other previously cited literature values from 2D experiments [152–155]. All drug concentrations tested had IC_{50} values within one order of magnitude of *in vitro* toxicity data, with Hep3B cells encapsulated in PuraMatrix exhibiting normal dose-response type behavior, with increased concentrations of compounds reducing cell viability and the middle range of concentrations producing a more dramatic shift in cell viability. These results point towards the ability of Hep3B cells encapsulated in PuraMatrix to be used to assess potential drug toxicity in the liver.

Table 3. Comparison of IC_{50} and LD_{50} values of the model compounds.

Compound	3D Hep3B IC_{50} from the chip (μM)	2D HepG2 IC_{50} from literature (μM)	Human Hepatocyte IC_{50} from literature (μM)	C_{max} from literature (μM)	Mouse oral LD_{50} from MSDS (mg/kg)
Acetaminophen	>2100	630 (Neutral red assay) [154]	28200 (MTT) [156]	130 [157,158]	338
Lovastatin	23	20 ± 3.7 (MTT) [159]	96 (CYP3A4 activity) [160]	0.01 [157,158]	>1000
Rotenone	2.4	0.5 ± 0.1 (Fluo-4 AM) [155]	1.0 (CellTiterGlo) [161]	50 [155,157,158]	2.8
Tamoxifen	4.3	60 ± 5.9 (Fluo-4 AM) [155]	21.5-98.4 (CellTiterGlo) [162]	0.4 [155,157,158]	2200
Menadione	1.2	13 (Luc-CEE) [163]	4.2 (TMRM) [164]	5 [157,158,165]	500
Sodium Citrate	>1400	>1000 (Fluo-4 AM) [155]	>1000 (Hoechst) [166]	N/A [155,157]	5000
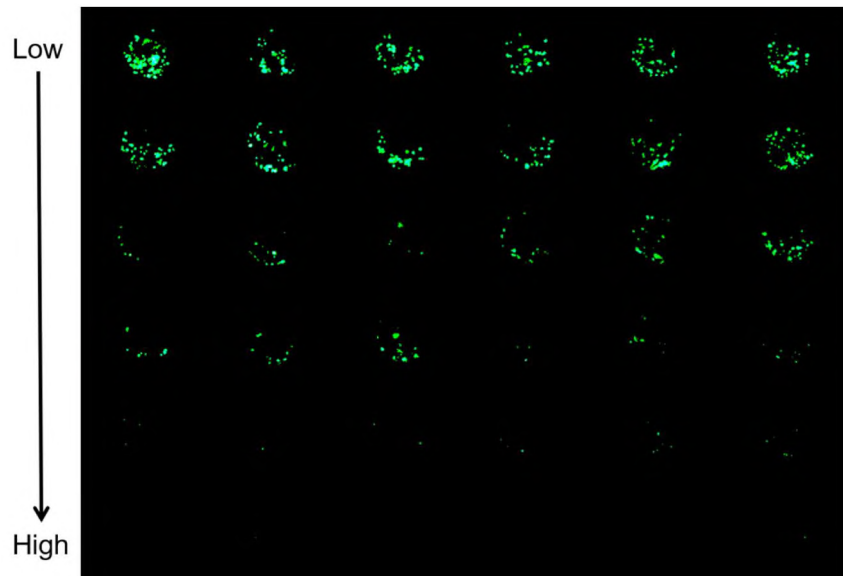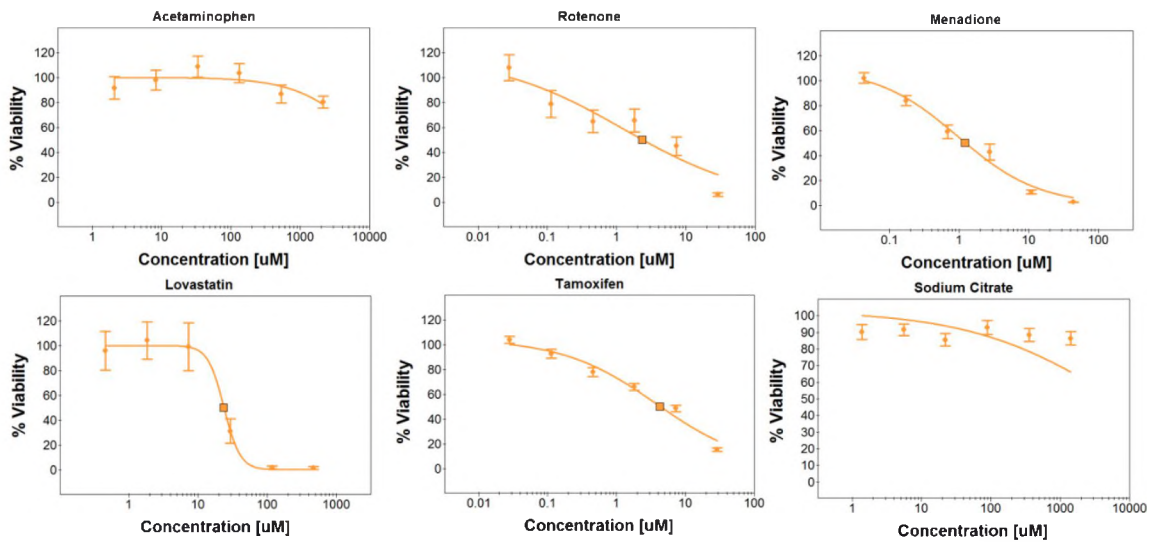
Figure 6. (A) Representative image of Hep3B cells encapsulated in PuraMatrix treated with menadione (low dosage: 43 nM, high dosage: 44.3 µM). (B) Dose response curves of Hep3B cells exposed to the model compounds while encapsulated in PuraMatrix on the micropillar chip, n = 12.

2.4. Discussion

The goal of this research was to design a chip platform containing hepatic cells in a 3D biomimetic microenvironment that can be suited for rapid assessment of potential drug candidates and controlled expression of genes *via* viral transduction. PuraMatrix was selected as an analog for cellular ECMs as the peptide structure is used for anchoring sites of the cellular integrins to attach [111,144]. Generally, PuraMatrix has been used for applications in neural tissue engineering, as the hydrogel has mechanical properties similar to that of other hydrogels used for neural ECM substitutes [111]. PuraMatrix also forms fibrous strands similar to that of the tracks found in the white matter of the brain [111]. While the liver does not necessarily contain the exact architecture of these tracks, integrins are important for cells to adhere to the ECM in any tissue or organ.

Initially, surface chemistry needed to be optimized for PuraMatrix attachment onto the micropillar chip. This part was of particular importance as a good attachment serves to provide numerous replicates for experiments, making the micropillar chip a suitable platform for cell culture and imaging. Additionally, surface chemistry developed may be applied towards hydrogels other than PuraMatrix. In particular, coating the surface of the micropillar chip with 0.01% (w/v) PMA-OD in ethanol creates a favorable interaction between the micropillars and the amine-reactive polymers and hydrogels as now the micropillar chip has been functionalized with amine-reactive maleic anhydride groups, while there is an anchor formed via the hydrophobic interactions between the micropillar chip made of polystyrene and the alkyl side chains from PMA-OD. Since spot detachment was positively correlated with hydrophobicity, this makes PMA-OD a good choice for ensuring the robustness of the surface chemistry. Ultimately, PMA-OD was a better choice

than ACM1510 or PMA-TD because of the lack of bubbles formed when using PMA-OD, which means that PMA-OD also does not impede the ability of cells in hydrogels to come into contact with media, creating an environment ideal for microscale 3D cell culture.

As another part of this study, it was necessary to observe if printing salts and ionic polymers on the surface of the micropillars will result in improved attachment of PuraMatrix. PuraMatrix forms a gel in the presence of salts, which promotes ionic interactions between arginine and aspartic acid; thus, Hep3B cells suspended in PuraMatrix must be pretreated with 10% (w/v) sucrose which is both isotonic and non-ionic. It was initially hypothesized that printing salts would hasten the gelation process once Hep3B cells in PuraMatrix were printed on the micropillar chip. In addition, a pre-printing step of diluted PuraMatrix was used to provide high affinity to the PMA-OD-coated micropillars for which the cell-laden PuraMatrix may attach. The results showed that printing of the salts and ionic polymers seems to be unnecessary as a method for improving surface attachment. In the case of D-PBS, the printing of high concentrations of salts significantly increased the detachment of PuraMatrix spots, and thus decreased the number of spots that could be analyzed. The results indicate that salts in growth media are sufficient for gelation, and PuraMatrix gelation prior to immersion in growth media is unnecessary presumably due to high affinity of the PuraMatrix bottom layer.

More importantly, PuraMatrix exists at an acidic pH of 2-3, which is toxic to Hep3B cells and needs to be neutralized for 3D cell culture. This is supported by two results: 1) neutralizing PuraMatrix with two media washes provided more consistent, highly viable cells and 2) increasing the cell density from 4 million cells/mL to 6 million cells/mL effectively increased the exhibited green fluorescence intensity (and thus, the amount of

50

live cells) and decreased in spot-to-spot variation. Both results were independent of the salts and ionic polymers used to initiate gelation. While the 3D cell culture on the micropillar chip focused on optimization of gelation conditions for PuraMatrix, previous experimental protocols utilized PBS [103,149] or culture media [111,149] to initiate gelation. The results of the experiments performed on the micropillar chip indicate that D-PBS is not a suitable gelation agent for PuraMatrix for this scaffold, indicating the importance of using divalent cations as supposed to monovalent cations for improved surface attachment and gelation of PuraMatrix.

The major drawback of using PuraMatrix is that the preparation for cell printing relies on several steps that could be toxic and time-sensitive. This may make PuraMatrix unsuitable to be used for cell types that may be averse to these harsh conditions. It because of the low pH of PuraMatrix that it was necessary to subsequently increase cell seeding density in the spots and wash each chip twice with excess growth media to neutralize the pH of PuraMatrix. While these steps did make results for subsequent experiments more consistent, and improve general culture conditions, Hep3B cell growth seems to be generally less than that experienced in other hydrogel cultures [143]. This is particularly apparent with less spheroid formation, a general indicator that Hep3B cells are thriving in 3D.

The major advantage towards using PuraMatrix is the fact that it can be used to encapsulate cells while having minimal interactions with viral capsids, allowing for controlling the expression levels of key enzymes [136,167] Adenoviruses were designed for expansion in HEK293 cells as an expression vector due to their relatively low pathogenicity and their expression is transient in nature [136,143]. The results conclusively

51

show the ability for Hep3B cells to be infected with adenoviruses while encapsulated in PuraMatrix. Additionally, the S+ scanner imaging system can distinguish Hep3B cells expressing GFP and RFP, while the cells exhibited MOI-dependent infection capability. Although Hep3B cells in PuraMatrix on the chip were used for infection with adenoviruses carrying genes for GFP and RFP, our approach could be further expanded to include various other viruses, allowing for control of genetic expression of enzymes and proteins important in drug discovery.

After successful adenoviral transduction, adverse drug responses were monitored *via* Hep3B cell exposure to six model compounds at different concentrations and measured their relative toxicities. Results showed that the IC_{50} values obtained from 3D-cultured Hep3B cells in PuraMatrix were similar to those obtained from HepG2 cells in 2D for four out of six compounds yet not quite perfectly aligned with the toxicity values observed from *in vivo* animal data obtained from the chemical manufacturers [156,159,163]. Additionally, there are differences between C_{max} literature values and the calculated IC_{50} values for Hep3B in PuraMatrix [155,157,158]. These variations can be attributed to the nature of metabolism and clearance being heavily dependent on the genetic makeup of drug metabolizing enzymes (DMEs) and drug transporters. Therefore, *in vivo* toxicity data from animals and humans can be completely different. Among hepatic cell lines, *in vitro* toxicity data can be also varied depending on the levels of DME expression. For example, acetaminophen is a well-known metabolism-sensitive compound, which is activated in the presence of DMEs such as cytochrome P450 (CYP450) isoforms. Unlike primary hepatocytes, Hep3B cells don't express high levels of DMEs [168], leading to no activation of acetaminophen on the chip platform. In addition, tamoxifen is metabolized by a variety

of CYP450 isoforms, a key family of enzymes expressed within the liver [169]. In the cases of Hep3B and HepG2, both cell lines experience significant decreases in the expression of CYP450 2D6 (CYP2D6), the isoform most associated with tamoxifen metabolism [168,169]. Likewise, menadione metabolism is heavily dependent on CYP450s for adequate clearance [170]. In the case of other compounds, significant differences can exist between in $vivo$ and in $vitro$ data because the in $vitro$ experiments cannot account for all drug metabolism. For lovastatin, metabolism occurs both in the liver and the intestine [160]. The ultimate effect of this are multiple cell types that can metabolize a potentially harmful drug, which reduces the toxicity observed in $vivo$ compared to in $vitro$. In the case of other compounds, the results were consistent with both in $vivo$ and in $vitro$ results. This is true for sodium citrate, a generally nontoxic salt, and rotenone, whose mechanism of action affects mitochondria, which is present in many cell types, though in very high levels in hepatocytes [161]. In the case of acetaminophen, the general mechanism of toxicity is also associated with impaired mitochondrial function [171,172]. This is particularly apparent when comparing rat and mouse in $vivo$ results, where rats are less susceptible to oxidative stress from acetaminophen because of their elevated levels of mitochondria per hepatocyte as compared to mice [172]. Overall, the IC_{50} values of tamoxifen and menadione were reduced in the presence of PuraMatrix on the chip as compared to other in $vitro$ data. This could be potentially due to the additive effects of toxicity from the test compounds and PuraMatrix. Since it was necessary to increase cell seeding density to improve Hep3B cell viability on the micropillar chip, it is also possible that cells exhibited a decreased tolerance towards these compounds due to the added stresses. Additionally, these reductions may also be due to the effect of culturing cells in 3D instead of 2D, as cells cultured in 3D

experience cues from more cells than cells grown in 2D, including potential triggers for cell death. Regardless, discrepancies between PuraMatrix, *in vivo*, and other *in vitro* results can be attributed to the varying nature of metabolism presented in these experiments and any stresses associated with using PuraMatrix as a scaffold for Hep3B cell growth.

The developed platform can replicate toxic reactions, but there are some drawbacks to this system. The use of PuraMatrix is tricky as its pH requires several neutralization steps after printing and makes it tricky for use larger scale 3D cultures. Additionally, because it gels in the presence of salts, it necessitates cells to be resuspended in an isotonic, 10 % sucrose solution. This resuspension causes cells to clump and can also be toxic if cells are kept in suspension for long periods of time.

Another drawback is the scale of the platform. The size of the microwell chip and the micropillar chip means total droplet size cannot be greater than 60 nL per spot, or the hydrogel could hit the bottom surface of the microwell chip. Because the droplet is so small in size, the depth in which cells form 3D structures is equal to only two cell diameters. Thus, while there is some 3D organization, the thickness means that drugs can easily diffuse through all cell layers, which is not necessarily the case for larger scale 3D or *in vivo* cell cultures.

2.5. Conclusions

Here, it has been demonstrated that PMA-OD can improve PuraMatrix attachment on the surface of the hydrophobic micropillar chip made of polystyrene. A procedure was optimized by which Hep3B cells encapsulated in PuraMatrix can be cultured on the chip

for low-volume, high-throughput applications. In addition, genetic expression was successfully modified *via* adenoviral transduction of Hep3B cells encapsulated in PuraMatrix on the micropillar chip, which can be potentially extended to gain- and loss-of-function studies such as metabolism-induced toxicity of compounds by over-expressed DMEs or lack of specific DMEs. While toxicity did not perfectly correlate with *in vivo* data, much of this can be attributed to differences between *in vivo* and *in vitro* metabolism and its contribution to toxicity. Potential variations between *in vitro* data can be associated with stresses put on cells encapsulated in PuraMatrix, or differences between cell types and the comparison of cells in 2D vs. cells in 3D.

CHAPTER III

OPTIMIZATION OF OXYMETHACRYLATED ALGINATE (OMA) FOR USE IN MINIATURIZED 3D HEPATIC CELL CULTURES

3.1. Introduction

The majority of *in vitro* 3D cell culture relies on the use of hydrogels as extracellular matrix (ECM) mimics to promote the appropriate interactions between cells and their surrounding environment [87,90,102]. While the standard 2D system offers ease of set-up, hydrogels provide several distinct advantages over 2D and other 3D systems. Namely, hydrogels have flexible chemical and physical properties that allow for cell adhesion and growth, providing a stable structure for cells to mature in [78,117,118,120,173]. It is the goal of researchers to develop biomimetic, tunable hydrogels that can provide the necessary structural and chemical stability to promote cell growth and maturation in 3D.

Hydrogels have great diversity in structure and mechanisms for polymerization. Common hydrogels include those with polysaccharide structures (alginate [91,142], chitosan [137,138], hyaluronic acid [100,174]) and peptide/protein-based structures

(Matrigel [175,176], fibrin [96,103], collagen [94,96]), and both generalized structures may be biologically derived [93,177] or synthesized artificially [88,89,106,111]. Gelation mechanisms for hydrogels include changes in temperature [95], introducing certain ions into the polymer [178], UV-light based polymerization [179], enzyme-catalyzed polymerization [127], and changes to pH [180]. With the hundreds of methods and compositions used to form hydrogels, it is important to choose an optimum mimic for *in vivo* 3D-architectures.

As discussed in the previous chapter, PuraMatrix was not a suitable hydrogel for larger scale 3D cultures because the mechanisms for polymerization and its natural pH created some toxicity from the cells. Thus, we chose to explore photopolymerizable hydrogels. Photopolymerizable hydrogels have tunability in their physical properties and are more structurally stable than hydrogels that rely on ionic mechanisms of polymerization [179,181–184]. Photopolymerization relies on the use of a photoinitiator (PI) to generate radicals, which can serve as a crosslinker or use radical-based polymerization in the presence of hydrogels [183,185,186] Because of the covalent bonds formed during the polymerization process, photopolymerized hydrogels are more resistant to degradation than hydrogels that rely on ionic coordination or temperature activation for polymerization [179,182,186]. However, because of the presence of radicals in solution, there is inherent toxicity to the cell due to generation of reactive oxygen species (ROS), which can have a variety of effects from DNA damage and loss of protein function to peroxidation of the lipid membrane [187,188].

Oxy-methacrylated alginates (OMAs) provides many distinct advantages over native alginate. While alginate utilizes divalent cations to initiate ionic crosslinking with

57

carboxylic acids, OMA relies on the use of a PI with near-UV light to create covalent polymerization. This crosslinking has been demonstrated to be markedly more robust than alginate, both mechanically and its resistance to degradation [189]. While OMA has been used for a variety of studies, including *in vivo* implants and drug delivery, the use of OMA for microscale tissue culture and as a 3D scaffold on high-throughput platforms is lacking. While large scale cultures can potentially mimic more features of the various organs but suffer from inefficient nutrient transport and cost associated with the scale [190–193]. Miniaturizing these tissue cultures can improve some of these hurdles, yet further optimization of crosslinking is necessary, as the consumption of a PI and the penetration of light may be different at smaller scales [194,195]. Subsequently, there is a need to better understand what happens to cells and hydrogels in miniaturized 3D cell culture.

In this study, we attempted to optimize the parameters for polymerizing OMA within a microwell chip with a goal of finding a set of conditions yields stable and viable cells in 3D. The microwell chip contains 532 wells capable of holding ~ 1 µL spot volume, ideally designed for miniaturized 3D culture (Figure 7). While we have previously utilized the microwell chip as a vessel for containing media to be paired with the micropillar chip containing cells, we wanted to work with a platform that is more conducive to multi-layered 3D culture as spot volumes on the micropillar chip are quite small, and only allow for a thickness of two cells for 3D structures. We examined a variety of factors affecting polymerization, including surface background color, OMA concentration, intensity of light, duration of light exposure, and PI concentration. Additionally, we compared results between synthesized OMA samples that have different concentrations of methacrylate functional groups. We compared viability results and the formation of gels amongst all

conditions at various heights within the microwell, which ultimately allowed us to assess

the efficiency of polymerization of OMA in small volumes.
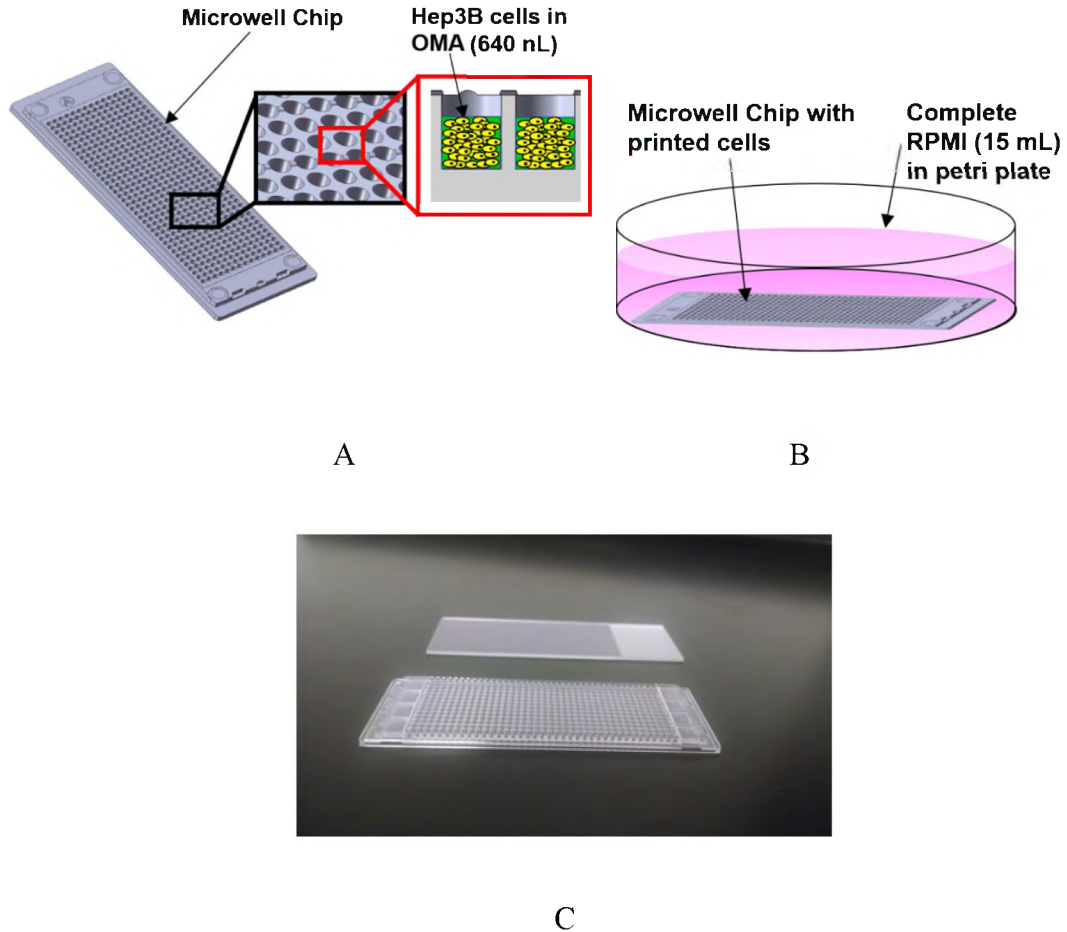
Figure 7. Schematic representation of (A) a microwell chip with printed Hep3B cells in a OMA matrix and (B) that same chip submerged in media in a petri plate. (C) Picture of a microwell chip against a microscope glass slide.

3.2. Materials and Methods

3.2.1. Materials

Hep3B human hepatoma cell line (catalog no. HB-8064) and all cell culture

ingredients, including RPMI, fetal bovine serum (FBS), penicillin-streptomycin (PS), and

gentamicin were provided from ATCC. The microwell chips were manufactured by MBD Korea (Suwon, South Korea). Staining solutions, including calcein AM and ethidium homodimer-1 were purchased from ThermoFisher. 2-Hydroxy-4'-(2-hydroxyethoxy)-2-methylpropiophenone (trade name, Irgacure2959, catalog no. 410896) for photopolymerization was obtained from Sigma Aldrich.

3.2.2. OMA Synthesis

OMA-15 and OMA-45 were prepared by the previously reported method with modification by Dr. Oju Jeon and Dr. Eben Alsberg from Case Western Reserve University [181,189]. Briefly, sodium alginate (10 g, Protanal LF 20/40, FMC Biopolymer) was dissolved in ultrapure deionized water (diH$_2$O, 900 ml) overnight. Sodium periodate (1 and 1.75 g, Sigma) was dissolved in 100 ml diH$_2$O, added into separate alginate solutions under stirring to achieve 10 and 17.5 % theoretical alginate oxidation, and allowed to react in the dark at room temperature for 24 hrs. The oxidized, methacrylated alginate (OMA) macromers were prepared by reacting OA with 2-aminoethyl methacrylate (AEMA). To synthesize OMA, 2-morpholinoethanesulfonic acid (MES, 9.76 g, Sigma) and NaCl (8.765 g) were directly added to an OA solution (500 L) and the pH was adjusted to 6.5. N-hydroxysuccinimide (NHS,0.44 and 1.325 g, Sigma) and 1-ethyl-3-(3-dimethylaminopropyl)-carbodiimide hydrochloride (EDC, 1.46 sand 4.375 g, Sigma) were added to the mixture under stirring to activate 15 and 45 % of the carboxylic acid groups of the alginate, respectively. After 5 min, AEMA (0.635 and 1.9 g, Polysciences) (molar ratio of NHS:EDC:AEMA = 1:2:1) was added to the solution, and the reaction was maintained in the dark at RT for 24 hrs. The reaction mixture was precipitated into excess of acetone, dried in a fume hood, and rehydrated to a 1 % w/v solution in diH$_2$O for further

60

purification. The OMA was purified by dialysis against diH_2O using a dialysis membrane (MWCO 3500, Spectrum Laboratories Inc.) for 3 days, treated with activated charcoal (5 g/L, 50-200 mesh, Fisher) for 30 min, filtered (0.22 μm filter) and lyophilized.

3.2.3. Plasma Treatment of Microwell Chips

Polystyrene microwell chips were exposed to plasma using a PDC-001-HP high power expanded plasma cleaner from Harrick Plasma. Up to ten microwell chips were laid out on the pyrex loading plate and placed inside the chamber. Initially, the chamber, 3-way valve, and metering valve were closed before the machine and vacuum were turned on for five minutes, lowering the chamber pressure to 100-200 mTorr. The three-way valve was opened to the processing position, and air was bled in at 250-350 mTorr for one minute. Following initial air processing, the plasma RF power was turned onto "medium" or "high" for one minute. Finally, RF power was maintained, and the metering valve was adjusted for air processing at 800-1000 mTorr for 5, 10, 15 and 20 minutes. After the final processing, samples were tested for successful treatment by immersing chips in 15 mL complete media in a petri plate following treatment. The microwells containing bubbles were evaluated as a function of the percentage of total microwells. We subsequently used the protocol that gave us the fewest average amount of bubbles. From this point forward, all samples were stored at room temperature for up to three days before cell printing occurred.

3.2.4. Preparation of OMA and PI

To create a 12 w/v % OMA solution, 120 mg of OMA-15 with 5% oxidation and OMA-45 with 17.5 % oxidation were separately dissolved in 1 mL complete RPMI

containing 10 v/v % fetal bovine serum (FBS), 1 v/v % penicillin and streptomycin (PS), and 0.1 v/v % gentamicin. Dissolving OMA consisted of vigorous manual mixing using a sterile spatula followed by vortexing and then centrifuging at 500 g for 5 minutes. This process was repeated up to twice until completely dissolved. If OMA was not adequately dissolved after three cycles of manual mixing, vortexing, and centrifugation, the sample was discarded, and dissolving started with a fresh sample. OMA is printed and polymerized one day after being dissolved in complete RPMI and is stored room temperature if printing occurs within one hour of dissolution, or at 4°C should it occur later. For polymerization and ease of mixing, 100 mg of Irgacure-2959 was dissolved in 1 mL of 70 v/v % ethanol via vortexing to a final concentration of 10 v/v %. Dissolved PI was stored at 4°C for up to a week before printing.

3.2.5. Printing Hep3B Cells in Microwell Chips

Hep3B cells (P15-P50) were cultured in RPMI + 10 % FBS + 1 % PS in T-75 flasks and grown to 90% confluence before passaging. Before printing, cells were resuspended to concentrations of 8 or 12 x 10^6 cells/mL in complete media. Cells, OMA, Irgacure2959, and complete media were mixed for the final printed solution, with concentrated cells representing half of the volume of the printed sample. The final concentrations Hep3B were 4 or 6 x 10^6 cells/mL. The final concentration of OMA was 1, 2, or 4 w/v %. The final concentration of Irgacure2959 was 0, 0.025, 0.05 or 0.10 w/v %. Cells were printed using a S+ Microarrayer from ATI Korea (South Korea) into a microwell plate at 640 nL/microwell.

3.2.6. Photopolymerization of OMA

Photopolymerization was initiated using an Omnicure Series 1500 UV curing system from Lumen Dynamics. The light source was fixed 20 cm above the exposed surface. The exposed surface was kept at 6°C during the duration of the polymerization to prevent sample evaporation. Up to two microwell chips were exposed to near UV light during a given exposure. For optimizing polymerization and viability of Hep3B cells in both OMA-15 and OMA-45, we varied the background color on which the chips rested (black cardboard paper versus reflective stainless steel), exposure time (30 seconds to 4 minutes), exposure intensity (45 versus 70% maximum intensity), PI concentration (up to 0.10 w/v %), and OMA concentration (1-4 w/v %) with a fixed cell seeding density (4 x 10^6 cells/mL).. For scenarios in which different regions on a microwell chip were exposed to different durations of light, the region experiencing shorter exposure was covered with black cardboard paper during the extended duration. Additionally, control samples were run in 96-well plates without plasma treatment. After polymerization at desired intensities, cells were placed in sterile petri plates and immersed in 15 mL pre-warmed complete RPMI.

3.2.7. Viability Analysis

Cells were assessed for viability using calcein AM and ethidium homodimer-1 to stain for live and dead cells. Microwell chips were initially washed twice in a saline solution containing 140 mM NaCl and 20 mM $CaCl_2$ for ten minutes per wash, and dried before and after washes by gently blotting with Kimwipes. Each chip was submerged in 8 mL of D-PBS containing 0.5 μM calcein AM and 0.5 μM ethidium homodimer-1 and incubated at room temperature in darkness for 2 hours. After washing, microwell chips were washed twice again with the saline solution for 20 minutes each in darkness and blotted dry using Kimwipes. After the final wash, micropillar chip surfaces were covered

with a Breath-Easy gas permeable sealing membrane for microtiter plates from Diversified Biotech, and subsequently scanned using a S+ Scanner from ATI Korea (South Korea). Microwell plates were scanned at a gain of 100 using a green filter. Samples that were not immediately scanned were placed in a moist incubation chamber and stored at 4°C until scanning could occur. All samples were scanned within 24 hours of the completion of staining. Fluorescence intensity was extracted for each layer using an in-house macro developed by Yu *et. al* [141]. Images were filtered of light that fell outside of green wavelengths. We then quantified the green fluorescence intensity across an entire image.

3.2.8. Statistical Analysis

Mean, standard deviation, and standard error were calculated in Microsoft Excel. One-way analysis of variance (ANOVA) was conducted in GraphPad Prism comparing the various factors impacting gelation. This analysis was conducted between different conditions across the same layer, focusing on the layers with highest cell densities.

3.3. Results

3.3.1. Surface Chemistry for Printing Cells in Microwell Chips

Surface chemistry was assessed by quantifying the percentage of microwells in a given chip that containing bubbles after treated chips were immersed in complete media. Bubble formation results are shown in Table 4. Ultimately, we found that for our microwell chips, bubble formation is minimized while processing plasma at high intensity at a pressure of 800-1000 mTorr for 15 minutes. Processing at medium intensity resulted in an increased amount of bubbles formed in the microwells, as did decreasing the duration of

the processing. Longer processing at the same intensity and pressure produced no noticeable effect on improving the hydrophilicity of the wells in the microwell chips.

Table 4. Bubbles Present in Plasma-Treated Microwell Chips (n=6)

Time	Area covered with bubbles (%)	
(Minutes)	Medium RF	High RF
5	69.4 ± 1.9	73.8 ± 5.3
10	46.6 ± 2.8	47.3 ± 8.1
15	32.5 ± 9.2	14.6 ± 1.4
20	35.5 ± 2.8	20.1 ± 1.5

3.3.2. Effect of Background on Polymerization

Our first attempts at improving OMA polymerization efficiency (and thus, the robustness of the 3D system) involved using black and reflective backgrounds while maintaining a surface temperature of 6°C. Our initial belief was that a reflective background could would provide more energy for more uniform polymerization, but we also wanted to test against using a normal lab bench-top color. As a result, background color did not impact 3D morphology of the hydrogel, but viability was impacted at 0.1 w/v % (Figure 8). We hypothesized that temperature within the microwells could be elevated locally due to black background. Since the cooling surface on which the chips sat is made of stainless steel, we used a reflective background to potentially increase the energy received to initiate photopolymerization. Since both black and reflective backgrounds resulted in no differences in the ability to form a gel, we decided to use a reflective background for simplicity of future experiments.
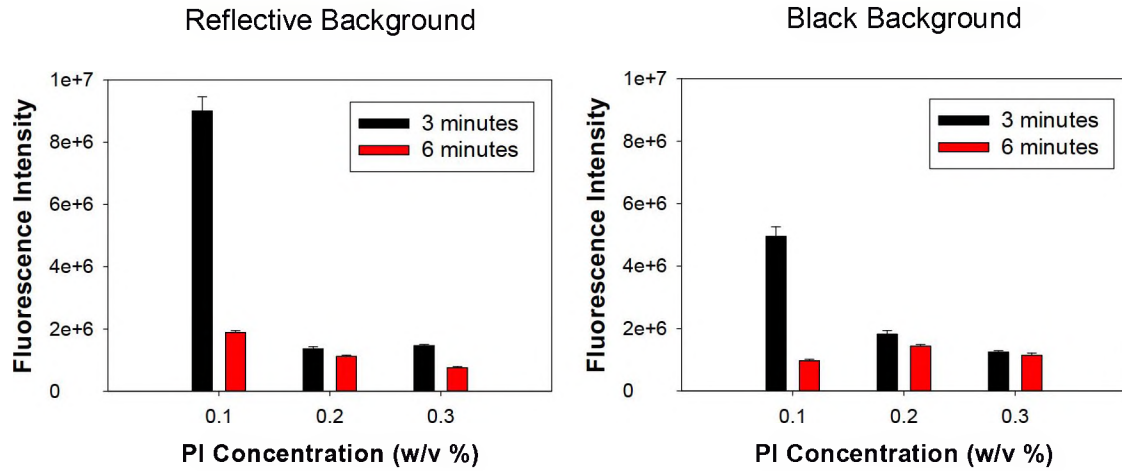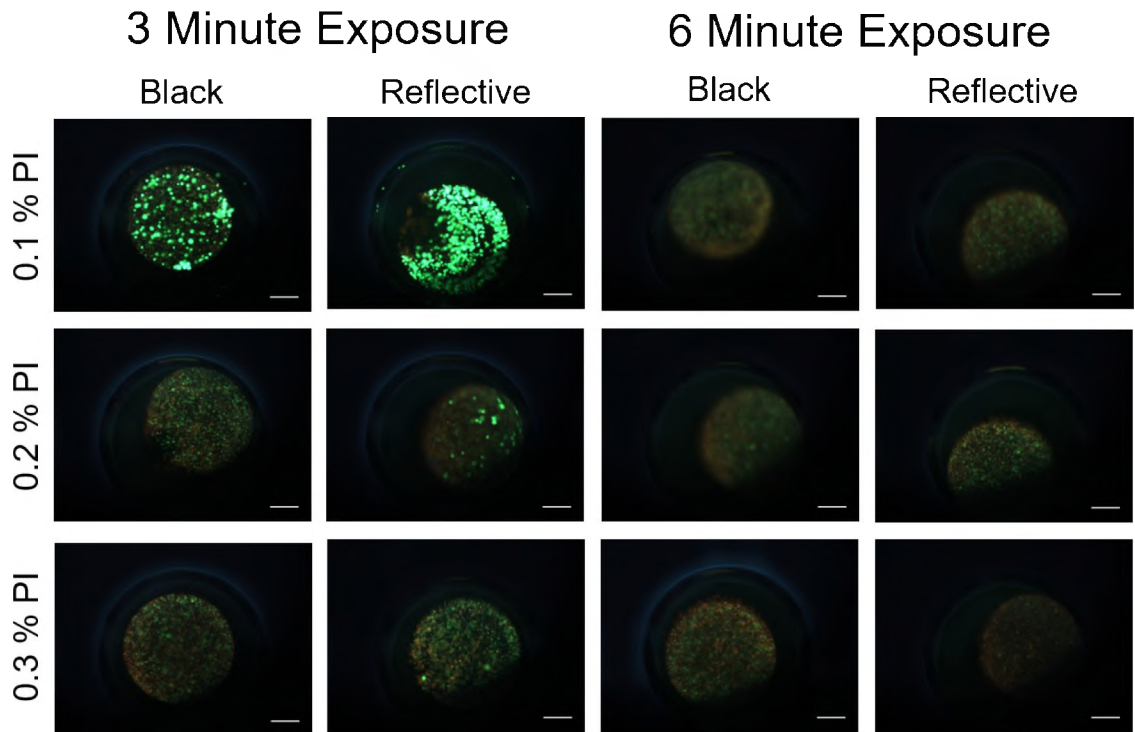
Figure 8. Demonstrated effect of using (A) reflective and (B) black background on the viability of Hep3B cells in 2 w/v % OMA-45. Samples were exposed to 0.1-0.3 w/v % PI using ~2.5 mW/cm² near UV-light for 3-6 minutes and measured at 300 μm above the bottom of the well. (C) Images corresponding with graphs at 300 μm above the bottom of the microwell (scale bar = 200 μm). Error bars represent SEMs, n = 72.

3.3.3. Effect of PI

When we examined PI concentration, the viability was optimized around using 0.05 w/v % Irgacure2959 (Figure 9). Decreasing the PI concentration resulted in decreased polymerization efficiency as cells could be observed in 2D. Meanwhile, increasing to 0.1 w/v % decreased cell viability, and subsequent increases would result in large cell death, resulting in a "goldilocks" scenario of using 0.05 w/v % Irgacure2959.

3.3.4. Effect of OMA Concentration

We found that Hep3B cell viability was optimized with 2 w/v % of OMA-45 (Figure 9). Increasing the hydrogel concentration to 4 w/v % caused numerous problems for the cells, including decreased viability and issues with printing due to increased viscosity of the materials. In addition, decreasing the concentration of OMA also affected the formation of 3D structures, yielding a "goldilocks" scenario of using 2 w/v % OMA-45. Furthermore, decreasing the PI concentration to 0.025 w/v % resulted in decreased polymerization efficiency while maintaining high cell viability.

3.3.5. Effect of Light Intensity and Duration

With the Irgacure system, we found several conditions that were ideal for polymerization of OMA-45 (Figure 10). Using a 45% intensity (~2.5 mW/cm^2) of the Omnicure Series 1500 UV curing system, we found polymerization to be achieved with a two-minute exposure. At a 70% intensity (~4.0 mW/cm^2), the exposure necessary to form gels dropped to 30 seconds. In these cases, subsequent increases of exposure time would often result in decreased viability, while decreases of exposure time would result in poor gelation, as is the case of with PI concentration. As a result, we decided to use a 70%

exposure intensity for 30 seconds as we believed this decreased the activation time for the PI while also minimizing the effect that changes in temperature could have on sample drying.

A

B
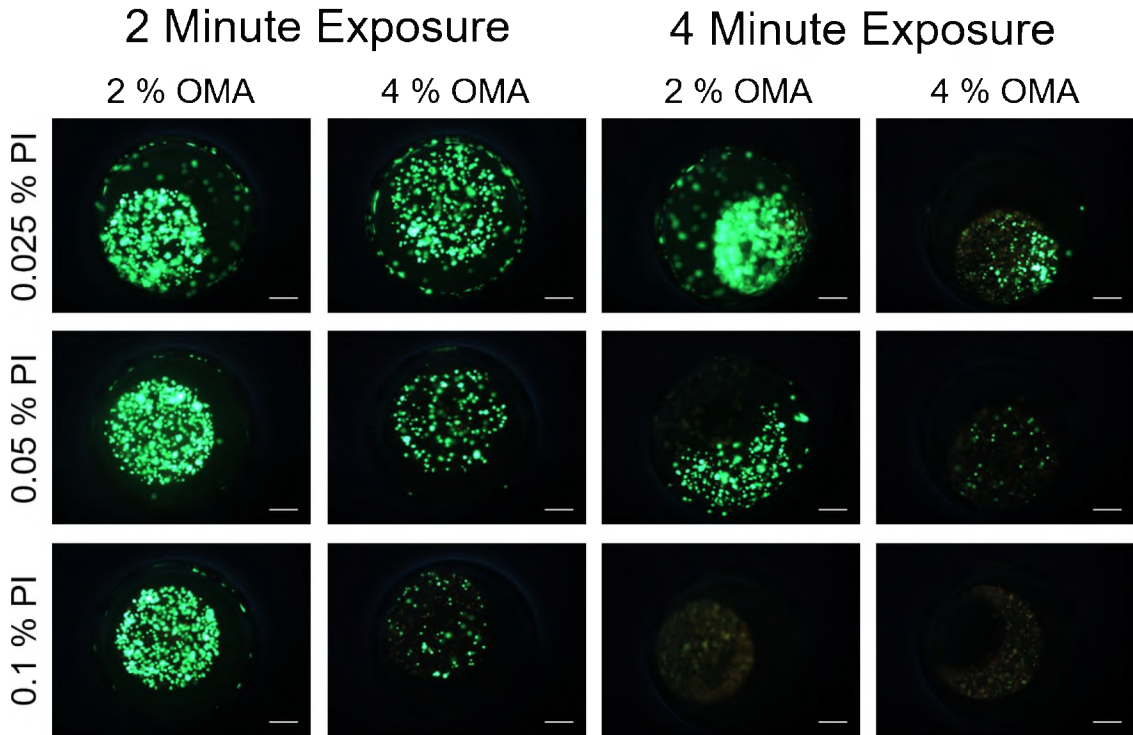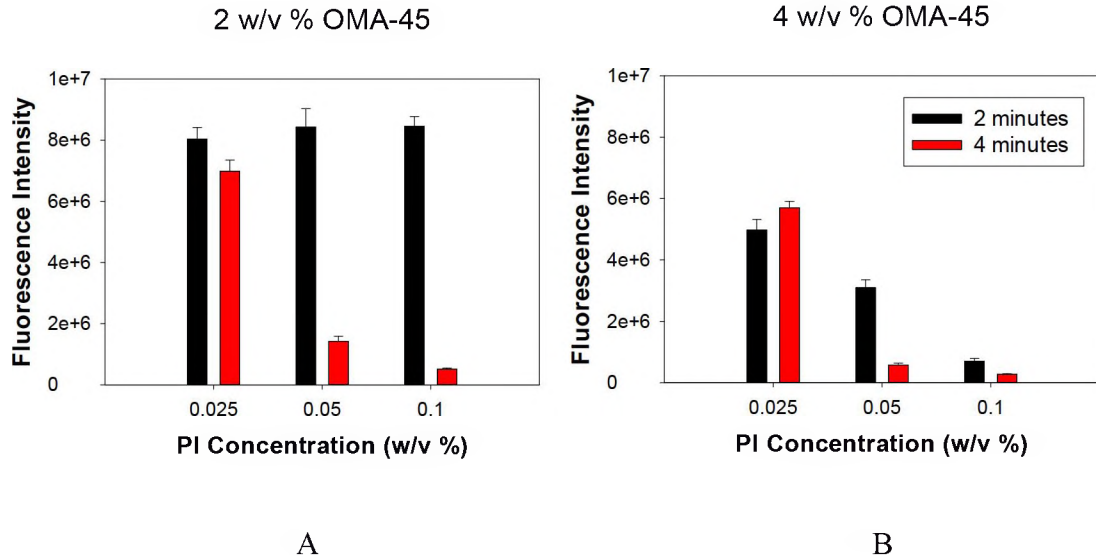
C

Figure 9. Demonstrated effect of varying concentration of OMA and PI using (A) 2 w/v % and (B) 4 w/v % OMA-45 on the viability of Hep3B cells. Samples were exposed to 0.025-0.1 w/v % PI using ~2.5 mW/cm² near UV-light for 2-4 minutes and measured at 300 μm above the bottom of the well. (C) Images corresponding with graphs at 300 μm above the bottom of the microwell (scale bar = 200 μm). Error bars represent SEMs, n = 72.

3.3.6. Optimization of OMA-15

Our attempts at optimizing photopolymerization while maintaining high Hep3B viability in OMA-15 in microwell chips proved to be unsuccessful (Figure 11). We found polymerization could not be achieved within the microwells for cells grown in OMA-15 in a way that would also allow for viable cells. Additionally, we attempted to see if increasing the exposure conditions while keeping microwell plates submerged in water to minimize temperature increase could aid in polymerization. However, we found that we were unable to achieve polymerization of OMA-15 within the microwell chips in this case too. We concluded that it is necessary to have methacrylation of 45% (use OMA-45) to achieve quick crosslinking at the microscale.

69

A   B

30 Second Exposure   ## 60 Second Exposure

2 % OMA   4 % OMA   2 % OMA   4 % OMA
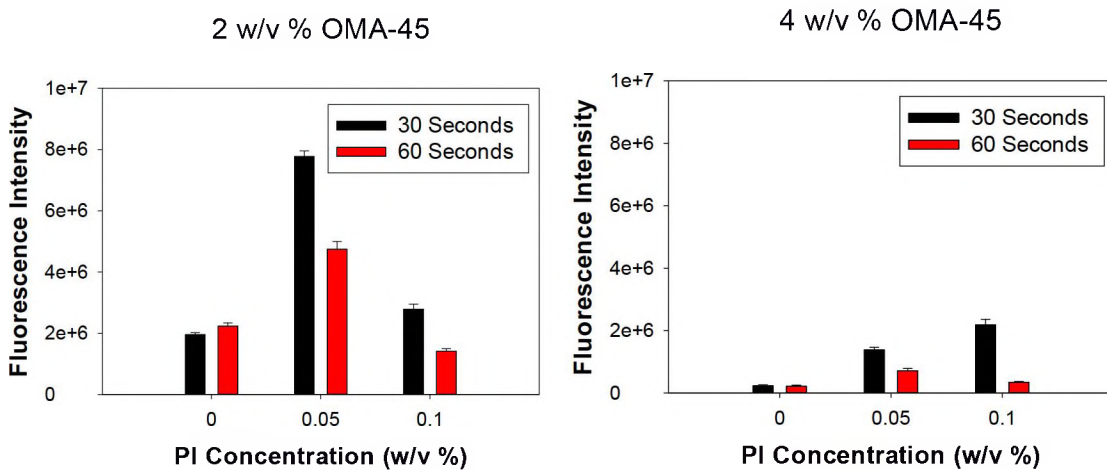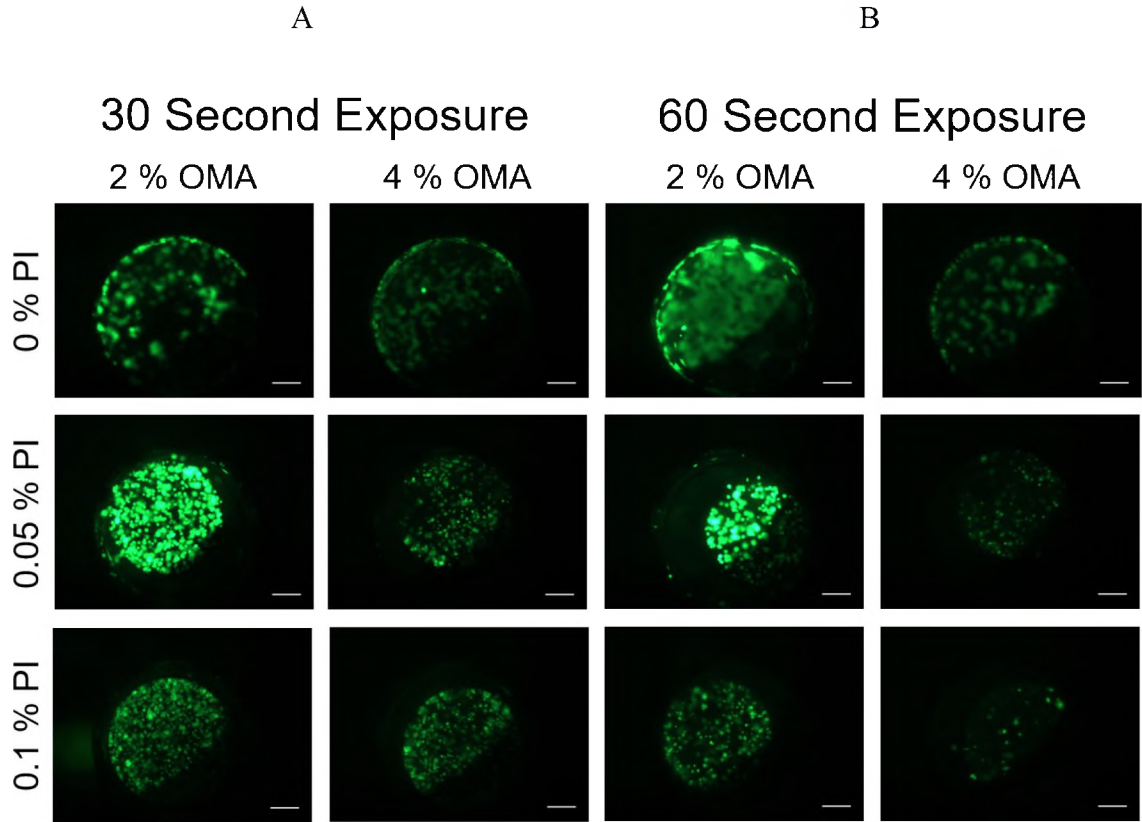
C

Figure 10. Demonstrated effect of using higher intensity, shorter exposures with (A) 2 w/v % and (B) 4 w/v % OMA-45 on the viability of Hep3B cells. Samples were exposed to 0.0-0.1 w/v % PI using 4.0 mW/cm² near UV-light for 30-60 seconds and measured at 300 μm above the bottom of the well. (C) Images corresponding with graphs at 300 μm above the bottom of the microwell (scale bar = 200 μm). Error bars represent SEMs, n =72.

2 w/v % OMA-15   4 w/v % OMA-15
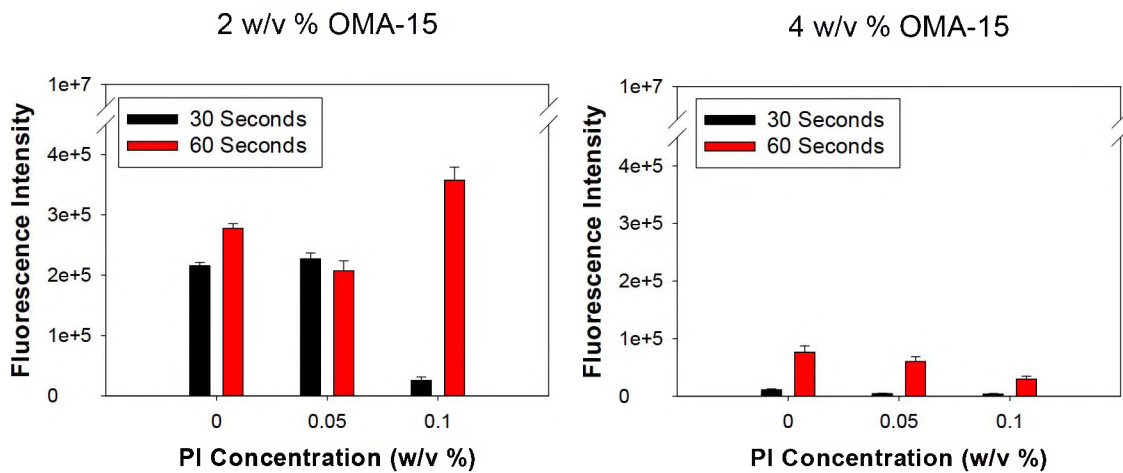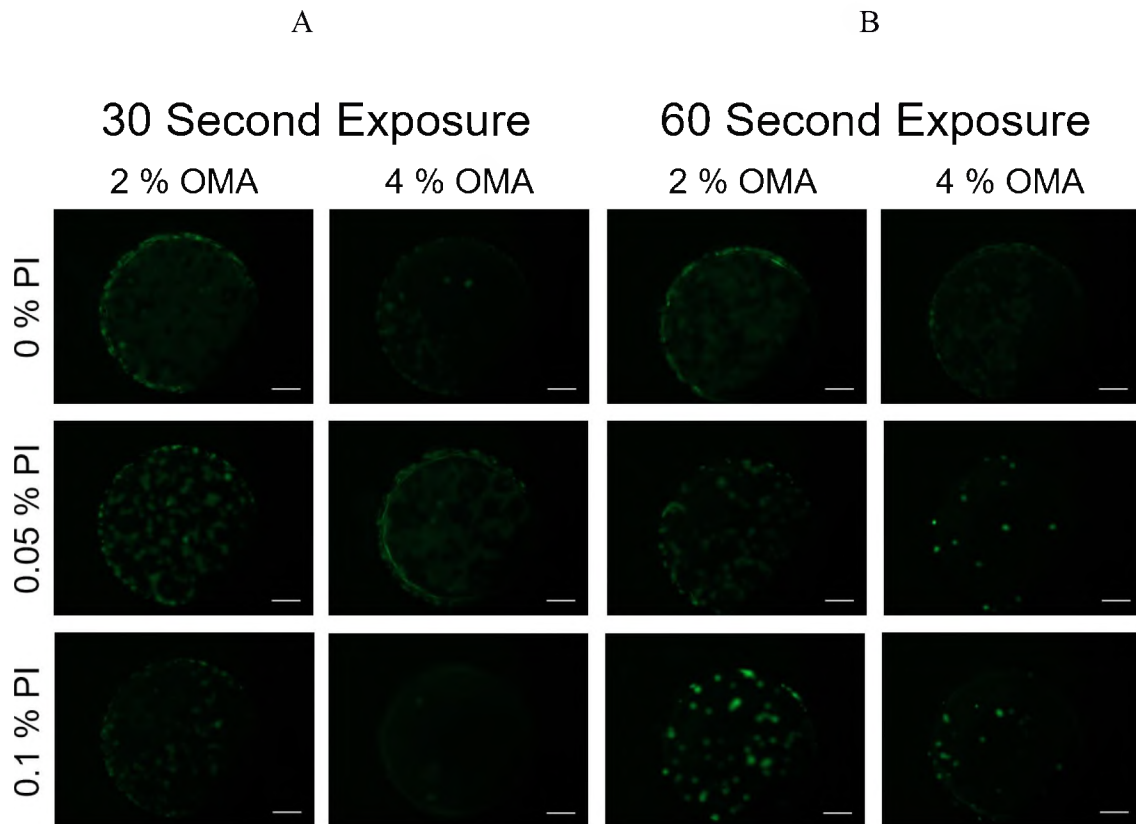
Figure 11. Comparative results using OMA-15 at (A) 2 w/v % and (B) 4 w/v % hydrogel concentration. Samples were exposed to ~ 4 mW/cm² intensity light for 30-60 seconds, using 0.0-0.1 w/v % PI. Analysis was done for samples at 300 μm above the bottom of the microwell. (C) Images corresponding with graphs at 300 μm above the bottom of the microwell (scale bar = 200 μm). Error bars represent SEMs, n = 72.

3.4. Discussion

The goal of this study was to develop a set of parameters that can polymerize OMA for miniaturized tissue cultures to produce viable cells in 3D. We found multiple factors that influence this process. While protocols for surface functionalization and etching using plasma utilize up to five minutes for treatment [196,197], we found it necessary to treat for fifteen minutes to minimize the formation of bubbles. Owing to the fact that microwell chips have depressions for containing media and cells, it was necessary to extend treatment

71

to ensure that media could adequately enter the wells when the chips were submerged. Extending treatment time past fifteen minutes did not decrease hydrophobicity of the chip, and changes in intensity of plasma exposure had a saturating effect when treating for longer durations. We believe that higher plasma energy was necessary to properly etch the surface of the chips, with saturation in the surface treatment having occurred at fifteen minutes. Increases or decreases in chamber pressure also tended to result in more bubbles in the microwells. We believe that having too little O_2 in the chamber means there is insufficient surface charge generated, while having too much O_2 resulted in decreased gas ionization, and thus decreasing the charge on the surface of the microwell chips. While bubbles do form within empty chips, bubble formation decreases significantly once 320 nL cell spots were printed into the wells. This indicates that we can completely eliminate air bubble entrapment by filling up the microwells (1.5 mm well depth and 1.15 mm well diameter) with cell spots with plasma treatment, which is critical for long-term cell culture in the microwell chip.

When examining polymerization of OMA, background color, PI concentration, OMA concentration, light exposure duration, light exposure intensity, and the relative presence of methacrylate functional groups all effected viability and the ability for Hep3B cells to grow in 3D. The results are listed at the top of Table 5 and compared with other photo-crosslinked hydrogels. We initially sought to compare black and reflective surfaces, along with examining PI concentrations of 0.1 to 0.3 w/v % Irgacure2959. Irgacure2959 was chosen owing to its relatively high solubility in water while requiring low concentrations to initiate photopolymerization as compared to other PIs [188]. While significant differences were not apparent between black background and reflective

background at higher PI concentrations, microwell chips placed on a reflective background had cells with greater viability at 0.1 w/v % PI. We suspect that this is due to the effect of temperature when the light is exposed, as the black color can absorb the light from the source and increase localized heat instead of dissipating it. Since our surface was naturally reflective and our cells were most viable at 0.1 w/v %, we used these as baselines for subsequent experiments.

Table 5. Optimized Parameters for OMA Polymerization

Cells Used	Hydrogel			PI		Light		Ref.
	Type	Functionalization (%)	Conc. (w/v %)	Type	Conc. (w/v %)	Intensity (mW/cm^2)	Duration (min)	
Hep3B	OMA	45	2	Irgacure 2959	0.05	2.5-4.0	0.5-2	N/A
hMSCs	OMA	15	2	Irgacure 2959	0.05	1	10	[198]
Chondrocytes	OMA	45	2	Irgacure 2959	0.05	1	10	[181]
hADMSCs	GelMA	80	6	Irgacure 2959	0.05	2	5	[199]
				VA086	0.75			
MDA MB 231s	GelMA	80	10	Irgacure 2959	0.05	1	10	[99]
VICs	GelMA	94	15	Irgacure 2959	0.5	7.2	0.25	[200]

Abbreviations: human mesenchymal stem cells (hMSCs); human adipose-derived MSCs (hADMSCs); methacrylated gelatin (GelMA); MD Anderson metastatic breast 231 (MDA MB 231) cancer cells; aortic valvular interstitial cells (VICs);

Results indicated that PI concentration significantly affected viability to the extent that subsequent experiments required using 0.1 w/v % PI as an upper limit to the concentration. We believe that the decrease in viability was due to the formation of the

radicalized PI *via* the UV light in such heavy quantities that subsequent generation of radicals caused oxidative damage to the cells. Using 0.1 w/v % PI was even shown to be toxic to cells as compared to 0.025 and 0.05 w/v % when accounting for fluctuations in light intensity and duration. We ultimately decided to use 0.05 w/v % PI, as this gave us consistent results in both cell viability and polymerization of OMA. We believe this is due to the "goldilocks" scenario achieved where at 0.05 % w/v, the concentration of PI is high enough where the radicals formed from the light can initiate sufficient polymerization of OMA, but not at such high concentrations that cause significant oxidative stress to the cells.

Regarding OMA concentration, our results clearly indicate that using higher concentrations of OMA (4 w/v %) resulted in decreased cell viability. This result indicates that high crosslinking with high concentrations of OMA (typically above 2 w/v %) is cytotoxic and may lead to diffusion limitations of nutrients and oxygen. We believe the high concentration of OMA impacted viability as the presence of too many cross-linking sites limited the ability of the Hep3B cells to thrive. Generally, divalent cation-polymerized alginate can be used at lower percentages than OMA because the cross-linking density is enough to support 3D cell growth while not so large as to restrict it or have a toxic effect on the cells [91,136]. Simply using 2 w/v % instead of 4 w/v % allowed us to maintain high cell viability without compromising the ability of OMA to be polymerized in the microwells. This result was consistent regardless of the exposure conditions used to initiate polymerization. An additional benefit of using 2 % w/v instead of 4 % w/v OMA is the decreased solution viscosity, which was generally easier to handle manually and is easier to print with our robotic dispensing system (S+ Microarrayer). Other groups also found

that use of lower concentrations of OMA were also favored for better cell viability [181,198].

The major variations between macro- and micro-scale photopolymerization are due to the effects of light exposure such as the duration and intensity of light. The penetration depth of light would be up to ten times different between macro- and micro-scale photopolymerization (1 cm vs. 1 mm). In the case of the exposure conditions, we were able to achieve successful photopolymerization of OMA while optimizing viability of Hep3B under at least two conditions. Both relatively short duration, higher intensity light and longer exposure, lower intensity light yielded optimal results while polymerizing 2 w/v % OMA with 0.05 w/v % PI. While the light is necessary for photopolymerization, activation of radicals and temperature increase both occur as a result of using this light source. Temperature is highly tied to both intensity and duration of light, as increasing either of these variables increased the ambient temperatures to above 38°C. In the case of PI, polymerization becomes active in the presence of near UV-light, so increases in intensity and duration resulted in increased concentration of radicals and subsequent oxidative stress to the cells. Our results were similarly reflected by Chen et al who initiated GelMA polymerization in a microfluidic device, and found that shorter duration, higher intensity exposure was better suited for forming 3D hydrogels at smaller scales [200].

In addition, the relative presence of methacrylate groups in OMA was also a major factor in polymerization efficiency in the microwell chip. Despite trying numerous combinations of factors affecting polymerization we were unable to achieve 3D culture in OMA-15 in the microwell chip. We believe the reason for this is that with fewer sites for crosslinking, the ability to form a gel within the microwell is limited. Increasing

75

concentration of OMA resulted in cell death, while decreased concentration still resulted in a lack of polymerization of OMA-15. All of this occurred independent of PI concentration and parameters affecting exposed light. Polymerization within the microwell chip is somewhat hampered compared to on glass slides or other smooth surfaces, as the intensity of light experienced at the bottom of the well is effectively 25-30 % less than that experienced at the top of the well. This necessitates increasing exposure intensity or duration to generate enough radicals for polymerization without impacting cell viability. While this may not limit the ability of OMA-15 to be used as a hydrogel for microscale tissue culture, it does mean that low methacrylate concentration within the OMA may not be polymerized effectively in small volumes with relatively low exposed surface areas. As a result, OMA-15 cannot be used for microscale tissue culture in such situations (i.e., within our microwell chips).

While microwell chips are an improvement compared to micropillar chips in terms of recapitulating 3D cell behavior, there are several drawbacks. One issue is that because microwell chips require submersion in petri plates to sustain sufficient nutrient growth, microwell chips cannot be used in combinatorial studies for testing drug efficacy or toxicity. Additionally, media can only enter through the top of the well, so there is the potential for nutrient diffusion limitation issues to cells located near the bottom of the well.

3.5. Conclusions

We were able to successfully create viable 3D-cultured Hep3B cell structures within microwell chips using a photopolymerizable hydrogel, OMA-45. While the material

parameters of 0.05 w/v % Irgacure2959 and 2 w/v % OMA-45 concentration and methacrylate concentration work to produce viable cells encapsulated in strong hydrogels, polymerization is best achieved using 4.0 mW/cm^2 intensity light for 30 seconds or 2.5 mW/cm^2 light for two minutes. There is a significant contribution to the ability to form viable 3D spheroids from the size of the reaction and the apparatus, as OMA-15 could not be polymerized in microwell chips. Additionally, larger scale polymerizations generally require lower intensity and significantly longer durations of exposure, while microscale polymerizations benefit from higher intensity and quicker reactions. Ultimately, these results are promising for generating miniaturized tissue constructs within the microwell chips. In the future, we hope to use OMA-45 as a hydrogel scaffold for full recapitulation of the *in vivo* liver functions and to create a model for observing specific liver disease states *in vitro*.

3.6. Acknowledgements

CHAPTER IV

A HIGH-THROUGHPUT 3D HEPATIC CANCER CELL MIGRATION ASSAY

ON A 384-PILLAR PLATE WITH SIDEWALLS

4.1. Introduction

Hepatocellular carcinoma (HCC) is the most widely distributed liver cancer in the world, constituting about sixty five percent of liver cancer patients, and it is the sixth most prevalent of all cancers globally [4]. HCC, unlike other cancers in the United States, is seeing an increase of incidence, with estimates placing the number of affected individuals having tripled since the 1980s [1,5]. These triggers are likely due to the fact that poor sanitation conditions have seen an increase in individuals infected with hepatitis, where the hepatitis B and hepatitis C viruses (HBV and HCV respectively) are known to lead to HCC [1]. HCC is characterized by generally being treatable if detected early but having poor prognosis during later staging of the disease if metastasis has occurred [31,36]. Thus, it is the goal of scientists and doctors to understand what causes metastasis of HCC, how to prevent the spread of the disease, and how to better treat a patient who is experiencing metastasis.

Cancer metastasis can be triggered by external cues, signaling cells to migrate away from the initial tumor site towards otherwise unaffected parts of a previously affected organ or to different organs entirely [59]. The nature of these cues is diverse, ranging from changes in confirmation of the extracellular matrix (ECM) in the tumor, to small and large molecule signaling from lack of nutrients [59,201]. The tumor ECM plays a large role in the metastasis of a cancer, as tumors are generally poorly vascularized, and have a much more heterogeneous cell distribution than a healthy tissue [6,202]. Once angiogenesis within the tumor occurs, the cells from the HCC have a means from which to migration out [6,203]. Often, these markers for angiogenesis are triggers for metastasis in themselves [204–206].

Because of the variety of biomarkers and triggers for cancer metastasis, scientists desire methods to mete out any false positives for cancer detection and determine how these various factors interact with each other. Growth factors (GFs) such as basic fibroblast growth factor (bFGF) and transforming growth factor beta 1 (TGFβ1) play important roles in cellular reorganization, but also in angiogenesis as signal molecules for cancer cell metastasis [60,207–209]. Due to the variant nature of cancer, it is important for scientists and doctors to know the distinct molecules that can signal for metastasis based on the type of cancer and the individual case.

Often, scientists will use cell migration studies as an *in vitro* assessment of potential metastatic cues. General migration tests have focused on two-dimensional (2D) assessments, such as wound healing assays, to signal and promote cell movement [47,210]. However, 2D migration systems lack the directionality of movement associated with true metastatic behavior observed *in vivo* [47,56]. Additionally, media supplementation to these

systems cannot mimic the nutrient transport observed in a three-dimensional (3D) *in vivo* environment [205,211]. 3D cell migration has focused on developing cell spheroids and quantifying the dispersal of cells away from spheroids or tracking individual cell movement through ECM mimics [47,56,212]. The main draw back with using 3D systems is that it is trickier to determine modes of migration, particularly in high-throughput when numerous factors need to be considered for understanding the nature of a tumor [47,68,212].

Our group has previously developed several small-scale high-throughput platforms, mostly used in the development of drug toxicity testing. Originally, we worked with the micropillar chip for cell culture and paired with a microwell chip containing media and various dissolved compounds [142,143,213,214]. Because of the size limitations associated with micropillar chip cultures, adequate 3D cell cultures could not be generated. We subsequently used microwell chips as the platform for cell seeding while immersing the chips in media in petri plates. While this allowed a better recapitulation for certain cell culture aspects, the microwell chip is not ideal for combinatorial work as media composition cannot vary between wells on the same chip due to the need to immerse whole chips in individual petri plates to supply sufficient nutrients to cells. Additionally, cells located within a microwell chip beneath several other layers of cells could suffer from lack of nutrients. The current system developed by Bigdelou et. al. utilizes pillar plates designed with sidewalls fitted to a 384-well plate (Unpublished). Here, cells encapsulated in hydrogels would grow on the pillars while being supported by the sidewalls beneath the pillars. The sidewalls can help anchor cell droplets, while the spaces between the walls allow for nutrients from growth media to come into contact with cells on the pillar. The sidewalls can hold about 4 μL of hydrogel droplet volume, which is sufficient for several

layers of printed cells. Because the platform is designed to be paired with a 384-well plate, combinatorial studies can be conducted using varied growth media, making it ideal for understanding the multitude of factors affecting cancer cell migration.

The goal of this work is to develop a high-throughput 3D cancer cell migration test. In order to do this, we will let cells migrate in response to the presence of various growth factors and extracellular matrix (ECM) components within the 384-pillar plate with sidewalls (Figure 12). We used oxidized methacrylated alginate (OMA-45) for cell encapsulation. The use of OMA-45 for microscale polymerization has been optimized as detailed in Chapter III, while the design of the 384-pillar plate with sidewalls was optimized by Bigdelou et. al. (unpublished). The design of the test is similar to a typical sandwich assay. On the first-printed layer, we print OMA with various growth factors which will be stabilized with the presence of methacyrlated heparin sulfate (MHS). On the second layer, we will print cell-laden OMA. The Hep3B cells used in the top layer will have been infected with lentiviruses containing mCherry expression so that we can monitor in real time if cells are migrating in response to the materials in the bottom layer. Cells will be monitored for up to two weeks to determine if migration occurs in response to the presence of certain chemoattractants by taking pictures of the cells at various heights within the pillars. Finally, this migration will be quantified using developed in house macros which will filter out any background associated with out-of-focus cells. This will ultimately give us a method in which we can quantify 3D cell migration in high-throughput.

A

B

384-pillar plate with sidewalls

Growth factors in OMA and Heparin (2 µL) Hep3B cells in OMA (2 µL) Media in 384-well plate

Cells migrating in response to growth factors

C
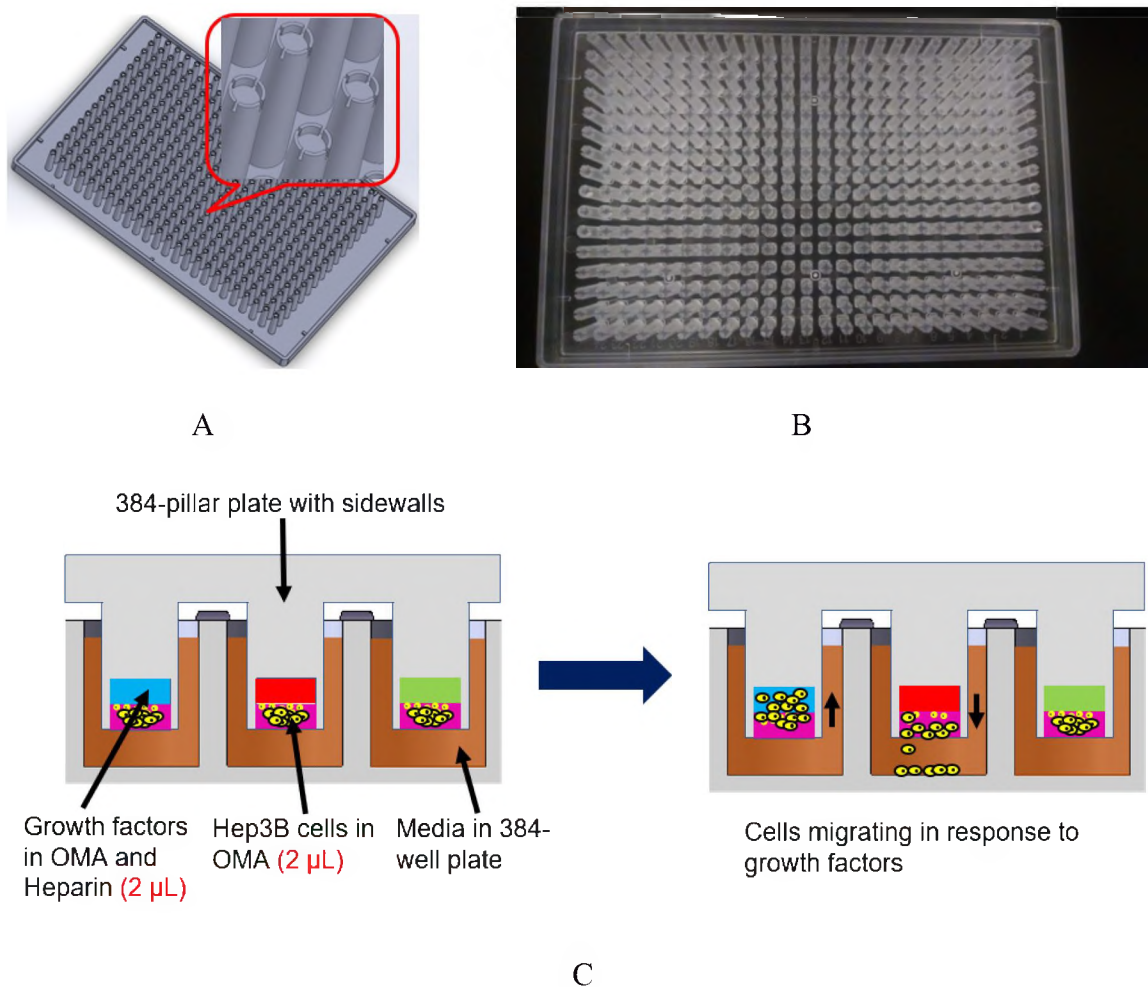
Figure 12. (A) Schematic representation of 384-pillar plates with sidewalls. (B) A photograph of a 384-pillar plate with sidewalls. (C) Schematic representing migration assay in 384-pillar plate with side walls. Initially, growth factors are bound to heparin sulfate and encapsulated with OMA. Then, cells are encapsulated in OMA and printed on a second layer. This is inverted and stamped into a 384-well plate, where cells migrate in response to growth factors.

4.2. Materials and Methods

4.2.1. Materials

Hep3B human hepatoma cell line (catalog no. HB-8064), HEK293T cells (catalog no. CRL-11268) and all cell culture ingredients, including RPMI, DMEM, fetal bovine serum (FBS), penicillin-streptomycin (PS), and gentamicin were provided from ATCC.

The microwell chips were manufactured by MBD Korea (Suwon, South Korea). Staining solutions, including calcein AM and ethidium homodimer-1, Opti-MEM reduced serum media (31985062), and lipofectamine 2000 (11668027) transfection reagent were purchased from ThermoFisher. 2-Hydroxy-4'-(2-hydroxyethoxy)-2-methylpropiophenone (trade name, Irgacure-2959, 410896) for photopolymerization, polybrene infection/transfection reagent (TR-1003-G), and heparin sodium salt from porcine intestinal mucosa (H3393) was obtained from Sigma Aldrich. The growth factors basic fibroblast growth factor (bFGF, cyt-218), hepatocyte growth factor (HGF, cyt-244), transforming growth factor beat (TGF-β, cyt-716), and vascular endothelial growth factor (VEGF, cyt-241) were all sourced from ProspecBio. The VEGF ELISA kit (DY293B-05) and the ancillary reagent kit (DY008) were sourced from DuoSet. E-Shell 450 Clear M (RES-02-422) from EnvisionTEC was used to create the initial mold for the printed 60-pillar plate with side walls described in Bigdelou et al (Unpublished) before the optimized 384-pillar plate with sidewalls manufactured *via* plastic injection molding at TechOne.

4.2.2. Synthesis of OMA

OMA-45 was prepared by the previously reported method with modification by Dr. Jeon and Dr. Alsbserg of Case Western Reserve University [181,189]. Briefly, sodium alginate (10 g, Protanal LF 20/40, FMC Biopolymer) was dissolved in ultrapure deionized water (diH$_2$O, 900 ml) overnight. Sodium periodate (1 and 1.75 g, Sigma) was dissolved in 100 ml diH$_2$O, added into separate alginate solutions under stirring to achieve 10 and 17.5 % theoretical alginate oxidation, and allowed to react in the dark at room temperature for 24 hrs. The oxidized, methacrylated alginate (OMA) macromers were prepared by reacting OA with 2-aminoethyl methacrylate (AEMA). To synthesize OMA, 2-

morpholinoethanesulfonic acid (MES, 9.76 g, Sigma) and NaCl (8.765 g) were directly added to an OA solution (500 L) and the pH was adjusted to 6.5. N-hydroxysuccinimide (NHS, 0.44 and 1.325 g, Sigma) and 1-ethyl-3-(3-dimethylaminopropyl)-carbodiimide hydrochloride (EDC, 1.46 sand 4.375 g, Sigma) were added to the mixture under stirring to activate 45 % of the carboxylic acid groups of the alginate. After 5 min, AEMA (0.635 and 1.9 g, Polysciences) (molar ratio of NHS:EDC:AEMA = 1:2:1) was added to the solution, and the reaction was maintained in the dark at RT for 24 hrs. The reaction mixture was precipitated into excess of acetone, dried in a fume hood, and rehydrated to a 1 % w/v solution in diH_2O for further purification. The OMA was purified by dialysis against diH_2O using a dialysis membrane (MWCO 3500, Spectrum Laboratories Inc.) for 3 days, treated with activated charcoal (5 g/L, 50-200 mesh, Fisher) for 30 min, filtered (0.22 µm filter) and lyophilized.

4.2.3. Cell Migration in Microwell Chips

We initially tested migration using microwell chips, with a Matrigel-OMA bottom layer and a top layer of OMA. Microwell chips were exposed to plasma using a PDC-001-HP high power expanded plasma cleaner from Harrick Plasma. Samples were processed for 15 minutes at high intensity. 120 mg OMA-45 was dissolved in 2 mL complete RPMI to a concentration of 6 w/v %. 100 mg PI was dissolved in 1 mL 70 v/v % ethanol to a concentration of 10 w/v %. 80 µL OMA was added to 1.2 µL PI with variable amounts of 9.1 mg/mL Matrigel and complete media to a final volume of 240 µL. The final concentration of the bottom layer of solution consisted of 2 w/v % OMA-45, 0.05 % w/v PI, and 0, 1, 2, 3, or 4 mg/mL Matrigel, all diluted in complete RPMI. Additionally, a control was run that contained 0 mg/mL Matrigel and 0 % w/v PI. The bottom layer was

printed with an S+ Microarrayer at 320 nL/microwell and gelled using the Omnicure 1500S system at 4 mW/cm^2 for 30 seconds. We then combined 600 μL OMA-45, 9 μL PI, 900 μL 8 x 10^6 cells/mL, and 291 μL complete RPMI to form the top layer, which consisted of 2 w/v % OMA-45, 0.05 w/v % PI, and 4 X 10^6 cells/well. The top cell layer was printed on top of the Matrigel bottom layer at 320 nL/well, and gelled using the Omnicure 1500S system at 4 mW/cm^2 for 30 seconds. Cells were submerged in 15 mL media in petri plates, where media was changed as needed. Microwell chips were removed 0, 3, 7, and 14 days after initial print for cell staining.

4.2.4. Cell Staining

Cells were assessed for viability using calcein AM and ethidium homodimer-1 to stain for live and dead cells. Microwell chips were initially washed twice in a saline solution containing 140 mM NaCl and 20 mM CaCl$_2$ for ten minutes per wash, and dried before and after washes by gently blotting with Kimwipes. Each chip was submerged in 8 mL of D-PBS containing 0.5 μM calcein AM and 0.5 μM ethidium homodimer-1 and incubated at room temperature in darkness for 2 hours. After washing, microwell chips were washed twice again with the saline solution for 20 minutes each in darkness and blotted dry using Kimwipes. After the final wash, micropillar chip surfaces were covered with a Breath-Easy gas permeable sealing membrane for microtiter plates from Diversified Biotech, and subsequently scanned using a S+ Scanner from ATI Korea (South Korea). Microwell plates were scanned at a gain of 100 using a green filter. Samples that were not immediately scanned were placed in a moist incubation chamber and stored at 4°C until scanning could occur. All samples were scanned within 24 hours of the completion of staining. Fluorescence intensity was extracted for each layer using an in-house macro

developed by Yu *et. al* [141]. Images were filtered of light that fell outside of green wavelengths. We then quantified the green fluorescence intensity across an entire image.

4.2.5. Surface Treatment of 384-Pillar Plates with Sidewalls

384-pillar plates were sandwiched with 384-well plates containing 30 µL/well 0.05 % w/v PMA-OD and left to dry under ambient air at room temperature for 2-3 hours. The pillar plates with sidewalls were then sandwiched with 384-well plates containing 30 µL/well 0.0033 w/v % PLL solution and left to air dry over night before printing.

4.2.6. Growth Factor Leaching

Initially, 120 mg of OMA-45 was dissolved in 2 mL complete RPMI (RPMI + 10 % v/v FBS, 1 % v/v PS, and 0.1 % v/v gentamicin) using a metal spatula, then vortexed and centrifuged at 500 g for 5 minutes. If precipitate was present, this process was repeated until the precipitate was gone. For heparin-dependent leaching, we added 12 mg of heparin to the 120 mg OMA-45 before adding the media. This yielded a 6 % w/v OMA-45 and 0.6 % w/v heparin solution. We diluted 10 µL of the VEGF in 500 mM NaCl to form a 40 µg/mL solution of VEGF. We then combined 133.3 µL of our OMA with 2 µL of 10 % w/v PI in 70 % ethanol and 214.7 µL complete RPMI as our stock solution. 35 µL of the stock solution was combined in separate tubes with 0-5 µL of the 20 µg/mL VEGF solution and finished off with 0-5 µL media. This yielded a 2 % w/v OMA-45 hydrogel (with possible 0.2 % w/v heparin), and 0.5 µg/mL bound VEGF and 0.05 % w/v PI in a total volume of 40 µL. Samples were manually pipetted into the depression of the 384-pillar plate with sidewalls at 2 µL/pillar. Samples were then exposed to UV-light from using an Omnicure Series 1500 UV curing system from Lumen Dynamics. Exposure occurred at 20 cm beneath the light source at 12 cm above the plate for 60 seconds. For the top layer, we

combined 133.3 µL 6 % w/v OMA-45, 2 µL 10 % w/v PI in 70 % ethanol, and 264.7 µL complete RPMI to form a final solution of 2 % w/v OMA-45 and 0.05 % w/v PI in a total volume of 400 µL. 2 µL were added to the same wells our VEGF-containing samples were mixed in and re-exposed to the UV light at the previously described conditions. The top layer was printed at 2 µL/pillar on top of the growth factor layer in the 60-pillar plate with sidewalls using a S+ Microarrayer. Samples were re-exposed to light at the previous described conditions. Samples were then immersed in 50 µL complete RPMI in a 384-well plate. All the media in the wells was taken out and replaced with fresh media at 1, 4, 8, and 24 hours, followed by media replacement every other day starting at day 2 until day 14. Samples were frozen until analysis of leaching was performed.

4.2.7. Quantifying the Leach Concentration

Leached VEGF was quantified using a VEGF ELISA kit from DuoSet. Capture antibody was coated overnight at room temperature in a 96 well plate. Wells were washed three times with tween-20, then exposed to 300 µL/well BSA blocking solution for one hour. Wells were washed again three times before exposure to samples and standards (15.6-1000 pg/mL). Samples were incubated for another two hours and washed three times again. Samples were exposed to the capture antibody at room temperature for two hours. Samples were washed again then exposed to strep-HRP for 20 minutes. Wells were washed three times again and exposed to two color reagents. The reaction was stopped after 20 minutes, and absorbance measurements were taken at 450, 540, and 570 nm immediately.

4.2.8. Design and Expansion of Lentivirus Vector

The lentivirus was designed and expanded using the protocols of Joshi et al. (Unpublished). HEK293T cells (passage < 10) were expanded to 50 % confluence in

DMEM + 10 v/v % FBS + 1 v/v % PS in a T-25 flask. In one tube, 200 μL Opti-MEM reduced serum media was mixed with 16 μl lipofectamine 2000 reagent. In a second tube, 266 μL opti-MEM reduced serum media was mixed with 30 μL pLV-mCherry vector (40 ng/μL), 1 μL pMDG2 (800 ng/μL), and 2 μL pSOX2 (800 ng/μL). The contents of the two vials were mixed to a total volume of 525 μL with 2.28 ng/μL pLV-mCherry, 1.52 ng/μL pMDG2, and 3.05 ng/μL pSOX2. Media was removed from the flask and cells were washed before this solution was added with 2 mL DMEM + 10 v/v % FBS and 2.5 μL 10 mg/mL polybrene to assist in transfection and incubated for one day at 37 ^{0}C and 5 % CO_2, after which transfection was observed at > 90%. Subsequently, supernatant was collected and 2.5 mL fresh DMEM + 10 v/v % FBS + 1 v/v % PS was added, and cells were continually incubated for another three days. The supernatant was collected again and pooled with the supernatant collected at day 1 and stored at -80 °C until further use. Samples were concentrated using centrifugal filtration and titered using FACS.

4.2.9. Transduction of Lentiviruses into Hep3B Cells

$1*10^6$ Hep3B cells (P15-30) were plated on a T-25 flask and grown in 5 mL RPMI + 10 % FBS + 1 % PS for 48 hours, or until 50-60 % confluence was reached. Media was removed and replaced with 2 mL antibiotic-free RPMI + 10 % FBS, 40 μL lentivirus stock solution, and 2.5 μL 10 mg/mL polybrene for a multiplicity of infection (MOI) of 1. Cells were grown in the flask for 24 hours before addition of 5 mL RPMI + 10 % FBS. These cells were grown for another 24 hours before passaging and expansion. Cells were frozen at -80°C for future experiments.

4.2.10. Cell Migration with Encapsulated Growth Factors

For cell migration, we followed a similar protocol to our leach experiment. OMA and heparin were dissolved in complete RPMI at 6 and 0.6 % w/v respectively using a combination of manual stirring and vortexing, then centrifuging at 500 g for 5 minutes to remove bubbles. Next, samples were combined with 10 % w/v PI in 70 % ethanol, individual growth factor solutions (stock concentration: 200 μg/mL), and complete RPMI. All growth factors (TGFβ1, VEGF, bFGF, and HGF) were printed at a final concentration of 1 μg/mL, with OMA and heparin at 2 and 0.2 % w/v respectively, and PI at 0.05 % w/v. Samples were incubated for three hours at room temperature before being dispensed on the 384-pillar plate with side walls at 2 μL/pillar using a S+ Microarrayer. Samples were then polymerized via exposure to near UV-light at 70% intensity 12 cm above the plate for 60 seconds. The top layer was then prepared, combining 120 μL of $8 * 10^6$ infected Hep3B cells/mL, 80 μL 6.0 % w/v OMA-45 in complete RPMI, 1.2 μL 10 % w/v PI in 70 % ethanol, and 38.8 μL RPMI. This gave us a final concentration of $4 * 10^6$ infected Hep3B cells/mL in 2.0 % w/v OMA-45 and 0.05 % w/v PI. This top layer was printed at 2 μL/well using a S+ Microarrayer. After the top layer was printed, cells were allowed to settle for five minutes before being polymerized by near UV-light. Cells were imaged at seven different positions spaced 250 μm apart, starting from the top edges to the side wall until hitting the pillar surface daily for two weeks after seeding. Images were taken using a S+ Scanner with an orange filter (SEMCO, TxRed-4040C-000) using 100 and 400 gain at on day zero with decreasing the high gain until day 14 was reached, when 25 gain was used.

4.2.11. Quantification of Cell Migration

We developed a macro through which we eliminated out-of-focus cells first. The macro developed in ImageJ would have images undergo a finite Fourier transform (FFT), with bandpass filtering at 50 and 250 Hz before undergoing inverse FFT (iFFT). Finally, the macro would sorted into folders containing common z-positions based on labels within the file names. Next, fluorescence was quantified using an in-house developed bioprinting macro for ImageJ that quantifies the range of fluorescence between 0 and 50 to only quantify the red signal. After the signal was quantified, we calculated the mean position of the cells using the following equation:

$$\overline{Z} = \frac{\sum_{i=1}^{n} f_i z_i}{\sum_{i=1}^{n} f_i}$$

Where $\overline{Z}$ is the mean position of the cells, f_i and z_i are the corresponding fluorescence intensity and z-position height in row i. We then calculated a rate of cell movement by comparing mean z-positions in identical wells across various time points.

4.2.12. Statistical Analysis

Mean, standard deviation, and standard error were calculated in Microsoft Excel. One-way analysis of variance (ANOVA) was conducted in GraphPad Prism comparing the individual and combinations of growth factors in the gel and in solution. Graphs for ELISA standards, fluorescence intensity, leaching, and migration were generated in SigmaPlot.

4.3. Results

4.3.1. Migration in Microwell Chips

The quantification of migration showing mean position in the wells of the microwell chips is shown in Figure 13. We were able to successfully distinguish cells between layers using our macro and observed some cell movement. However, much of this movement was limited, and none of our results showed chemoattraction towards Matrigel. Additionally, because our procedure required staining of the cells, samples had to be disposed after imaging and could not be used for subsequent monitoring of migration, which forced us to use Hep3B cells infected with lentiviruses to track migration.

4.3.2. Lentivirus Transduction

The results of lentiviral transductions are shown in Figure 14. We were able to successfully transduce lentiviruses into cells. Efficiency of transfection was estimated around 80 percent. Furthermore, infected Hep3B cells were successfully frozen and thawed after infection with the virus. There was no significant impact with viability on the cells, and cells retained expression of mCherry up to ten passages after the frozen cell line was thawed. Thus, we were able to create a stable Hep3B cell culture capable of expressing mCherry for the purposes of tracking migration.
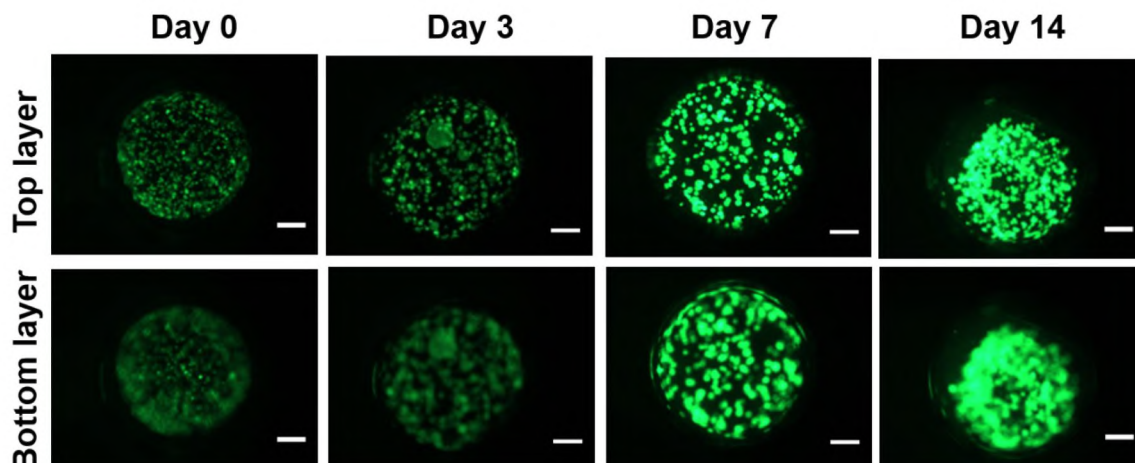
A
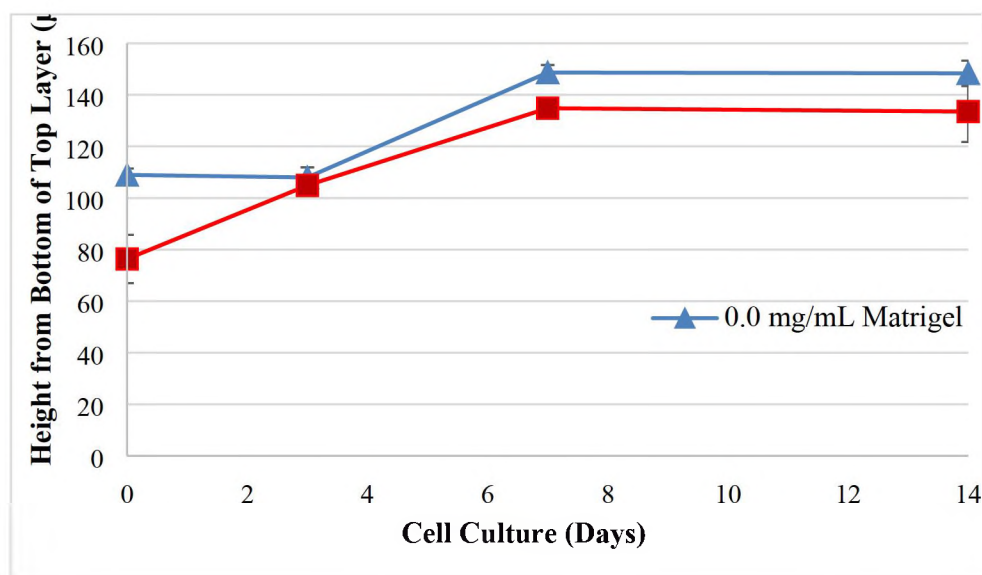
B

Figure 13. A) Calcein-AM stained Hep3B cells encapsulated in 2 w/v % OMA-45 and printed into a microwell chip on the top layer, with the bottom layer for this set of images containing 1.5 mg/mL Matrigel. Scale bar = 200 μm. B) Average position of Hep3B cells within the microwell chip measured as distance from the bottom of the well based on our process described in section 4.2.11. Error bars represent SEMs, n = 72.

4.3.3. Growth Factor Leaching

The results of our leaching indicate that we were able to observe leaching effects primarily within the first 24 hours that slowly increased over time (Figure 15). Moreover,

growth factor leaching was greater without MHS continuously, and was completely released by four days after printing, though the rate of release seemed to dissipate after the first day. Samples bound to MHS had a slower, but continual release profile. This linear release is consistent with literature values for growth factor release studies for heparin sulfate-bound samples [215,216]. Thus, our results indicate the need for MHS to stabilize growth factors in hydrogels.
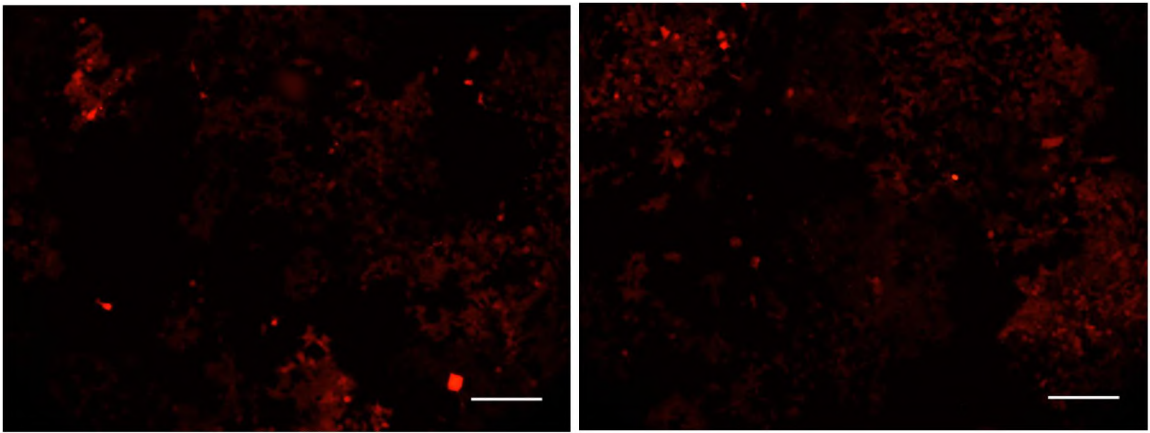
Figure 14. 2D cells infected with lentiviruses containing expression for mCherry 2D images on a 96 well plate of cells 15 passages after transduction. Scale bar = 200 μm.

A

B
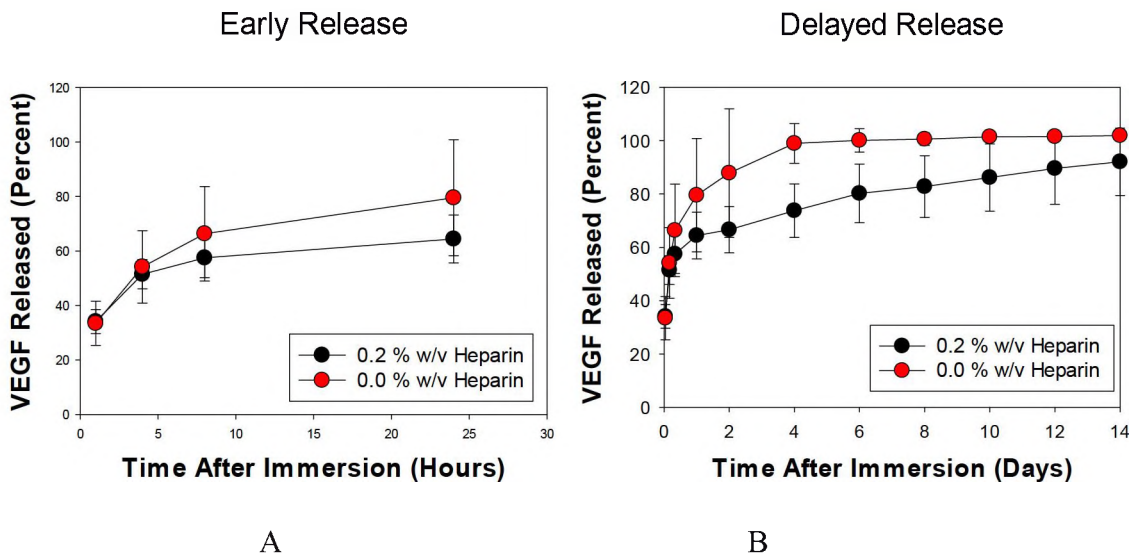
Figure 15. Analysis of the leaching of 1 µg/mL bFGF from OMA-45 either mixed with 0.2 w/v % heparin or no heparin A) within the first 24 hours of immersion B) for the duration of the experiment. Error bars represent SEMs, n = 12.

4.3.4. Cell Growth in 384-Pillar Plates with Sidewalls

The results of our cell growth experiments are shown in Figure 5. As it can be seen, cells successfully proliferated for up to two weeks after the initial print, though it was hard to quantify differences in fluorescence intensity in significantly proliferated samples after day 6 due to the saturation in fluorescence at 100 gain after day 6. It is hard to give an exact cell count with this procedure, given the nature of spheroid formation potentially amplifying or impeding red signals. Samples were initially rather dark on day 0 owing to the fact that after infected Hep3B cells are passaged, mCherry expression subsequently decreases and takes time to recover, which likely results in underestimating the actual cell number on day 0. The samples that proliferated the most were all, HGF, and TGFβ1. Furthermore, we observed spheroid cultures forming within the plate, indicating that our platform is suitable for long term 3D culture. Spheroid generation seemed to increase with time and start forming 4-6 days after the initial print for all conditions regardless of the presence of growth factors. Fluorescence intensity of infected cells increased with time up to about six days after seeding indicating that the infection also has long term stability in 3D culture and can be used to monitor the cells. Additionally, spheroid cultures formed readily here unlike in microwell chips where cells seemed to proliferate though with limited growth potential. This shows that the 384-pillar plate with sidewalls is better for long-term sustenance of cell growth and mimicking the HCC tumor architecture than microwell chips. One drawback is the formation of bubbles that can occur between layers, which somewhat hampered our ability to monitor migration and adequately quantify fluorescence.

94

Conditions which seemed to cause the greatest formation of spheroids were cells in the presence of HGF and the combination of growth factors. This proliferation is reflective of the effect this growth factor has on the cells *in vivo*. Other growth factors did not induce the formation of spheroids as compared to the absence of growth factors.
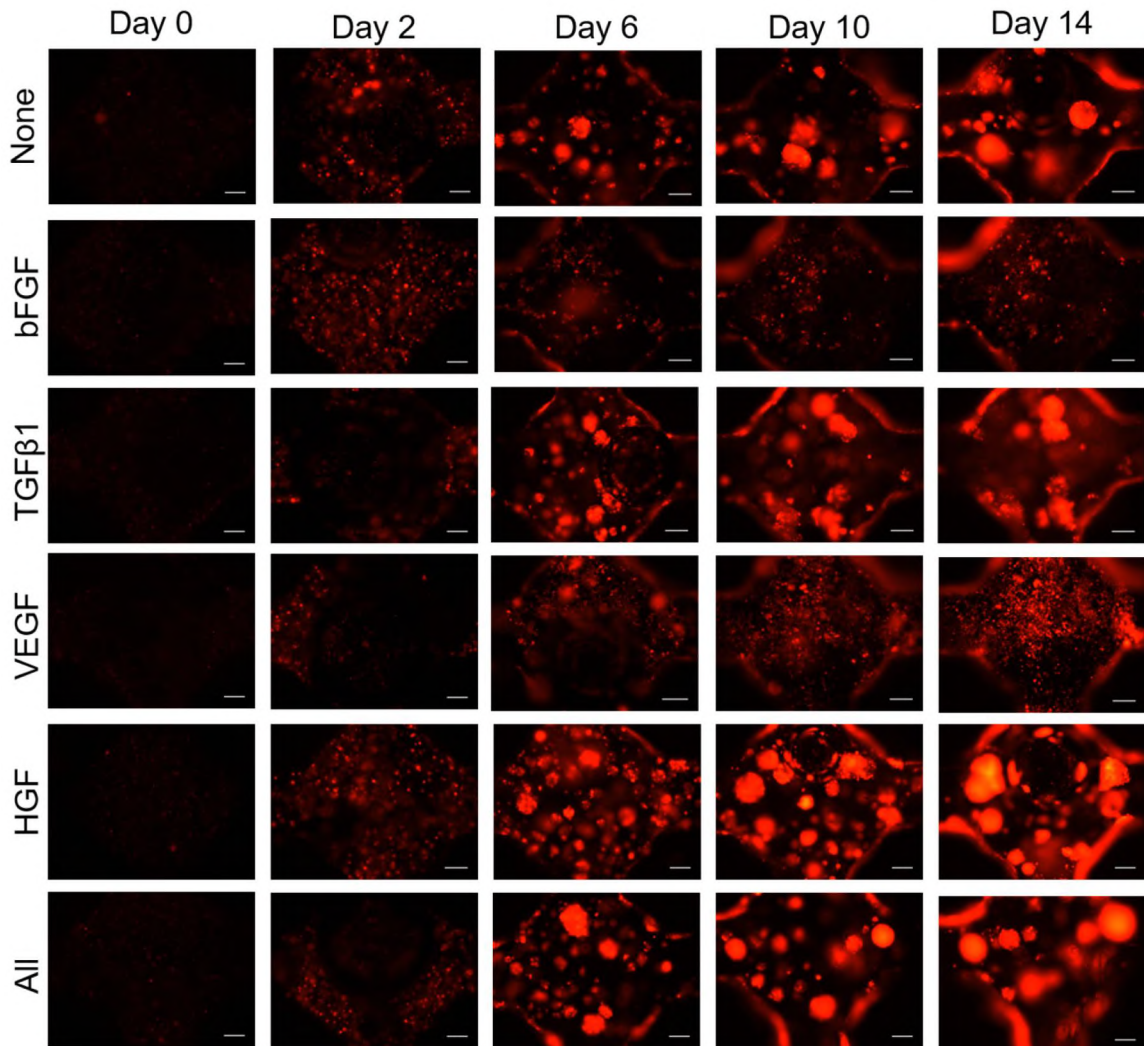
A
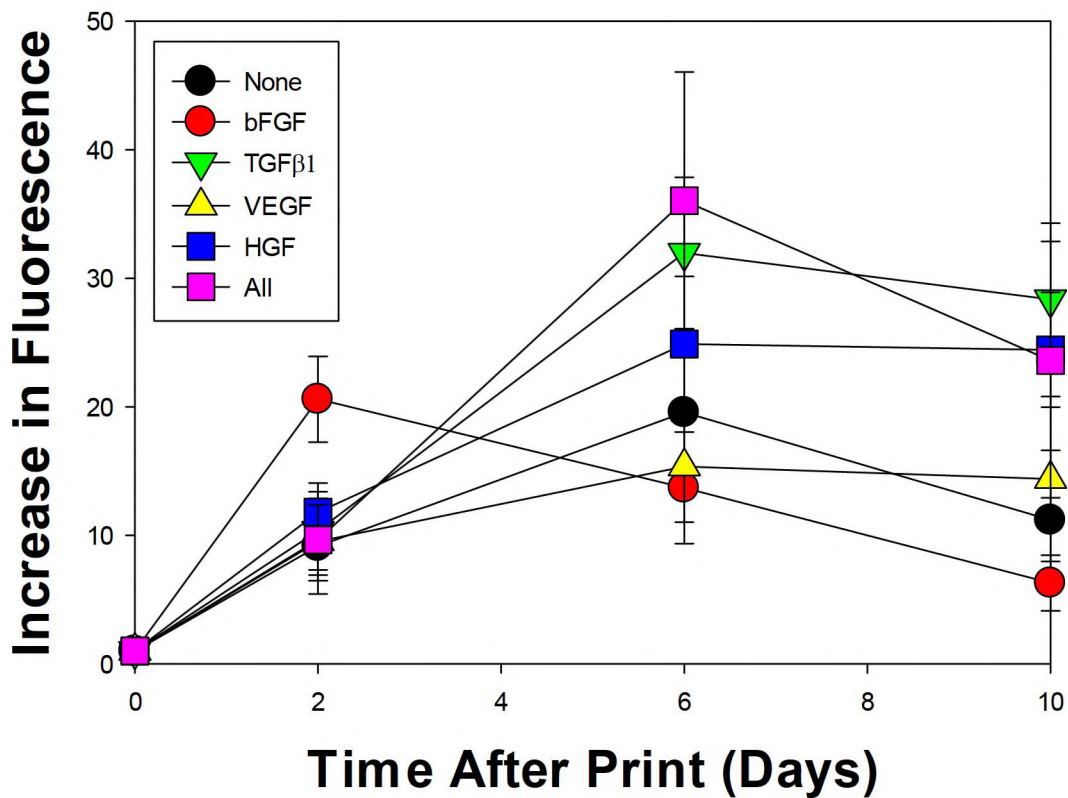
B

Figure 16. A) Representative images of Hep3B cells expressing mCherry in a 384-pillar plate with sidewalls after being exposed to various growth factors for up to two weeks. Images were taken 500 μm away from the pillar surface Scale bar = 200 μm. B) Fluorescence intensity changes as a function of time. For fluorescence intensity, this reflects the total fluorescence observed summed over all z-positions. Error bars represent SEMs, n = 12.

4.3.5. Migration in 384-Pillar Plates with Sidewalls

The results of our migration experiments in 384-pillar plates with sidewalls is shown in Figure 17, with rates of migration discussed in Table 6, with deviations in linearity denoted by root square mean (R^2). All conditions were found to have an average initial position between 740 and 750 μm from the pillar surface, which is consistent with where the start of the second layer should be given the area between the sidewalls. We found some levels of migration to be promoted with VEGF, bFGF, TGFβ1, and

combinatorial growth factors, while HGF did not seem to induce migration relative to controls. Most of this migration seemed to take place later in the assay, though error was significantly large at individual time points to show no individual deviations between samples at individual time points. Even still, the trends for movement towards the layer with printed growth factors and against gravity were apparent. In all cases, there was some movement towards the first printed layer, particularly later in the assay. HGF and control samples showed relatively little migration. We were able to distinguish spheroid formation vs. migration by eliminating out of focus cells using our developed in-house macro, which eliminates low and high frequencies after undergoing FFT. Migration potential was greatest in the case of VEGF, followed by combinations of growth factors used. bFGF, VEGF, and combination growth factor used generally showed migration moving in the direction of growth factors, while TGFβ1 exposed samples did not necessarily follow the same continue trend.
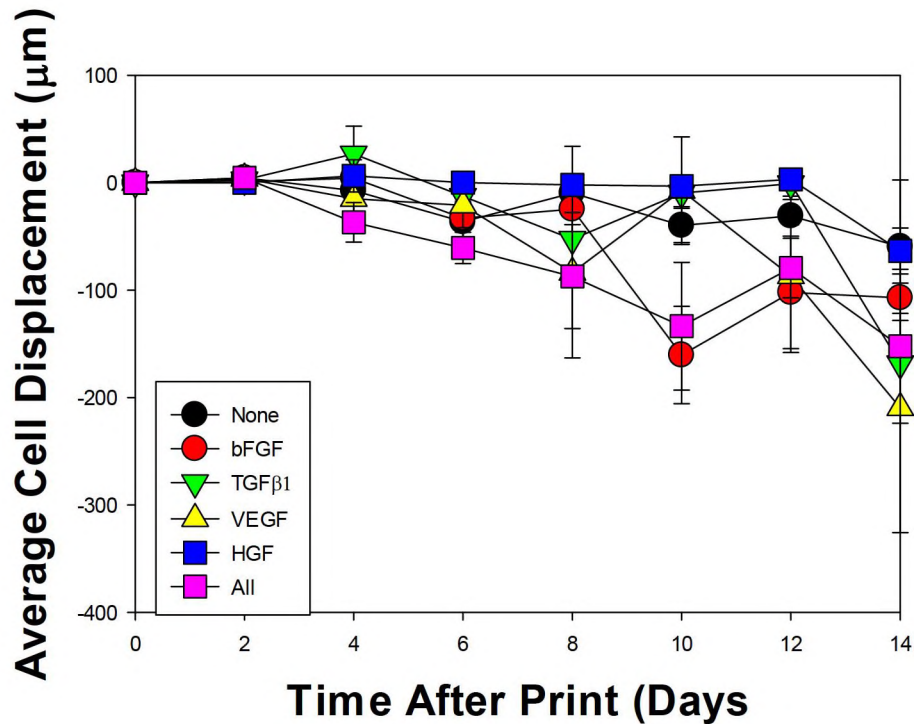
Figure 17. Relative average position of cells in the presence of growth factors as a function of time. Note: 500 µm from the pillar surface represents the distance beneath the pillar surface, meaning decreases in height represent movement of cells against gravity. Error bars represent SEMs, n = 12.

Table 6. Average Cell Migration as a Function of Growth Factor

Exposed Growth Factor	Average Cell Movement (µm/day)	R^2
None	-3.96	0.74
bFGF	-10.42	0.67
TGFβ1	-8.01	0.41
VEGF	-11.68	0.61
HGF	-2.73	0.34
All	-10.73	0.84

4.4. Discussion

In this work, we created a high-throughput cancer cell migration assay. To perform this study, we combined several different engineering designs, including the creation of a fluorescent lentivirus for subsequent transfection in a cell line to make permanently fluorescence Hep3B cells, synthesized a chemically modified version of alginate that is photopolymerizable, engineered a platform capable of supporting 3D cell-culture that is compatible with other high-throughput technologies, and developed our own image processing capabilities to fully analyze cell migration. Integrating these engineering strategies creates a platform through which 3D cell migration and cell proliferation can be monitored in real-time and in high throughput for up to two weeks after initial cell seeding.

Initially we attempted to study migration in a microwell chip using calcein and ethidium stains. This protocol was based on previous work performed in Chapter III where we optimized OMA viability and polymerization in microwell chips. While cells were viable out to two weeks, growth seemed to be static within the microwell chips as compared to the 384-pillar plate with sidewalls. We suspect this is due to potential nutrient deprivation experienced by cells within the microwells, as we successfully generated spheroid culture within the 384-pillar plate with sidewalls. The design of the microwell chips allows for nutrients to diffuse through one surface: the top interface between the hydrogel and the cell culture media. Cells further from this surface are less likely to see any nutrients and oxygen, meaning there are diffusion limitations to their growth. This is not a problem in the 384-pillar plate with sidewalls, as the slits between the sidewalls give encapsulated cells more access to nutrients.

While spot detachment has been an issue with a previously designed 384-pillar plate and micropillar chips, the combination of surface modifications our group previously developed and the capillary forces within the depression in the pillar serve to anchor the hydrogel to the pillar. Bubble formation was somewhat of an issue with printing as the nozzles with our machine are designed to print smaller volumes that 2 µL droplets, and bubbles could also get trapped between printed layers. Additionally, bubbles within the media in 384 well plates could be trapped within the pillars, so care needs to be taken when media is dispensed into the 384-well plate.

Hep3B cells were successfully transduced with lentivirus containing mCherry at about an 80-90 % transduction efficiency. Moreover, the lentivirus expression was stable, as cells passaged ten times after transduction still expressed mCherry. The expression of

the lentivirus was optimal about 3-4 days after passaging when cells reached 80-90 % confluence on the T-flask. We believe that the reason for this is that as cells are passaged, cell surface proteins are affected, which diverts much of the cells' energy towards processes to ensure their survival. This result is consistently reflected in our migration/growth studies, where samples at day 0 produced relatively little fluorescence that was only observable after two days growth. After cells are passaged, they are more likely to proliferate in either 2D or 3D conditions, which explains why this expression is stronger days after passaging. Moreover, the use of lentivirus transduced cells allows us to monitor cell movement in real time without disposing our samples. With calcein-stained samples, cells had to be disposed of after staining due to the degradation of the fluorophore over time and the toxicity associated with increased exposure to the fluorophore. This means that only end-point monitoring of migration could be performed with stained samples, so migration could not be accurately assessed with the stained samples.

We were able to successfully encapsulate growth factors within OMA for slow release for our migration studies. MHS was used for binding to growth factors to stabilize them within OMA. The tested growth factors all have sites that natural bind to heparin sulfate which is to allow for a slower release of growth factors from the hydrogel [83,130,217–219]. Ultimately, we found that MHS does stabilize growth factor in OMA after an initial quick leach in the first 24 hours with an extended linear leach after that time, while VEGF in the absence of heparin sulfate also had a much faster immediate leach and was fully leached within four days. While many of release studies done on growth factor-heparin binding are conducted directly on the surface of materials, growth factors have more ways to escape the matrix in the 384-pillar plate with sidewalls. This potentially had

an impact on the growth factor leaching, which may have also been exacerbated given the small area for polymerization and migration, producing an initially very fast first leach. In the case of the heparin-bound samples, we believe the initial release growth factor is from unbound VEGF. Jeon et al have demonstrated the use of these growth factors at lower concentrations, producing linear release profiles [220]. This means that the growth factor concentration relative to the heparin sulfate may be high, producing the quick release seen in the first 24 hours for both samples. Strong initial release kinetics of heparin-bound VEGF have been observed previously, though it tends to have a linear release profile after the first day following our MHS model [216,220]. One other thing to note is that heparin sulfate binding and release kinetics can vary between growth factors, so it is quite possible more or less growth factor is released when using other growth factors [220–222]. This may produce different release profiles, though this behavior is expected to also be gradual if binding is successful. While there is still leaching of growth factors in the presence of MHS, ultimately the concentration of leached growth factors in media is still significantly less than the growth factor concentration in the printed OMA layer.

One of the major factors that also plays a role in migration and tumorgenesis is the role of O_2 diffusion within the tumor. As hypoxia is common in larger tumors, cells in parts of the tumor are necrotic, while others begin moving in search of more nutrients, and O_2 in particular. The transcription factor hypoxia-inducible factor 1-alpha (HIF-1α) which is downregulated by the presence of O_2 is known to cause the expression of various proteins that signal for angiogenesis and proliferation, specifically upregulating both VEGF and TGFβ1 *in vivo* [223]. Additionally, HIF-1α is tied to the expression of metastatic and invasion cues, including several matrix metalloproteases (MMPs) and the c-Met

[6,223,224]. With the formation of cancer spheroids within our system, the growth factors we supplemented are also secreted within the spheroids themselves, which can further enhance growth or migration.

We have successfully shown that several of our growth factors can trigger the expansion of Hep3B cells into spheroid structures. Some of these growth factors like HGF [225,226] and bFGF [83] are known to initiate cell growth independent of the status of the cancer. What was interesting was that growth was greatest in the presence of HGF more than other growth factors or the combination of growth factors. It is known that Hep3B cells do proliferate in response to stellate cells secretion of HGF [226]. This is likely due to the fact the HGF is secreted by stem cells in the liver to assist in wound healing. While it is unknown if Hep3B functions in the stem-cell like nature of cancer cells, it is known that all of these growth factors can induce the proliferation of hepatic cells, including several known cancer cell lines. Hep3B in particular is known to express high-levels of FGF receptor II (FGFRII), which binds to bFGF [227]. Comparatively, Hep3B cells also secrete higher levels of TGFβ1, which may also explain why they too experienced increased proliferation in the presence of this growth factor [227]. Since spheroid formation can occur independent the presence of growth factors (though it is enhanced by certain growth factors), it is important to eventually quantify the growth factors that are secreted instead of delivered. Subsequent growth factor quantification for intracellular production of growth factors can be performed looking at the genetic expression of the growth factors within the cell or performing western blot analysis on isolated cell samples.

Our results showed a mixed amount of migration, that was growth-factor dependent. Specifically, bFGF and VEGF (and, to a lesser extent, TGFβ1) seemed to stimulate

migration, while HGF did not generate much cellular movement. This is likely due to bFGF's, TGFβ1's and VEGF's roles in angiogenesis [28,209] and HGF's role in proliferation [226]. While spheroid formation did occur in all conditions, spheroid formation seemed to be contained to the second printed layer and individual cells migrated to the first printed layer as observed by the fact that spheroids did not exist near the pillar surface where the growth factors were printed. We believe this is due to the fact that while angiogenic growth factors seem to play a role in inducing migration, the growth factors that play a role in cell proliferation will not impact migration. Individual cells, particularly ones searching for nutrients, are able to move through the matrix, while the tumors themselves are static within the culture.

Another interesting result is that the combination of growth factors experiment yielded more migration than the control, but less than VEGF experiments, and how proliferation seemed to increase in the combination growth factor experiment relative to the control but was less than the HGF and TGFβ1 cases by day ten. We believe this is due to the limitation of room for heparin to bind growth factors. Thus, the combination experiment likely had less growth factor bound long term as all four growth factors were competing for the same space, which resulted in a response that trends towards the presence of individual growth factors but is somewhat muted because there are less overall.

4.5. Conclusions

We successfully developed a high-throughput 3D cell migration assay on a platform compatible with 384-well plates. The migration assay was able to quantify relative rates of migration in real-time for up to two weeks after initial seeding. We were also able to

quantify proliferation rates of Hep3B cells in the presence of various growth factors. Our results reflected in literature that growth factors that promote angiogenesis also induce HCC migration and metastasis. Subsequent studies will look into comparing Hep3B cells with other cell lines so as to use this platform as a potential diagnostic marker for HCC. We also hope to look at different combinations of growth factors and ECM components as chemoattractants for cell migration and incorporate fibroblasts for co-culture to study the effects of restructuring of the ECM during angiogenesis and metastasis of HCC.

4.6. Acknowledgements

CHAPTER V

CONCLUSIONS AND FUTURE DIRECTIONS

5.1. Conclusions

There is a recent shift in the development of *in vitro* cell cultures for modeling liver disease from using 2D cultures to 3D cultures. This shift reflects the desires of individuals from academia and industry to have a model that reflects the *in vivo* behavior. These models can be of use in drug development for toxicity and efficacy studies, or as diagnostic and treatment tools as well. This thesis details methods for creating 3D liver cultures and assays for use in better understanding liver diseases, specifically focusing on HCC and ADRs. In this study, we have successfully used and optimized three different platforms and two hydrogels for the culture of Hep3B cells in 3D. We have also demonstrated how viral transductions can be used to code for various fluorescent proteins. Furthermore, we showed how we can use Hep3B cells transfected with lentiviruses can be tracked for a high-throughput 3D cell migration and invasion assay, and that this assay can be successfully conducted for up to two weeks after initial seeding.

The work presented here has several implications for industrial, pre-clinical, and academic use. The surface modification techniques discussed in aims 1 and 2 give

researchers methods for immobilizing hydrogels onto polystyrene surfaces. In addition, these modifications are suitable hydrogel-based microarray technologies, as our group has subsequently used both PMA-OD and plasma treatment to immobilize other hydrogels onto the surfaces of our polystyrene-based microarray platforms. In aims 1 and 3, we successfully transduced viruses into cells containing the expression of fluorescent proteins. In the case of PuraMatrix, this transduction means that encapsulated cells may be transduced with adenoviruses *in situ*, allowing for scientists to modify the genetic expression within encapsulated cells. This allows researchers to study various disease states, including genetic polymorphisms that may affect DILI or HCC. DILI is a likely candidate for future studies as cells encapsulated in PuraMatrix exhibited dose-dependent responses to several tested toxic compounds. The transduction performed using lentiviruses on Hep3B cells created a permanently fluorescent cell line that could be used to track cell growth and movement *in vitro*. We optimized the polymerization parameters for two hydrogels for microscale tissue culture, which allows for both of these hydrogels to be used in other small-scale tissue cultures. Finally, aim 3 also saw the development of a high-throughput, quantitative 3D cell migration assay. The techniques developed in the third aim can be applied for monitoring multiple cell types if different cell types contain individual fluorescent tags, meaning that more complex tissue models can be studied. While this assay was designed with HCC in mind, other types of cancer or any mammalian cells that respond to the presence of growth factors can also be assessed. Table 7 presents the key findings of these studies.

Table 7. Summary of Results from Individual Aims

Aim 1	Aim 2	Aim 3
Encapsulate hepatic cells in hydrogels that can be used for high-throughput drug screening and *in situ* adenoviral transduction	Optimize hepatic cell encapsulation conditions in a photopolymerizable hydrogel for creating layered cell structures	Simulate migration of liver cancer cells in 3D and quantify their migration *in situ* in high throughput
• Provided robust spot attachment between hydrogels and micropillar chips • Optimized polymerization of PuraMatrix on the micropillar chip • Transduced adenoviruses into encapsulated Hep3B cells • Demonstrated dose-response behavior of encapsulated cells	• Optimized surface plasma treatment of microwell chips • Found optimal parameters for OMA polymerization based on background color, PI concentration, OMA concentration, light intensity/duration, and methacrylation percentage	• Created a macro that can quantify cell migration in 3D • Transduced lentiviruses into Hep3B cells containing expression for mCherry • Demonstrated stability of MHS-bound growth factors in OMA for two-week long leaching. • Proliferated encapsulated Hep3B cells for two weeks after seeding • Demonstrated migration of Hep3B cells in response to angiogenic factors

5.2. Future Directions and Recommendations

1) Cells encapsulated in PuraMatrix are susceptible to toxicity due to the handling of the cells before printing and the rather low pH of the hydrogel before the washing steps. Other cell lines may be less susceptible to the toxic effects of this hydrogel. Additionally, as demonstrated within the first aim, Hep3B cells can be transduced with adenoviruses *in situ*. Future experiments can focus on transductions carrying genes coding for various DMEs with a focus on DILI.

2) Temperature is a major factor when controlling for toxicity associated with OMA polymerization. This is the reason why gelation and viability were optimized on a narrow

range of conditions. If the height of the lamp above the exposed surface is changed, remember to also change the exposure intensity accordingly.

3) The roughness of the surface increases the duration of plasma treatment necessary to prevent bubble formation. Smoother polystyrene surfaces can be plasma exposed for as little as five minutes to ensure proper functionalization. All of our scaffolds are generally considered to not be smooth, but other microarray technologies may be different.

4) While we demonstrated the migration potential of Hep3B cells, we did not compare these results to other HCC cells lines, patient samples, other kinds of cancer, or other cells that are known to move in response to various cues. As a potential diagnostic assay, future studies should focus on comparing migration potential of Hep3B cells against other known tumor cell lines and explanted tumor tissue and using other chemorepellants and chemoattractants to induce migration.

5) Our current system does not account for growth factor generation during cancer cell proliferation, and there is no discussion of understanding the role of O_2 transport in the behavior of cells within the spheroids. To fully understand these phenomena, it is necessary to model transport of growth factors and O_2 within the spheroid, and possibly monitor expression of HIF-1α or try to stain hypoxic regions within the samples.

6) Our platform is ideally suited for combinatorial studies, yet most of the experiments were performed with high numbers of replicates with few combinatorial studies done to limit error. Work on the micropillar chip does not focus on the impacts of multiple drugs within a system, and the work on the 384-pillar plate with sidewalls uses only one or four combinations of growth factors to study migration. Additionally, growth factor concentration was fixed for the study.

7) ECM components were not incorporated as another mechanism that could impact cell proliferation and migration, which is especially important in the tumor microenvironment.

8) The cancer microenvironment consists of several different cell types, so the current model is rather simplistic from a biological perspective. Future experiments will focus on the use co-cultures of fibroblasts and HCC cells to model the restructuring of the tumor during angiogenesis. If these experiments are successful, we may incorporate some cells of the immune system as well.

9) As use of the 384-pillar plate with side walls was suitable for fourteen days of cell culture, we hope to expand the time used in the culture to longer periods. Furthermore, we hope to use the system to model the behavior of cells in liver co-cultures and look into organoid development on this platform to study liver biology and other liver diseases.

REFERENCES

1.   Your Liver. In: American Liver Foundation [Internet]. 2017. Available:
      https://liverfoundation.org/for-patients/about-the-liver/

2.   Chronic Liver Disease and Cirrhosis. In: Center for Disease Control [Internet].
      2016. Available: https://www.cdc.gov/nchs/fastats/liver-disease.htm

3.   Chen C, Wang G. Mechanisms of hepatocellular carcinoma and challenges and
      opportunities for molecular targeted therapy. World J Hepatol. 2015;7: 1964–1970.
      doi:10.4254/wjh.v7.i15.1964

4.   De Minicis S, Marzioni M, Benedetti A, Svegliati-Baroni G. New insights in
      hepatocellular carcinoma: from bench to bedside. Ann Transl Med. 2013;1: 15.
      doi:10.3978/j.issn.2305-5839.2013.01.06

5.   Moudgil V, Redhu D, Dhanda S, Singh J. A Review of Molecular Mechanisms in
      the Development of Hepatocellular Carcinoma by Aflatoxin and Hepatitis B and C
      Viruses. J Environ Pathol Toxicol Oncol. 2013;32: 165–175.
      doi:10.1615/JEnvironPatholToxicolOncol.2013007166

6.   Hernandez-Gea V, Toffanin S, Friedman SL, Llovet JM. Role of the
      microenvironment in the pathogenesis and treatment of hepatocellular carcinoma.
      Gastroenterology. Elsevier Inc.; 2013;144: 512–527.
      doi:10.1053/j.gastro.2013.01.002

7.   Tujios S, Fontana RJ. Mechanisms of Drug Induced Liver Injury: From Bedside to

Bench. J Nat Rev Gastroenterol Hepatol. 2011;8: 202–211.

8.   Chen M, Bisgin H, Tong L, Hong H, Fang H, Borlak J, et al. Toward predictive models for drug-induced liver injury in humans: are we there yet? Biomark Med. 2014;8: 201–13. doi:10.2217/bmm.13.146

9.   Ng W, Lobach ARM, Zhu X, Chen X, Liu F, Metushi IG, et al. Animal models of idiosyncratic drug reactions. Adv Pharmacol. San Diego, California: Elsevier Inc.; 2012;63: 81–135. doi:10.1016/B978-0-12-398339-8.00003-3

10. Ettlin RA. Toxicologic pathology in the 21st century. Toxicol Pathol. 2013;41: 689–708. doi:10.1177/0192623312466192

11. Michelotti GA, Machado M V., Diehl AM. NAFLD, NASH and liver cancer. Nat Rev Gastroenterol Hepatol. Nature Publishing Group; 2013;10: 656–665. doi:10.1038/nrgastro.2013.183

12. Soldatow VY, Lecluyse EL, Griffith LG, Rusyn I. In Vitro Models for Liver Toxicity Testing. Toxicol Res (Camb). 2013;23: 23–39. doi:10.1039/c2tx20051a

13. Benam KH, Dauth S, Hassell B, Herland A, Jain A, Jang K-J, et al. Engineered In Vitro Disease Models. Annu Rev Pathol Mech Dis. 2015;10: 195–262. doi:10.1146/annurev-pathol-012414-040418

14. LeCluyse EL, Witek RP, Andersen ME, Powers MJ. Organotypic liver culture models: Meeting current challenges in toxicity testing. Crit Rev Toxicol. 2012;42: 501–548. doi:10.3109/10408444.2012.682115

15. Skardal A, Smith L, Bharadwaj S, Atala A, Soker S, Zhang Y. Tissue specific

synthetic ECM hydrogels for 3-D in vitro maintenance of hepatocyte function. Biomaterials. 2012;33: 4565–4575. doi:10.1016/j.biomaterials.2012.03.034

16. Herceg Z, Paliwal A. Epigenetic mechanisms in hepatocellular carcinoma: How environmental factors influence the epigenome. Mutat Res - Rev Mutat Res. Elsevier B.V.; 2011;727: 55–61. doi:10.1016/j.mrrev.2011.04.001

17. Arzumanyan A, Reis HMGPV, Feitelson MA. Pathogenic mechanisms in HBV- and HCV-associated hepatocellular carcinoma. Nat Rev Cancer. 2013;13: 123–135. doi:10.1038/nrc3449

18. Gripon P, Rumin S, Urban S, Le Seyec J, Glaise D, Cannie I, et al. Infection of a human hepatoma cell line by hepatitis B virus. Proc Natl Acad Sci U S A. 2002;99: 15655–15660. doi:10.1073/pnas.232137699

19. Mathew S, Ali A, Abdel-Hafiz H, Fatima K, Suhail M, Archunan G, et al. Biomarkers for virus-induced hepatocellular carcinoma (HCC). Infect Genet Evol. Elsevier B.V.; 2014;26: 327–339. doi:10.1016/j.meegid.2014.06.014

20. Shlomai A, de Jong YP, Rice CM. Virus associated malignancies: The role of viral hepatitis in hepatocellular carcinoma. Semin Cancer Biol. 2014;26: 78–88.

21. Shlomai A, Schwartz RE, Ramanan V, Bhatta A, de Jong YP, Bhatia SN, et al. Modeling host interactions with hepatitis B virus using primary and induced pluripotent stem cell-derived hepatocellular systems. Proc Natl Acad Sci U S A. 2014;111: 1–6. doi:10.1073/pnas.1412631111

22. Denniston MM, Jiles RB, Drobeniuc J, Klevens RM, Ward JW, McQuillan GM, et

al. Chronic Hepatitis C Virus Infection in the United States, National Health and Nutrition Examination Survey 2003 to 2010. Ann Intern Med. 2014;160: 293–+. doi:10.7326/m13-1133

23.   Aravalli RN, Steer CJ, Cressman ENK. Molecular mechanisms of hepatocellular carcinoma. Hepatology. 2008;48: 2047–2063. doi:10.1002/hep.22580

24.   Qi LN, Bai T, Chen ZS, Wu FX, Chen YY, De Xiang B, et al. The p53 mutation spectrum in hepatocellular carcinoma from Guangxi, China : Role of chronic hepatitis B virus infection and aflatoxin B1 exposure. Liver Int. 2015;35: 999–1009. doi:10.1111/liv.12460

25.   Koul HK, Pal M, Koul S. Role of p38 MAP Kinase Signal Transduction in Solid Tumors. Genes Cancer. 2013;4: 342–359. doi:10.1177/1947601913507951

26.   Hammerich L, Heymann F, Tacke F. Role of IL-17 and Th17 Cells in Liver Diseases. Clin Dev Immunol. 2011; 1–12. doi:10.1155/2011/345803

27.   Anastas JN, Moon RT. WNT signalling pathways as therapeutic targets in cancer. Nat Rev Cancer. Nature Publishing Group; 2013;13: 11–26. doi:10.1038/nrc3419

28.   Vilchez V, Turcios L, Marti F, Gedaly R. Targeting Wnt/β-catenin pathway in hepatocellular carcinoma treatment. World J Gastroenterol. 2016;22: 823–832. doi:10.3748/wjg.v22.i2.823

29.   Pez F, Lopez A, Kim M, Wands JR, Caron De Fromentel C, Merle P. Wnt signaling and hepatocarcinogenesis: Molecular targets for the development of innovative anticancer drugs. J Hepatol. European Association for the Study of the

Liver; 2013;59: 1107–1117. doi:10.1016/j.jhep.2013.07.001

30. Ayub A, Ashfaq UA, Haque A. Review Article HBV Induced HCC : Major Risk Factors from Genetic to Molecular Level. Biomed Res Int. 2013;2013: 1–14.

31. Ma L, Chua MS, Andrisani O, So S. Epigenetics in hepatocellular carcinoma: An update and future therapy perspectives. World J Gastroenterol. 2014;20: 333–345. doi:10.3748/wjg.v20.i2.333

32. Callegari E, Elamin BK, Sabbioni S, Gramantieri L, Negrini M. Role of microRNAs in hepatocellular carcinoma: A clinical perspective. Onco Targets Ther. 2013;6: 1167–1178. doi:10.2147/OTT.S36161

33. Kew MC. Aflatoxins as a cause of hepatocellular carcinoma. J Gastrointest Liver Dis. 2013;22: 305–310.

34. Wands JR, Kim M. WNT/β-catenin signaling and hepatocellular carcinoma. Hepatology. 2014;60: 452–454. doi:10.1002/hep.27081

35. Mace K, Aguilar F, Wang J-S, Vautravers P, Gomez-Lechon M, Gonzalez FJ, et al. Aflatoxin B1-induced DNA adduct formation and p53 mutations in CYP450-expressing human liver cell lines. Carcinogenesis. 1997;18: 1291–1297. doi:DOI 10.1093/carcin/18.7.1291

36. Bruix J, Gores GJ, Mazzaferro V. Hepatocellular carcinoma: Clinical frontiers and perspectives. Gut. 2014;63: 844–855. doi:10.1136/gutjnl-2013-306627

37. Tang S-W, Lv X-Z, Zhang Y, Wu S-S, Yang Z-R, Xia Y-Y, et al. CYP2E1, GSTM1 and GSTT1 genetic polymorphisms and susceptibility to antituberculosis

drug-induced hepatotoxicity: a nested case-control study. J Clin Pharm Ther. 2012;37: 588–93. doi:10.1111/j.1365-2710.2012.01334.x

38. Teixeira RL de F, Morato RG, Cabello PH, Muniz LMK, Moreira ADSR, Kritski AL, et al. Genetic polymorphisms of NAT2, CYP2E1 and GST enzymes and the occurrence of antituberculosis drug-induced hepatitis in Brazilian TB patients. Mem Inst Oswaldo Cruz. 2011;106: 716–724. doi:http://dx.doi.org/10.1590/S0074-02762011000600011

39. Mittal S, El-Serag HB. Epidemiology of HCC: Consider the Population. J Clin Gastroenterol. 2013;47: 1–10. doi:10.1097/MCG.0b013e3182872f29.Epidemiology

40. Park EJ, Lee JH, Yu G-Y, He G, Ali SR, Holzer RG, et al. Dietary and genetic obesity promote liver inflammation and tumorigenesis by enhancing IL-6 and TNF expression. Cell. 2010;140: 197–208. doi:10.1016/j.cell.2009.12.052

41. Choumar A, Tarhuni A, Lettéron P, Reyl-Desmars F, Dauhoo N, Damasse J, et al. Lipopolysaccharide-induced mitochondrial DNA depletion. Antioxid Redox Signal. 2011;15: 2837–54. doi:10.1089/ars.2010.3713

42. Abu El Makarem M. An overview of biomarkers for the diagnosis of hepatocellular carcinoma. Hepat Mon. 2012;12. doi:10.5812/hepatmon.6122

43. Witjes CDM, Van Aalten SM, Steyerberg EW, Borsboom GJJM, De Man RA, Verhoef C, et al. Recently introduced biomarkers for screening of hepatocellular carcinoma: A systematic review and meta-analysis. Hepatol Int. 2013;7: 59–64.

doi:10.1007/s12072-012-9374-3

44. Tsuchiya N, Sawada Y, Endo I, Saito K, Uemura Y, Nakatsura T. Biomarkers for the early diagnosis of hepatocellular carcinoma. World J Gastroenterol. 2015;21: 10573–10583. doi:10.3748/wjg.v21.i37.10573

45. Wolf MJ, Adili A, Piotrowitz K, Abdullah Z, Boege Y, Stemmer K, et al. Metabolic activation of intrahepatic CD8+T cells and NKT cells causes nonalcoholic steatohepatitis and liver cancer via cross-talk with hepatocytes. Cancer Cell. 2014;26: 549–564. doi:10.1016/j.ccell.2014.09.003

46. Asghar W, El Assal R, Shafiee H, Pitteri S, Paulmurugan R, Demirci U. Engineering cancer microenvironments for in vitro 3-D tumor models. Mater Today. Elsevier Ltd.; 2015;18: 539–553. doi:10.1016/j.mattod.2015.05.002

47. Kramer N, Walzl A, Unger C, Rosner M, Krupitza G, Hengstschläger M, et al. In vitro cell migration and invasion assays. Mutat Res - Rev Mutat Res. 2013;752: 10–24. doi:10.1016/j.mrrev.2012.08.001

48. Chen R-C, Yi P-P, Zhou R-R, Xiao M-F, Huang Z-B, Tang D-L, et al. The role of HMGB1-RAGE axis in migration and invasion of hepatocellular carcinoma cell lines. Mol Cell Biochem. 2014;390: 271–280. doi:10.1007/s11010-014-1978-6

49. Carr BI, Alessandro RD, Refolo MG, Iacovazzi PA, Lippolis C, Messa C, et al. Effects of Low Concentrations of Regorafenib and Sorafenib on Human HCC Cell AFP , Migration , Invasion , and Growth In Vitro. J Cell Physiol. 2012; 1344–1350. doi:10.1002/jcp.24291

50. Poujade M, Hertzog A, Jouanneau J, Chavrier P, Ladoux B, Buguin A. Collective migration of an epithelial monolayer in response to a model wound. PNAS. 2007;104: 15988–15993.

51. Cai G, Lian J, Shapiro SS, Beacham DA. Evaluation of endothelial cell migration with a novel in vitro assay system. Methods Cell Sci. 2000;22: 107–114.

52. Nieto N, Lutolf MP. Extracellular matrix bioengineering and systems biology approaches in liver disease. Syst Synth Biol. 2011;5: 11–20. doi:10.1007/s11693-011-9085-4

53. Lee H, Jeng Y, Chen Y. Gas6 / Axl pathway promotes tumor invasion through the transcriptional activation of Slug in hepatocellular carcinoma. Carcinogenesis. 2018;35: 769–775. doi:10.1093/carcin/bgt372

54. Chen Y, Wang T, Hsu H, Yuan R, Jeng Y. Overexpression of CTHRC1 in Hepatocellular Carcinoma Promotes Tumor Invasion and Predicts Poor Prognosis. PLoS One. 2013;8: e70324. doi:10.1371/journal.pone.0070324

55. Zhang Y, Zhang X, Zhang J, Sun B, Zheng L, Li J. Microfluidic chip for isolation of viable circulating tumor cells of hepatocellular carcinoma for their culture and drug sensitivity assay. Cancer Biol Ther. Taylor & Francis; 2016;17: 1177–1187. doi:10.1080/15384047.2016.1235665

56. Kalchman J, Fujioka S, Chung S, Kikkawa Y, Mitaka T, Kamm RD, et al. A three-dimensional microfluidic tumor cell migration assay to screen the effect of anti-migratory drugs and interstitial flow. Microfluid Nanofluid. 2013;14: 969–981.

doi:10.1007/s10404-012-1104-6

57.   Takayama K, Kawabata K, Nagamoto Y, Kishimoto K, Tashiro K, Sakurai F, et al. 3D spheroid culture of hESC/hiPSC-derived hepatocyte-like cells for drug toxicity. Biomaterials. 2013;34: 1781–1789.

58.   Laschke MW, Menger MD. Spheroids as vascularization units: From angiogenesis research to tissue engineering applications. Biotechnol Adv. Elsevier; 2017;35: 782–791. doi:10.1016/j.biotechadv.2017.07.002

59.   Chen R, Dong Y, Xie X, Chen J, Gao D, Liu Y, et al. Screening candidate metastasis-associated genes in three-dimensional HCC spheroids with different metastasis potential. Int J Clin Exp Pathol. 2014;7: 2527–2535.

60.   Takai A, Fako V, Dang H, Forgues M, Yu Z, Budhu A, et al. Three-dimensional Organotypic Culture Models of Human Hepatocellular Carcinoma. Sci Rep. Nature Publishing Group; 2016;6: 21174. doi:10.1038/srep21174

61.   Geis T, Döring C, Popp R, Grossmann N, Fleming I, Hansmann M, et al. HIF-2alpha-dependent PAI-1 induction contributes to angiogenesis in hepatocellular carcinoma. Exp Cell Res. Elsevier; 2014;331: 46–57. doi:10.1016/j.yexcr.2014.11.018

62.   Tung Y-C, Hsiao AY, Allen SG, Torisawa Y, Ho M, Takayama S. High-throughput 3D spheroid culture and drug testing using a 384 hanging drop array. Analyst. 2011;136: 473–8. doi:10.1039/c0an00609b

63.   Cavnar SP, Salomonsson E, Luker KE, Luker GD, Takayama S. Transfer,

Imaging, and Analysis Plate for Facile Handling of 384 Hanging Drop 3D Tissue Spheroids. J Lab Autom. 2014;19: 208–214. doi:10.1177/2211068213504296

64.   Horman SR, To J, Orth AP, Cuddihy MJ, Caracino D. High-content analysis of three-dimensional tumor spheroids : investigating signaling pathways using small hairpin RNA. Nat Methods. Nature Publishing Group; 2013;10: v–vi. doi:10.1038/nmeth.f.370

65.   Raghavan S, Mehta P, Horst EN, Ward MR, Katelyn R. Comparative analysis of tumor spheroid generation techniques for differential in vitro drug toxicity. Oncotarget. 2016;7: 16948–16961.

66.   Ivanov DP, Parker TL, Walker DA, Alexander C, Ashford MB, Gellert PR, et al. Multiplexing Spheroid Volume , Resazurin and Acid Phosphatase Viability Assays for High-Throughput Screening of Tumour Spheroids and Stem Cell Neurospheres. PLoS One. 2014;9: e103817. doi:10.1371/journal.pone.0103817

67.   Otsuka H, Sasaki K, Okimura S, Nagamura M, Nakasone Y. Micropatterned co-culture of hepatocyte spheroids layered on non-parenchymal cells to understand heterotypic cellular interactions. Sci Technol Adv Mater. 2013;14: 1–10. doi:10.1088/1468-6996/14/6/065003

68.   Vinci M, Box C, Zimmermann M, Eccles SA. Tumor Spheroid-Based Migration Assays for Evaluation of Therapeutic Agents. Target Identification and Validation in Drug Discovery. 2013. pp. 253–266. doi:10.1007/978-1-62703-311-4

69.   Wolf KK, Vora S, Webster LO, Generaux GT, Polli JW, Brouwer KLR. Use of

cassette dosing in sandwich-cultured rat and human hepatocytes to identify drugs that inhibit bile acid transport. Toxicol vVtro. Elsevier Ltd; 2010;24: 297–309. doi:10.1016/j.tiv.2009.08.009

70. De Bruyn T, Chatterjee S, Fattah S, Keemink J, Nicolaï J, Augustijns P, et al. Sandwich-cultured hepatocytes: utility for in vitro exploration of hepatobiliary drug disposition and drug-induced hepatotoxicity. Expert Opin Drug Metab Toxicol. 2013;9: 589–616. doi:10.1517/17425255.2013.773973

71. Hrach J, Mueller SO, Hewitt P. Development of an in vitro liver toxicity prediction model based on longer term primary rat hepatocyte culture. Toxicol Lett. Elsevier Ireland Ltd; 2011;206: 189–196. doi:10.1016/j.toxlet.2011.07.012

72. Yip D, Cho CH. A multicellular 3D heterospheroid model of liver tumor and stromal cells in collagen gel for anti-cancer drug testing. Biochem Biophys Res Commun. Elsevier Inc.; 2013;433: 327–332. doi:10.1016/j.bbrc.2013.03.008

73. Nath S, Devi GR. Three-dimensional culture systems in cancer research: Focus on tumor spheroid model. Pharmacol Ther. Elsevier Inc.; 2016;163: 94–108. doi:10.1016/j.pharmthera.2016.03.013

74. Mitra A, Mishra L, Li S. Technologies for deriving primary tumor cells for use in personalized cancer therapy. Trends Biotechnol. Elsevier Ltd; 2013;31: 347–354. doi:10.1016/j.tibtech.2013.03.006

75. Bale SS, Vernetti L, Senutovitch N, Jindal R, Hegde M, Gough A, et al. In vitro platforms for evaluating liver toxicity. Exp Biol Med. 2014;239: 1180–1191.

doi:10.1177/1535370214531872

76. Kimlin LC, Casagrande G, Virador VM. In vitro three-dimensional (3D) models in cancer research: An update. Mol Carcinog. 2013;52: 167–182. doi:10.1002/mc.21844

77. Fang Y, Frampton JP, Raghavan S, Sabahi-Kaviani R, Luker G, Deng CX, et al. Rapid Generation of Multiplexed Cell Cocultures Using Acoustic Droplet Ejection Followed by Aqueous Two-Phase Exclusion Patterning. Tissue Eng Part C Methods. 2012;18: 647–657. doi:10.1089/ten.tec.2011.0709

78. Godoy P, Hewitt NJ, Albrecht U, Andersen ME, Ansari N, Bhattacharya S, et al. Recent advances in 2D and 3D in vitro systems using primary hepatocytes, alternative hepatocyte sources and non-parenchymal liver cells and their use in investigating mechanisms of hepatotoxicity, cell signaling and ADME [Internet]. Archives of toxicology. 2013. doi:10.1007/s00204-013-1078-5

79. Liu Y, Li H, Yan S, Wei J, Li X. Hepatocyte Cocultures with Endothelial Cells and Fibroblasts on Micropatterned Fibrous Mats to Promote Liver-Speci fi c Functions and Capillary Formation Capabilities. Biomacromolecules. 2014;15: 1044–1054.

80. Han S, Han L, Yao Y, Sun H, Zan X, Liu Q. Activated hepatic stellate cells promote hepatocellular carcinoma cell migration and invasion via the activation of FAK-MMP9 signaling. Oncol Rep. 2014;31: 641–648. doi:10.3892/or.2013.2872

81. Cheng J, Deng Y, Yi H, Wang G, Fu B, Chen W, et al. Hepatic carcinoma-

associated fi broblasts induce IDO-producing regulatory dendritic cells through IL-6-mediated STAT3 activation. Oncogenesis. 2016;5: e198. doi:10.1038/oncsis.2016.7

82.   Capece D, Fischietti M, Verzella D, Gaggiano A, Cicciarelli G, Tessitore A, et al./' The inflammatory microenvironment in hepatocellular carcinoma: A pivotal role for tumor-associated macrophages. Biomed Res Int. 2013;2013. doi:10.1155/2013/187204

83.   Tuleuova N, Lee JY, Lee J, Ramanculov E, Zern M a, Revzin A. Using growth factor arrays and micropatterned co-cultures to induce hepatic differentiation of embryonic stem cells. Biomaterials. Elsevier Ltd; 2010;31: 9221–31. doi:10.1016/j.biomaterials.2010.08.050

84.   Wan S, Zhao E, Kryczek I, Vatan L, Sadovskaya A, Ludema G, et al. Tumor-associated macrophages produce interleukin 6 and signal via STAT3 to promote expansion of human hepatocellular carcinoma stem cells. Gastroenterology. Elsevier, Inc; 2014;147: 1393–1404. doi:10.1053/j.gastro.2014.08.039

85.   Lee TK, Na KS, Kim J, Jeong HJ. Establishment of Animal Models with Orthotopic Hepatocellular Carcinoma. Nucl Med Mol Imaging (2010). 2014;48: 173–179. doi:10.1007/s13139-014-0288-y

86.   Ruggeri BA, Camp F, Miknyoczki S. Animal models of disease : Pre-clinical animal models of cancer and their applications and utility in drug discovery. Biochem Pharmacol. Elsevier Inc.; 2014;87: 150–161. doi:10.1016/j.bcp.2013.06.020

87.   Stanton MM, Samitier J, Sánchez S. Bioprinting of 3D hydrogels. Lab Chip. Royal Society of Chemistry; 2015;15: 3111–3115. doi:10.1039/C5LC90069G

88.   Rowley J a, Madlambayan G, Mooney DJ. Alginate hydrogels as synthetic extracellular matrix materials. Biomaterials. 1999;20: 45–53. Available: http://www.ncbi.nlm.nih.gov/pubmed/9916770

89.   Pawar SN, Edgar KJ. Alginate derivatization: A review of chemistry, properties and applications. Biomaterials. Elsevier Ltd; 2012;33: 3279–3305. doi:10.1016/j.biomaterials.2012.01.007

90.   Datar A, Joshi P, Lee M-Y. Biocompatible hydrogels for microarray cell printing and encapsulation. Biosensors. 2015;5: 647–663. doi:10.3390/bios5040647

91.   Sun J, Tan H. Alginate-based biomaterials for regenerative medicine applications. Materials (Basel). 2013;6: 1285–1309. doi:10.3390/ma6041285

92.   Lu Y, Song W, An D, Jun KB, Schwartz R, Wu M, et al. Designing compartmentalized hydrogel microparticles for cell encapsulation and scalable. J Mater Chem B Mater Biol Med. Royal Society of Chemistry; 2015;3: 353–360. doi:10.1039/C4TB01735H

93.   Saldin LT, Cramer MC, Velankar SS, White LJ, Badylak SF. Extracellular matrix hydrogels from decellularized tissues: Structure and function. Acta Biomater. Acta Materialia Inc.; 2017;49: 1–15. doi:10.1016/j.actbio.2016.11.068

94.   Li CY, Stevens KR, Schwartz RE, Alejandro BS, Huang JH, Bhatia SN. Micropatterned cell-cell interactions enable functional encapsulation of primary

hepatocytes in hydrogel microtissues. Tissue Eng Part A. 2014;20: 2200–2212. doi:10.1089/ten.TEA.2013.0667

95. Klouda L, Mikos AG. Thermoresponsive hydrogels in biomedical applications. Eur J Pharm Biopharm. 2008;68: 34–45. doi:10.1016/j.ejpb.2007.02.025

96. Hunt NC, Grover LM. Cell encapsulation using biopolymer gels for regenerative medicine. Biotechnol Lett. 2010;32: 733–42. doi:10.1007/s10529-010-0221-0

97. Xing Q, Yates K, Vogt C, Qian Z, Frost MC, Zhao F. Increasing mechanical strength of gelatin hydrogels by divalent metal ion removal. Sci Rep. 2014;4: 1–10. doi:10.1038/srep04706

98. Yue K, Trujillo-de Santiago G, Alvarez MM, Tamayol A, Annabi N, Khademhosseini A. Synthesis, properties, and biomedical applications of gelatin methacryloyl (GelMA) hydrogels. Biomaterials. 2015;73: 254–271. doi:10.1016/j.biomaterials.2015.08.045

99. Arya AD, Hallur PM, Karkisaval AG, Gudipati A, Rajendiran S, Dhavale V, et al. Gelatin Methacrylate Hydrogels as Biomimetic Three-Dimensional Matrixes for Modeling Breast Cancer Invasion and Chemoresponse in Vitro. ACS Appl Mater Interfaces. 2016;8: 22005–22017. doi:10.1021/acsami.6b06309

100. Gurski LA, Jha AK, Zhang C, Jia X, Farach-Carson MC. Hyaluronic acid-based hydrogels as 3D matrices for in vitro evaluation of chemotherapeutic drugs using poorly adherent prostate cancer cells. Biomaterials. 2009;30: 6076–6085. doi:10.1016/j.biomaterials.2009.07.054

101. Deegan DB, Zimmerman C, Skardal A, Atala A, Shupe TD. Stiffness of hyaluronic acid gels containing liver extracellular matrix supports human hepatocyte function and alters cell morphology. J Mech Behav Biomed Mater. Elsevier; 2015;55: 87–103. doi:10.1016/j.jmbbm.2015.10.016

102. Tibbitt MW, Anseth KS. Hydrogels as extracellular matrix mimics for 3D cell culture. Biotechnol Bioeng. 2009;103: 655–63. doi:10.1002/bit.22361

103. Allen P, Melero-Martin J, Bischoff J. Type I collagen, fibrin and Puramatrix matrices provide permissive environments for human endothelial and mesenchymal progenitor cells to form neovascular networks. J Tissue Eng Regen Med. 2011;5: e74–e86. doi:10.1097/MPG.0b013e3181a15ae8.Screening

104. Li Y, Meng H, Liu Y, Lee BP. Fibrin Gel as an Injectable Biodegradable Scaffold and Cell Carrier for Tissue Engineering. Sci World J. 2015; 1–10.

105. de la Puente P, Ludeña D. Cell culture in autologous fibrin scaffolds for applications in tissue engineering. Exp Cell Res. Elsevier; 2014;322: 1–11. doi:10.1016/j.yexcr.2013.12.017

106. Nuttelman CR, Tripodi MC, Anseth KS. Synthetic hydrogel niches that promote hMSC viability. Matrix Biol. 2005;24: 208–218. doi:10.1016/j.matbio.2005.03.004

107. Wang W, Guo L, Yu Y, Chen Z, Zhou R, Yuan Z. Peptide REDV-modified polysaccharide hydrogel with endothelial cell selectivity for the promotion of angiogenesis. Soc Biomater. 2014; 1703–1712. doi:10.1002/jbm.a.35306

108. Ali S, Saik JE, Gould DJ, Dickinson ME, West JL. Immobilization of Cell-Adhesive Laminin Peptides. Biores Open Access. 2013;2: 241–249. doi:10.1089/biores.2013.0021

109. Wang L, Lee F, Lim J, Du C, Wan ACA, Lee SS, et al. Enzymatic conjugation of a bioactive peptide into an injectable hyaluronic acid – tyramine hydrogel system to promote the formation of functional vasculature. Acta Biomater. Acta Materialia Inc.; 2014;10: 2539–2550. doi:10.1016/j.actbio.2014.02.022

110. Caliari SR, Burdick JA. A practical guide to hydrogels for cell culture. Nat Publ Gr. Nature Publishing Group; 2016;13: 405–414. doi:10.1038/nmeth.3839

111. McGrath AM, Novikova LN, Novikov LN, Wiberg M. BD PuraMatrix peptide hydrogel seeded with Schwann cells for peripheral nerve regeneration. Brain Res Bull. Elsevier Inc.; 2010;83: 207–213. doi:10.1016/j.brainresbull.2010.07.001

112. Bonino C a., Krebs MD, Saquing CD, Jeong SI, Shearer KL, Alsberg E, et al. Electrospinning alginate-based nanofibers: From blends to crosslinked low molecular weight alginate-only systems. Carbohydr Polym. 2011;85: 111–119. doi:10.1016/j.carbpol.2011.02.002

113. Jeong SI, Burns NA, Bonino CA, Kwon IK, Khan SA, Alsberg E. Improved cell infiltration of highly porous 3D nanofibrous scaffolds formed by combined fiber-fiber charge repulsions and ultra-sonication. J Mater Chem B. 2014;2: 8116–8122.

114. Bonino C a., Efimenko K, Jeong SI, Krebs MD, Alsberg E, Khan S a. Three-dimensional electrospun alginate nanofiber mats via tailored charge repulsions.

Small. 2012;8: 1928–1936. doi:10.1002/smll.201101791

115. Bhattacharya M, Malinen MM, Lauren P, Lou YR, Kuisma SW, Kanninen L, et al. Nanofibrillar cellulose hydrogel promotes three-dimensional liver cell culture. J Control Release. Elsevier B.V.; 2012;164: 291–298. doi:10.1016/j.jconrel.2012.06.039

116. Roth AD, Elmer J, Harris DR, Huntley J, Palmer AF, Nelson T, et al. Hemoglobin Regulates the Migration of Glioma Cells Along Poly (e -caprolactone) -Aligned Nanofibers. Biotechnol Prog. 2014;30: 1214–1220. doi:10.1002/btpr.1950

117. Breslin S, O'Driscoll L. Three-dimensional cell culture: The missing link in drug discovery. Drug Discov Today. Elsevier Ltd; 2013;18: 240–249. doi:10.1016/j.drudis.2012.10.003

118. Murphy S V, Atala A. 3D bioprinting of tissues and organs. Nat Biotechnol. 2014;32: 773–785. doi:10.1038/nbt.2958

119. Haycock J. 3D Cell Culture: A Review of Current Approaches and Techniques. 3D Cell Cult Methods Protoc Methods Mol Biol. 2011;695: 243–259. doi:10.1007/978-1-60761-984-0

120. Kim Y, Rajagopalan P. 3D hepatic cultures simultaneously maintain primary hepatocyte and liver sinusoidal endothelial cell phenotypes. PLoS One. 2010;5: 1–10. doi:10.1371/journal.pone.0015456

121. Hoffman AS. Hydrogels for biomedical applications. Adv Drug Deliv Rev. Elsevier B.V.; 2012;64: 18–23. doi:10.1016/j.addr.2012.09.010

122. Darnell M, Sun J-Y, Mehta M, Johnson C, Arany P, Suo Z, et al. Performance and Biocompatibility of Extremely Tough Alginate/Polyacrylamide Hydrogels. Biomaterials. 2013;34: 8042–8048. doi:10.1126/scisignal.2001449.Engineering

123. Khademhosseini A, Langer R. Microengineered hydrogels for tissue engineering. Biomaterials. 2007;28: 5087–92. doi:10.1016/j.biomaterials.2007.07.021

124. Andersen T, Melvik JE, Gåserød O, Alsberg E, Christensen BE. Ionically gelled alginate foams: Physical properties controlled by type, amount and source of gelling ions. Carbohydr Polym. 2014;99: 249–256. doi:10.1016/j.carbpol.2013.08.036

125. Samorezov JE, Morlock CM, Alsberg E. Dual Ionic and Photo-Crosslinked Alginate Hydrogels for Micropatterned Spatial Control of Material Properties and Cell Behavior. Bioconjug Chem. 2015;26: 1339–1347. doi:10.1021/acs.bioconjchem.5b00117

126. Jeon O, Alsberg E. Photofunctionalization of alginate hydrogels to promote adhesion and proliferation of human mesenchymal stem cells. Tissue Eng Part A. 2013;19: 1424–32. doi:10.1089/ten.TEA.2012.0581

127. Um SH, Lee JB, Park N, Kwon SY, Umbach CC, Luo D. Enzyme-catalysed assembly of DNA hydrogel. Nat Mater. 2006;5: 797–801. doi:10.1038/nmat1741

128. Meli L, Barbosa HSC, Hickey AM, Gasimli L, Nierode G, Diogo MM, et al. Three dimensional cellular microarray platform for human neural stem cell differentiation and toxicology. Stem Cell Res. Elsevier B.V.; 2014;13: 36–47.

doi:10.1016/j.scr.2014.04.004

129. Deiss F, Mazzeo A, Hong E, Ingber DE, Derda R, Whitesides GM. Platform for High-Throughput Testing of the Effect of Soluble Compounds on 3D Cell Cultures. Anal Chem. 2013;85: 8085–8094.

130. Meli L, Jordan ET, Clark DS, Linhardt RJ, Dordick JS. Influence of a three-dimensional, microarray environment on human Cell culture in drug screening systems. Biomaterials. Elsevier Ltd; 2012;33: 9087–9096. doi:10.1016/j.biomaterials.2012.08.065

131. Quackenbush J. Microarray Data Normalization and Transformation. Nat Genet. 2002;32: 496–501. doi:10.1038/ng1032

132. Ziauddin J, Sabatini DM. Microarrays of cells expressing defined cDNAs. Nature. 2001;411: 107–110. doi:10.1038/35075114

133. Rushmore TH, Kong A-NT. Pharmacogenomics, regulation and signaling pathways of phase I and II drug metabolizing enzymes. Curr Drug Metab. 2002;3: 481–90. Available: http://www.ncbi.nlm.nih.gov/pubmed/12369894

134. Zhu H, Qian J. Applications of Functional Protein Microarrays in Basic and Clinical Research. Changes. 2012;29: 997–1003. doi:10.1016/j.biotechadv.2011.08.021.Secreted

135. Templin MF, Stoll D, Schrenk M, Traub PC, Vöhringer CF, Joos TO. Protein microarray technology. Drug Discov Today. 2002;7: 815–822. doi:10.1016/S1359-6446(00)01910-2

136. Kwon SJ, Lee DW, Shah DA, Ku B, Jeon SY, Solanki K, et al. High-throughput and combinatorial gene expression on a chip for metabolism-induced toxicology screening. Nat Commun. Nature Publishing Group; 2014;5: 3739. doi:10.1038/ncomms4739

137. Baoqiang L, Wang L, Guo J, Xu F, Wei D, Feng Y, et al. Cell laden and patterned chitosan microgel for micro-scale tissue engineering. J Control Release. Elsevier B.V.; 2015;213: e9. doi:10.1016/j.jconrel.2015.05.011

138. Li B, Wang L, Xu F, Gang X, Demirci U, Wei D, et al. Hydrosoluble, UV-crosslinkable and injectable chitosan for patterned cell-laden microgel and rapid transdermal curing hydrogel in vivo. Acta Biomater. Acta Materialia Inc.; 2015;22: 59–69. doi:10.1016/j.actbio.2015.04.026

139. Hancock MJ, Yanagawa F, Jang YH, He J, Kachouie NN, Kaji H, et al. Designer hydrophilic regions regulate droplet shape for controlled surface patterning and 3D microgel synthesis. Small. 2012;8: 393–403. doi:10.1002/smll.201101745

140. Qi H, Du Y, Wang L, Kaji H, Bae H, Khademhosseini A. Patterned Differentiation of Individual Embryoid Bodies in Spatially Organized 3D Hybrid Microgels. Adv Mater. 2010;22: 5276–5281. doi:10.1002/nbm.3066.Non-invasive

141. Lee M-Y. Microarray Bioprinting Technology: Fundamentals and Practices. Lee M-Y, editor. Springer; 2016.

142. Lee DW, Choi YS, Seo YJ, Lee MY, Jeon SY, Ku B, et al. High-throughput screening (HTS) of anticancer drug efficacy on a micropillar/microwell chip

platform. Anal Chem. 2014;86: 535–542. doi:10.1021/ac402546b

143.   Lee DW, Lee MY, Ku B, Yi SH, Ryu JH, Jeon R, et al. Application of the DataChip/MetaChip technology for the evaluation of ajoene toxicity in vitro. Arch Toxicol. 2014;88: 283–290. doi:10.1007/s00204-013-1102-9

144.   Curley JL, Moore MJ. Facile micropatterning of dual hydrogel systems for 3D models of neurite outgrowth. J Biomed Mater Res - Part A. 2011;99 A: 532–543. doi:10.1002/jbm.a.33195

145.   Liang Y, Jeong J, DeVolder RJ, Cha C, Wang F, Tong YW, et al. A cell-instructive hydrogel to regulate malignancy of 3D tumor spheroids with matrix rigidity. Biomaterials. Elsevier Ltd; 2011;32: 9308–9315. doi:10.1016/j.biomaterials.2011.08.045

146.   Malinen MM, Paolkangas H, Yliperttula M, Urtti A. Peptide Nanofiber Hydrogel Induces Formation of Bile Canaliculi Structures in Three-Dimensional Hepatic Cell Culture. Tissue Eng Part A. 2012;18: 2418–2425.

147.   Schoofs G, Monica TJ, Ayala J, Horwitz J, Montgomery T, Roth G, et al. A high-yielding serum-free, suspension cell culture process to manufacture recombinant adenoviral vectors for gene therapy. Cytotechnology. 1998;28: 81–89. doi:10.1023/A:1008021428969

148.   Tsai W-H. Moment-preserving thresolding: A new approach. Comput Vision, Graph Image Process. 1985;29: 377–393. doi:10.1016/0734-189X(85)90133-1

149.   Narmoneva DA, Oni O, Sieminski AL, Zhang S, Gertler JP, Kamm RD, et al. Self-

131

assembling short oligopeptides and the promotion of angiogenesis. Biomaterials. 2005;26: 4837–4846. doi:10.1016/j.biomaterials.2005.01.005

150. Loo Y, Zhang S, Hauser CAE. From short peptides to nanofibers to macromolecular assemblies in biomedicine. Biotechnol Adv. Elsevier Inc.; 2012;30: 593–603. doi:10.1016/j.biotechadv.2011.10.004

151. Vallés-Llucha A, Arnal-Pastora M, Martínez-Ramosa C, Vilariño-Feltrera G, Vikingssona L, Castells-Salab C, et al. Combining self-assembling peptide gels with three-dimensional elastomer scaffolds. Acta Biomater. 2013;9: 9451–9460.

152. Jonker AM, Löwik DWP. M, Van Hest JCM. Peptide- and protein-based hydrogels. Chem Mater. 2012;24: 759–773. doi:10.1021/cm202640w

153. Censi R, Di Martino P, Vermonden T, Hennink WE. Hydrogels for protein delivery in tissue engineering. J Control Release. Elsevier B.V.; 2012;161: 680–692. doi:10.1016/j.jconrel.2012.03.002

154. Rodrigues RM, Bouhifd M, Bories G, Sacco MG, Gribaldo L, Fabbri M, et al. Assessment of an automated in vitro basal cytotoxicity test system based on metabolically-competent cells. Toxicol Vitr. Elsevier Ltd; 2013;27: 760–767. doi:10.1016/j.tiv.2012.12.004

155. Tolosa L, Gómez-Lechón MJ, Pérez-Cataldo G, Castell J V., Donato MT. HepG2 cells simultaneously expressing five P450 enzymes for the screening of hepatotoxicity: identification of bioactivable drugs and the potential mechanism of toxicity involved. Arch Toxicol. 2013;87: 1115–1127. doi:10.1007/s00204-013-

1012-x

156. Jemnitz K, Veres Z, Monostory K, Kóbori L, Vereczkey L. Interspecies differences in acetaminophen sensitivity of human, rat, and mouse primary hepatocytes. Toxicol Vitr. 2008;22: 961–967. doi:10.1016/j.tiv.2008.02.001

157. Tolosa L, Pinto S, Donato MT, Lahoz A, Castell J V., O'connor JE, et al. Development of a multiparametric cell-based protocol to screen and classify the hepatotoxicity potential of drugs. Toxicol Sci. 2012;127: 187–198. doi:10.1093/toxsci/kfs083

158. O'Brien PJ, Irwin W, Diaz D, Howard-Cofield E, Krejsa CM, Slaughter MR, et al. High concordance of drug-induced human hepatotoxicity with in vitro cytotoxicity measured in a novel cell-based model using high content screening. Arch Toxicol. 2006;80: 580–604. doi:10.1007/s00204-006-0091-3

159. Masters B. In Vitro Myotoxicity of the 3-Hydroxy-3-methylglutaryl Coenzyme A Reductase Inhibitors, Pravastatin, Lovastatin, and Simvastatin, Using Neonatal Rat Skeletal Myocytes [Internet]. Toxicology and Applied Pharmacology. 1995. pp. 163–174. doi:10.1006/taap.1995.1058

160. Zhu Y, D'Agostino J, Zhang QY. Role of intestinal cytochrome P450 (P450) in modulating the bioavailability of oral lovastatin: Insights from studies on the intestinal epithelium-specific P450 reductase knockout mouse. Drug Metab Dispos. 2011;39: 939–943. doi:10.1124/dmd.110.037861

161. Martinez TN, Greenamyre JT. Toxin models of mitochondrial dysfunction in

Parkinson's disease. Antioxid Redox Signal. 2012;16: 920–34. doi:10.1089/ars.2011.4033

162. Moeller TA, Shukla SJ, Xia M. Assessment of compound hepatotoxicity using human plateable cryopreserved hepatocytes in a 1536-well-plate format. Assay Drug Dev Technol. 2012;10: 78–87. doi:10.1089/adt.2010.0365

163. Westerink WMA, Stevenson JCR, Schoonen WGEJ. Pharmacologic profiling of human and rat cytochrome P450 1A1 and 1A2 induction and competition. Arch Toxicol. 2008;82: 909–921. doi:10.1007/s00204-008-0317-7

164. Garside H, Marcoe KF, Chesnut-Speelman J, Foster AJ, Muthas D, Kenna JG, et al. Evaluation of the use of imaging parameters for the detection of compound-induced hepatotoxicity in 384-well cultures of HepG2 cells and cryopreserved primary human hepatocytes. Toxicol Vitr. 2014;28: 171–181.

165. Persson M, Løye AF, Mow T, Hornberg JJ. A high content screening assay to predict human drug-induced liver injury during drug discovery. J Pharmacol Toxicol Methods. Elsevier Inc.; 2013;68: 302–13. doi:10.1016/j.vascn.2013.08.001

166. Pradip A, Steel D, Jacobsson S, Holmgren G, Ingelman-Sundberg M, Sartipy P, et al. High content analysis of human pluripotent stem cell derived hepatocytes reveals drug induced steatosis and phospholipidosis. Stem Cells Int. 2016;2016. doi:10.1155/2016/2475631

167. Lahoz A, Vilà MR, Fabre M, Miquel JM, Rivas M, Maines J, et al. An in vitro tool

to assess cytochrome P450 drug biotransformation-dependent cytotoxicity in engineered HepG2 cells generated by using adenoviral vectors. Toxicol Vitr. 2013;27: 1410–1415. doi:10.1016/j.tiv.2012.08.001

168. Lin J, Schyschka L, Mühl-Benninghaus R, Neumann J, Hao L, Nussler N, et al. Comparative analysis of phase I and II enzyme activities in 5 hepatic cell lines identifies Huh-7 and HCC-T cells with the highest potential to study drug metabolism. Arch Toxicol. 2012;86: 87–95. doi:10.1007/s00204-011-0733-y

169. Saladores P, Mürdter T, Eccles D, Chowbay B, Zgheib NK, Winter S, et al. Tamoxifen metabolism predicts drug concentrations and outcome in premenopausal patients with early breast cancer. Pharmacogenomics J. 2015;15: 84–94. doi:10.1038/tpj.2014.34

170. Jan Y-H, Richardson JR, Baker AB, Mishin V, Heck DE, Laskin DL, et al. Vitamin K3 (menadione) redox cycling inhibits cytochrome P450- mediated metabolism and inhibits parathion intoxication. Toxicol Appl Pharmacol. 2015;288: 114–120. doi:10.1161/CIRCRESAHA.116.303790.The

171. Mcgill MR, Sharpe MR, Williams CD, Taha M, Curry SC, Jaeschke H. The mechanism underlying acetaminophen- induced hepatotoxicity in humans and mice involves mitochondrial damage and nuclear DNA fragmentation. J Clin Invest. 2012;122: 1574–83. doi:10.1172/JCI59755.of

172. McGill MR, Jaeschke H. Metabolism and disposition of acetaminophen: Recent advances in relation to hepatotoxicity and diagnosis. Pharm Res. 2013;30: 2174–2187. doi:10.1007/s11095-013-1007-6

173. Haycock JW. 3D cell culture: a review of current approaches and techniques. Methods in molecular biology (Clifton, N.J.). 2011. doi:10.1007/978-1-60761-984-0_1

174. Burdick J a, Prestwich GD. Hyaluronic acid hydrogels for biomedical applications. Adv Mater. 2011;23: H41-56. doi:10.1002/adma.201003963

175. Deharde D, Schneider C, Hiller T, Fischer N, Kegel V, Lübberstedt M, et al. Bile canaliculi formation and biliary transport in 3D sandwich-cultured hepatocytes in dependence of the extracellular matrix composition. Arch Toxicol. Springer Berlin Heidelberg; 2016;90: 2497–2511. doi:10.1007/s00204-016-1758-z

176. Jang M, Neuzil P, Volk T, Manz A, Kleber A. On-chip three-dimensional cell culture in phaseguides improves hepatocyte functions in vitro. Biomicrofluidics. 2015;9: 1–12. doi:10.1063/1.4922863

177. Wang RM, Christman KL. Decellularized myocardial matrix hydrogels: In basic research and preclinical studies. Adv Drug Deliv Rev. 2016;96: 77–82.

178. Andersen T, Melvik JE, Gåserød O, Alsberg E, Christensen BE. Ionically gelled alginate foams: Physical properties controlled by operational and macromolecular parameters. Biomacromolecules. 2012;13: 3703–3710.

179. Nguyen KT, West JL. Photopolymerizable hydrogels for tissue engineering applications. Biomaterials. 2002;23: 4307–14. Available: http://www.ncbi.nlm.nih.gov/pubmed/12219820

180. Naficy S, Spinks GM, Wallace GG. Thin, tough, pH-sensitive hydrogel films with

rapid load recovery. ACS Appl Mater Interfaces. 2014;6: 4109–4114. doi:10.1021/am405708v

181. Jeon O, Powell C, Ahmed SM, Alsberg E. Biodegradable, photocrosslinked alginate hydrogels with independently tailorable physical properties and cell adhesivity. Tissue Eng Part A. 2010;16: 2915–2925. doi:10.1089/ten.tea.2010.0096

182. Jeon O, Bouhadir KH, Mansour JM, Alsberg E. Photocrosslinked alginate hydrogels with tunable biodegradation rates and mechanical properties. Biomaterials. Elsevier Ltd; 2009;30: 2724–2734. doi:10.1016/j.biomaterials.2009.01.034

183. Occhetta P, Visone R, Russo L, Cipolla L, Moretti M, Rasponi M. VA-086 Methacrylate Gelatine Photopolymerizable Hydrogels: a Parametric Study for Highly Biocompatible 3D Cell Embedding. J Biomater Res Part A. 2015;103: 2109–2117. doi:10.1002/jbm.a.35346/abstract

184. Chung, Cindy, Mesa, John, Randolph, Mark A., Yaremchuk, Michael, Burdick JA. Influence of gel properties on neocartilage formation by auricular chondrocytes photoencapsulated in hyaluronic acid networks. J Biomed Mater Res A. 2006;77: 518–525. doi:10.1002/jbm.a

185. Wang S, Jeon O, Shankles PG, Liu Y, Alsberg E, Retterer ST, et al. In-situ photopolymerization of monodisperse and discoid oxidized methacrylated alginate microgels in a microfluidic channel. Biomicrofluidics. 2016;10: 1–5. doi:10.1063/1.4941339

186. Ki CS, Shih H, Lin CC. Facile preparation of photodegradable hydrogels by photopolymerization. Polymer (Guildf). Elsevier Ltd; 2013;54: 2115–2122. doi:10.1016/j.polymer.2013.02.018

187. Qin XH, Ovsianikov A, Stampfl J, Liska R. Additive manufacturing of photosensitive Hydrogels for tissue engineering applications. BioNanoMaterials. 2014;15: 49–70. doi:10.1515/bnm-2014-0008

188. Xu L, Sheybani N, Yeudall WA, Yang H. The effect of photoinitiators on intracellular AKT signaling pathway in tissue engineering application. Biomater Sci. 2015;3: 250–255. doi:10.1109/TMI.2012.2196707.Separate

189. Jeon O, Alt DS, Ahmed SM, Alsberg E. The effect of oxidation on the degradation of photocrosslinkable alginate hydrogels. Biomaterials. Elsevier Ltd; 2012;33: 3503–3514. doi:10.1016/j.biomaterials.2012.01.041

190. Lee M-Y. Microarray Bioprinting Technology: Fundamental and Practices. Springer; 2016.

191. Ma Y, Ji Y, Huang G, Ling K, Zhang X, Xu F. Bioprinting 3D cell-laden hydrogel microarray for screening human periodontal ligament stem cell response to extracellular matrix. Biofabrication. IOP Publishing; 2015;7: 044105. doi:10.1088/1758-5090/7/4/044105

192. March S, Ng S, Velmurugan S, Galstian A, Shan J, Logan DJ, et al. A microscale human liver platform that supports the hepatic stages of plasmodium falciparum and vivax. Cell Host Microbe. Elsevier Inc.; 2013;14: 104–115.

doi:10.1016/j.chom.2013.06.005

193. Bale SS, Vernetti L, Senutovitch N, Jindal R, Hegde M, Gough A, et al. In vitro platforms for evaluating liver toxicity. Exp Biol Med. 2014;239: 1180–1191. doi:10.1177/1535370214531872

194. Khetani SR, Bhatia SN. Microscale culture of human liver cells for drug development. Nat Biotechnol. 2008;26: 120–126. doi:10.1038/nbt1361

195. Fernandes TG, Diogo MM, Clark DS, Dordick JS, Cabral JMS. High-throughput cellular microarray platforms: applications in drug discovery, toxicology and stem cell research. Trends Biotechnol. 2009;27: 342–9. doi:10.1016/j.tibtech.2009.02.009

196. Chen Y, Gao Q, Wan H, Yi J, Wei Y, Liu P. Surface modification and biocompatible improvement of polystyrene film by Ar, O2and Ar + O2plasma. Appl Surf Sci. Elsevier B.V.; 2013;265: 452–457. doi:10.1016/j.apsusc.2012.11.027

197. Lee JH, Kwon JS, Kim YH, Choi EH, Kim KM, Kim KN. The effects of enhancing the surface energy of a polystyrene plate by air atmospheric pressure plasma jet on early attachment of fibroblast under moving incubation. Thin Solid Films. Elsevier B.V.; 2013;547: 99–105. doi:10.1016/j.tsf.2013.04.105

198. Jeon, Oju, Alsberg E. Photofunctionalization of alginate hydrogels to promote adhesion and proliferation of human mesenchymal stem cells. Tissue Eng Part A. 2013;19: 1424–1432.

199. Kang LH, Armstrong PA, Lee LJ, Duan B, Kang KH, Butcher JT. Optimizing Photo-Encapsulation Viability of Heart Valve Cell Types in 3D Printable Composite Hydrogels. Ann Biomed Eng. 2017;45: 360–377. doi:10.1007/s10439-016-1619-1

200. Chen MB, Srigunapalan S, Wheeler AR, Simmons CA. A 3D microfluidic platform incorporating methacrylated gelatin hydrogels to study physiological cardiovascular cell–cell interactions. Lab Chip. 2013;13: 2591. doi:10.1039/c3lc00051f

201. Holle AW, Young JL, Spatz JP. In vitro cancer cell-ECM interactions inform in vivo cancer treatment. Adv Drug Deliv Rev. The Authors; 2016;97: 270–279. doi:10.1016/j.addr.2015.10.007

202. Wallace MC, Friedman SL. Hepatic Fibrosis and the Microenvironment: Fertile Soil for Hepatocellular Carcinoma Development. Gene Expr. 2014;16: 77–84. doi:10.3727/105221614X13919976902057

203. Reuter S, Gupta SC, Chaturvedi MM, Aggarwal BB. Oxidative stress, inflammation, and cancer: how are they linked? Free Radic Biol Med. Elsevier Inc.; 2010;49: 1603–16. doi:10.1016/j.freeradbiomed.2010.09.006

204. Quail DF, Joyce JA. Microenvironmental regulation of tumor progression and metastasis. Nat Med. 2013;19: 1423–1437. doi:10.1038/nm.3394

205. Thoma CR, Zimmermann M, Agarkova I, Kelm JM, Krek W. 3D cell culture systems modeling tumor growth determinants in cancer target discovery. Adv

Drug Deliv Rev. Elsevier B.V.; 2014;69–70: 29–41.
doi:10.1016/j.addr.2014.03.001

206. Haekanson M, Cukierman E, Charnley M, Hakanson M, Cukierman E, Charnley
     M. Miniaturized pre-clinical cancer models as research and diagnostic tools.
     Advanced Drug Delivery Reviews. 2014. pp. 52–66.
     doi:10.1016/j.addr.2013.11.010

207. Chengye W, Yu T, Ping S, Deguang S, Keyun W, Yan W, et al. Metformin
     reverses bFGF-induced transition in HCC cells. Oncotarget. 2017;8: 104247–
     104257.

208. Hu P-H, Pan L-H, Wong PT-Y, Chen W-H, Yang Y-Q, Wang H, et al. 125 I-
     labeled anti-bFGF monoclonal antibody inhibits growth of hepatocellular
     carcinoma. World J Gastroenterol. 2016;22: 5033–5041.
     doi:10.3748/wjg.v22.i21.5033

209. Giannelli G, Villa E, Lahn M. Transforming growth factor-β as a therapeutic target
     in hepatocellular carcinoma. Cancer Res. 2014;74: 1890–1894. doi:10.1158/0008-
     5472.CAN-14-0243

210. Aijaz A, Faulknor R, Berthiaume F, Olabisi RM. Hydrogel Microencapsulated
     Insulin-Secreting Cells Increase Keratinocyte Migration, Epidermal Thickness,
     Collagen Fiber Density, and Wound Closure in a Diabetic Mouse Model of Wound
     Healing. Tissue Eng Part A. 2015;21: 2723–2732. doi:10.1089/ten.TEA.2015.0069

211. Amann A, Zwierzina M, Gamerith G, Bitsche M, Huber JM, Vogel GF, et al.

Development of an innovative 3D cell culture system to study tumour - Stroma interactions in non-small cell lung cancer cells. PLoS One. 2014;9. doi:10.1371/journal.pone.0092511

212. Driscoll MK, Danuser G. Quantifying Modes of 3D Cell Migration. Trends Cell Biol. Elsevier Ltd; 2015;25: 749–759. doi:10.1016/j.tcb.2015.09.010

213. Kwon SJ, Lee DW, Shah DA, Ku B, Jeon SY, Solanki K, et al. High-throughput and combinatorial gene expression on a chip for metabolism-induced toxicology screening. Nat Commun. Nature Publishing Group; 2014;5: 3739. doi:10.1038/ncomms4739

214. Yu K-N, Nadanaciva S, Rana P, Lee DW, Ku B, Roth AD, et al. Prediction of metabolism-induced hepatotoxicity on three-dimensional hepatic cell culture and enzyme microarrays. Arch Toxicol. 2017; doi:10.1007/s00204-017-2126-3

215. Jeong SI, Jeon O, Krebs MD, Hill MC, Alsberg E. Biodegradable photo-crosslinked alginate nanofibre scaffolds with tuneable physical properties, cell adhesivity and growth factor release. Eur Cells Mater. 2012;24: 331–343.

216. Zuo Q, Guo R, Liu Q, Hong A, Shi Y, Kong Q, et al. Heparin-conjugated alginate multilayered microspheres for controlled release of bFGF. Biomed Mater. IOP Publishing; 2015;10: 035008. doi:10.1088/1748-6041/10/3/035008

217. Lee K, Silva E a, Mooney DJ. Growth factor delivery-based tissue engineering: general approaches and a review of recent developments. J R Soc Interface. 2011;8: 153–170. doi:10.1098/rsif.2010.0223

218. Nakamura S, Ijima H. Solubilized matrix derived from decellularized liver as a growth factor-immobilizable scaffold for hepatocyte culture. J Biosci Bioeng. Elsevier Ltd; 2013;xx: 1–8. Available: http://www.mendeley.com/c/5731088441/p/15252503/nakamura-2013-solubilized-matrix-derived-from-decellularized-liver-as-a-growth-factor-immobilizable-scaffold-for-hepatocyte-culture/

219. Mccall JD, Luoma JE, Anseth KS. Covalently tethered transforming growth factor beta in PEG hydrogels promotes chondrogenic differentiation of encapsulated human mesenchymal stem cells. Drug Deliv Transl Res. 2012;2: 305–312. doi:10.1007/s13346-012-0090-2

220. Jeon O, Powell C, Solorio LD, Krebs MD, Alsberg E. Affinity-based growth factor delivery using biodegradable, photocrosslinked heparin-alginate hydrogels. J Control Release. Elsevier B.V.; 2011;154: 258–266. doi:10.1016/j.jconrel.2011.06.027

221. Sakiyama-Elbert SE. Incorporation of heparin into biomaterials. Acta Biomater. Acta Materialia Inc.; 2014;10: 1581–1587. doi:10.1016/j.actbio.2013.08.045

222. Ashikari-Hada S, Habuchi H, Kariya Y, Itoh N, Reddi AH, Kimata K. Characterization of Growth Factor-binding Structures in Heparin/Heparan Sulfate Using an Octasaccharide Library. J Biol Chem. 2004;279: 12346–12354. doi:10.1074/jbc.M313523200

223. Luo D, Wang Z, Wu J, Jiang C, Wu J. The role of hypoxia inducible factor-1 in hepatocellular carcinoma. Biomed Res Int. 2014;2014: 409272.

doi:10.1155/2014/409272 [doi]

224. Wong CCL, Kai AKL, Ng IOL. The impact of hypoxia in hepatocellular carcinoma metastasis. Front Med China. 2014;8: 33–41. doi:10.1007/s11684-013-0301-3

225. Chen YF, Tseng CY, Wang HW, Kuo HC, Yang VW, Lee OK. Rapid generation of mature hepatocyte-like cells from human induced pluripotent stem cells by an efficient three-step protocol. Hepatology. 2012;55: 1193–1203. doi:10.1002/hep.24790

226. Yu G, Jing Y, Kou X, Ye F, Gao L, Fan Q, et al. Hepatic Stellate Cells Secreted Hepatocyte Growth Factor Contributes to the Chemoresistance of Hepatocellular Carcinoma. PLoS One. 2013;8: e73312. doi:10.1371/journal.pone.0073312

227. Qiu GH, Xie X, Xu F, Shi X, Wang Y, Deng L. Distinctive pharmacological differences between liver cancer cell lines HepG2 and Hep3B. Cytotechnology. 2014;67: 1–12. doi:10.1007/s10616-014-9761-9

APPENDICES

A.1. OMA-15 Viability and Polymerization Results

Table 7 Lists all of the various experiments performed on using OMA-15 as a scaffold for growing Hep3B cells. All experiments were performed with the same optimized plasma surface treatment of high RF exposure for 15 minutes. In general, OMA-15 proved to be an unsuitable scaffold at the conditions we tested. While viable cells were achieved at several of the listed conditions, polymerization was not observed in an of the indicated conditions. Ultimately, unpolymerized hydrogels resulted in cell settling at the bottom of the microwell chip forming 2D confluent layers if toxicity was not observed.

Table 8. Photopolymerization tested on OMA-15

Concentration (w/v %)	Exposure Intensity (%)	Exposure Time (min)	PI (w/v %)	Viable Cells?	Gel formed?
4	45	4, 8	0.1, 0.2, 0.3	No	No
			0.3, 0.4, 0.5	No	No
		3, 6	0.025, 0.05, 0.1	Yes	No
2	45	3, 6	0.1, 0.2, 0.3	No	No
2 / 4	70	0.5, 1	0.025, 0.05, 0.1	No	No
2 / 4	70	0.75, 1.5 (immersion)	0.025, 0.05, 0.1	Yes	No
2 / 4	70	1, 2 (immersion)	0.025, 0.05, 0.1	Yes (1 min)	No

An additional experiment we performed was testing how immersion of our samples in water could affect polymerization. Our reasoning was that increased temperatures due to the intensity of exposed light can warm the sample sufficiently enough to either damage the cells or make them more susceptible to oxidative stress. Samples that were immersed in water had a breath-easy membrane added to the surface after printing but before exposure. Ultimately, the results had no effect on increasing polymerization efficiently though viable 2D cells were achieved during shorter durations.

A.2. Photopolymerizable Collagen Results

We attempted to work with a commercialized variation of methacrylated collagen. Since much of the liver ECM scaffold consists of collagen I, we thought using a photopolymerizable variant would yield an optimized biocompatibility while give us control over when gelation occurs. Moreover, photocrosslinking would increase robustness of a hydrogel that polymerizes due to increases in temperature. Cells would be printed at 4 * 10^6 cells/mL into microwell chips, with collagen concentration varying between 1 and 3 mg/mL, and PI concentration at 0.05 w/v % (using Irgacure 2959). Before adding cells, collagen must be suspended in 20 mM acetic acid and then neutralized with the requisite neutralization solution provided by Advanced BioMatrix (5201-1EA). Photopolymerization occurred at 4 mW/cm² for 30 seconds, followed by incubating microwell chips at 37°C for half an hour in a moisture-controlled chamber before being immersed into complete RPMI in petri plates.

The results of the experiment are shown in Figure 18. Polymerization of collagen was successful at 2 and 3 mg/mL, while using 1 mg/mL produced confluent cells. The use

of PI had a toxic effect at all indicated concentrations. The results indicate that at our tested values, while collagen is a suitable hydrogel, adding the photocrosslinking step does not improve the robustness of the hydrogel at any concentrations and impacts viability throughout. Like OMA-15, we discarded use of this hydrogel after several attempts to decrease the toxicity associated with photopolymerization while varying polymerization parameters. It is possible that this hydrogel is

A.3. pcDNA Transfections into Hep3B cells.

As an alternative method to create a permanently fluorescent cell line, we attempted to transfect plasmid DNA into Hep3B cells. We used a Lipofectamine 2000 Transfection Kit (Thermofisher scientific, catalog no. 11668027) with high concentrations of pcDNA (500-5000 ng/mL) containing the expression of RFP. After leaving the transfection reagents on for 48 hours, we attempted to select out cells using genticin with variable concentration (1-10%). Our results were ultimately unsuccessful. While transfection was successful, Hep3B cells proved not to be susceptible to genticin toxicity, meaning we could not select out cells that were not transfected. While this method could be potentially used for other cell lines, it is not compatible with Hep3B cells.

A.4. Assessing Fluorescent Reagents for CYP450 Activity

Several fluorescent and one luminescent assay was conducted to work with CYP450 enzymes (table 9). These substrates were tested for activity according to manufacturer's protoctols against pure enzymes, against cells infected with adenoviruses containing the expressions of these enzymes, and cDNA/pcDNA transfected cells. With the exceptions of 7-EC and MFC, all substrates fluoresced/luminesced when tested against their specific enzymes. However, only EOMCC/BOMCC worked against virus infected

cells. This indicates that these substrates are the only ones that can be use of the tested enzymes for cell-based activity. Furthermore, only CYP1A2 and CYP2C9 expression was successfully transduced into Hep3B cells.

Table 9. Substrates tested for CYP450 activity

Substrate	Metabolite	Isoform	Enzyme Activity	Virus Activity
7-Ethoxycoumarin (7-EC)	7-Hydroxycoumarin	1A2	-	-
Dibenzyl-fluorescein (DBF)	Fluorescein	2C9	+	-
3-[2-(N,N-diethyl-N-methyl-ammonium)ethyl]-7-methoxy-4-methylcoumarin (AMMC) Iodide	3-[2-(N,N-diethyl-N-methyl-ammonium)ethyl]-7-hydroxy-4-methylcoumarin (AHMC) Iodide	2D6	+	-
7-Methoxy-4-Trifluoromethylcoumarin (MFC)	7-hydroxy-4-Trifluoromethylcoumarin (HFC)	2E1	-	-
7-benzyloxy-4-Trifluoromethylcoumarin (BFC)	HFC	3A4	+	-
7-ethyloxymethyloxy-3-cyanocoumarian (EOMCC)	7-hydroxy-3-cyanocoumarin	1A2/2D6/2E1	++/+/+	+/-/-
7-benzyloxymethyloxy-3-cyanocoumarian (BOMCC)	7-hydroxy-3-cyanocoumarin	2C9/3A4	+/++	+/-
Luciferin-pentafluorobenzene (Luciferin-PFBE)	Luciferin	3A4	+	-

(-) No activity detected. (+) Moderate response. (++) significant response.